“Crystallization study on the lipid-based system: Cocoa Butter-Tristearin/Cocoa Butter-Coconut Oil and Fat/Oil-Hydrocarbons Blends: Thermal mixing behavior, crystallization kinetics, and rheology.”

Dissertation for obtaining the degree

"Doctor of the Natural Sciences"

In the subject of Chemistry

At the Department of Chemistry, Pharmacy, and Geosciences of the Johannes Gutenberg University in Mainz

Bhagyashri Laxmikant Joshi

Mainz, 09.03.2021

Dekan: Prof. Dr. Tobias Reich

1. Berichterstatter: Prof. Dr. Thomas Vilgis

2. Berichterstatter: Prof. Dr. Micheal Maskos

Tag der mündlichen Prüfung: 15.04.2021

Abstract

The mixing behavior of lipid blends results in a change in thermal, mechanical properties of the end product and these macroscopic properties are dependent on the nanoscale interactions of various lipid systems. Fundamental understanding of such interactions is essential and hence in this study, the main goal was to understand the mixing behavior in bulk lipid blends such as Cocoa Butter/Tristearin (CB/TS) and Cocoa Butter/Coconut Oil (CB/CO) blends. Based on the results of differential scanning calorimetry (DSC), the pseudo-binary phase diagram for CB/TS and CB/CO blends was achieved. This pseudo-solid liquid state diagram was further analyzed by using a mathematical model (Bragg-William's approximation) for understanding the thermodynamics behind ideal and non-ideal mixing behavior. Together with this analysis, the interaction between CB/TS and CB/CO at solid and liquid state resulted in monotectic and eutectic kind of phase diagrams. To understand in deep the interactions between CB and TS, coherent anti-Stokes Raman Scattering (CARS) microscopy and X-ray diffraction (XRD) techniques were used. These analyses were in agreement with DSC results and showed that phase separation occurs at a solid-state, also resulted that the S-L-S (solid-liquid-solid) transition occurs at a lesser temperature as the concentration of CB increases, and hence, the decrease in melting temperature of TS was observed after addition of CB. Next, to understand the thermal behavior for CB/CO blends deeply, a crystallization kinetic study was carried out by using ^{1}H solid-state nuclear magnetic resonance (SSNMR) and oscillatory rheology. The Solid Fat Content (SFC) from the NMR study and storage modulus from rheology contributed to a similar trend to the DSC study indicating eutectic mixture at 65wt% CO and 35wt% CB ($E_{CB\text{-}CO}$). Further, the fractal nature in the fat crystal network of CB/CO blends was analyzed by using the "Kraus model" fitting to amplitude sweep and by fractal box-counting method on image analysis. After understanding these mixing mechanisms, derivatives of paraffin waxes (3 specific n-alkanes) were mixed with $E_{CB\text{-}CO}$ to observe the effect on thermal, morphological, rheological properties, and crystallization kinetics with respect to the carbon chain length. The results depicted that, melting temperature, storage modulus, and SFC increased after the addition of 1wt% of C (20), C (25), whereas phase separation was observed for 1wt% C (30).

A further similar study with the addition of n-alkanes to pure CB and CO revealed that the interaction of n-alkanes with $E_{CB\text{-}CO}$ is dominated by the interaction of n-alkanes with CO

instead of CB. Thus, n-alkanes acted as the seed crystals with less concentration and act as an organo-gelator for more concentration (e.g. at and above 5wt %) for a higher number of carbon chain lengths (C (25) and C (30) with respect to the current study models). Therefore, present findings provide insight into how the purpose of n-alkanes to the crystallization process of CB and CO differs with respect to the concentration and carbon chain length, which definitely will help to design the processes for products containing such model systems. Altogether, with the current research, the effect on macroscopic properties of fat blends is dependent on microscopic and nanoscale interactions.

Acknowledgments

First of all, I would like to thank Prof. Dr. Thomas Vilgis for providing me an opportunity to carry out my Ph.D. studies. Thanks for your support, your trust, and encouragement. Also thank you for supervising my work with patience. You're a great mentor!

Thank you, Prof. Dr. Kremer, for allowing me to carry this work at Max Planck Institute of Polymer Research.

I also would like to thank Prof. Dr. Michael Maskos for being my preliminary supervisor during my research work. The progress report meetings indeed help me to improve my presentation skills along with research question understanding.

I would also like to thank all Technical Assistants at MPI-P for their help in carrying out experiments and for helping me out with all the experimental doubts that I had always and also your support and willingness to help me during my entire work.

Thank you, Dr. Robert Graf, Prof. Dr. Markus Mezger, Dr. Sapun Parekh, and Yujen Wang for allowing me to collaborate with your group. It indeed helps me to understand my research questions in a deep manner. I enjoyed all those discussions with you all.

I would like to express my deepest gratitude towards Dr. Birgitta Zielbauer, Dr. Steffen Beccard for being great colleagues and had faith in me and my work. Thank you very much Marta Ghebremedhin for critical reading of thesis and all the discussions that we had. Thank you Judith Hege being the great office mate. Also would like to thank all the foodies members, Dr. Trivikram Nallamilli, Juan Zambrano, Christine Schreiber, Sreejani Barua, Hannah Hartge, Sarah Gindra, Markus Kaetomeki, and Mathias Schmitt.

Last but not least, I would like to thank my husband Dr. Prasad Chikte for constant moral support without which it would be impossible to carry out my studies. Also all the family members back home in India I would like to thank you all!

Table of contents

List of illustrations

List of tables

List of abbreviations

CB **Cocoa Butter**

TS **Tristearin**

dTS **Deuterated Tristearin**

CO **Coconut Oil**

DSC **Differential Scanning Calorimetry**

PLM **Polarized Light Microscopy**

CARS **Coherent anti-Stokes Raman Spectroscopy**

XRD **X-ray Diffraction**

SAXS **Small Angle X-ray Scattering**

WAXS **Wide Angle X-ray Scattering**

SSNMR **Solid State Nuclear Magnetic Resonance**

TAG **Triacylglycerol or Triglycerides**

DAG **Diacylglycerol**

MAG **Monoacylglycerol**

FA **Fatty acid**

sn **stereospecific numbering**

S-L-S **Solid-Liquid-Solid**

S-S **Solid-Solid**

SFC **Solid Fat Content**

$E_{CB\text{-}CO}$ **Eutectic mixture of CB-CO**

LVE **Linear Viscoelastic**

N-LVE **Non-Linear Viscoelastic**

HMF **High Melting Fraction**

MMF **Medium Melting Fraction**

LMF **Low Melting Fraction**

List of variables

ΔG **Differential Gibbs free energy of a blend [J]**

ΔG_s **Differential Surface Gibbs free energy of a blend [J]**

ΔG_v **Differential Volume Gibbs free energy of a blend [J]**

ΔH **Differential Enthalpy of a blend [J/g]**

ΔS **Differential Entropy of a blend [J/K]**

T **Temperature [K]**

ΔT **Difference in temperature [K]**

δ **Crystal melt interfacial tension [N/m]**

S **Supersaturation ratio**

r **Radius of crystal nuclei [m]**

r_{3D}^* **Critical radius of a stable nuclei [m]**

ΔG_{3D}^* **Differential Gibbs free energy of stable crystal nuclei [J]**

V **Volume fraction of solid at specific time t**

V_0 **Volume fraction of solid at time t=0**

Vm **Maximum volume fraction obtained at a specific temperature**

k **Avrami constant**

n **Avrami exponent**

SFC **Solid fat content at particular time t**

SFCmax **Maximum solid fat content at a specific temperature**

d_f **Fractal dimension from Kraus model**

D_b **Box count fractal dimension**

D_f **Particle count fractal dimension**

G' Storage modulus at specific amplitude [Pa]

G'_0 Storage modulus at initial amplitude [Pa]

G'_∞ Storage modulus at infinite amplitude [Pa]

Φ_S Heat flow required for sample [W/g]

Φ_R Heat flow required for reference [W/g]

ω_{as} Antistokes frequency

ω_p pump beam frequency

ω_{pr} probe beam frequency

ω_s stokes beam frequency

λ Wavelength of x-ray beam [nm]

q scattering vector

ΔE Photon energy [J]

h Planck's constant = 6.626*10^-34 [J.s]

B_0 Applied magnetic field [T]

γ Oscillation strain (%)

σ Stress [Pa]

G" Loss modulus [Pa]

x_A Mole fraction of component A

x_B Mole fraction of component B

χ Energy difference between pair (A-B) and an average of (A-A) and (B-B)

u_{AA} Binary interaction energy between A-A pair

u_{BB} Binary interaction energy between B-B pair

u_{AB} Binary interaction energy between A-B pair

R Ideal gas constant [8.3145 $J.mol^{-1}.K.^{-1}$]

T_A Melting temperature of component A [K]

T_B Melting temperature of component B [K]

Chapter 1: Introduction

Lipids mainly consist of constituents that have long-chain aliphatic hydrocarbons. These materials are further subcategorized as: hydrocarbons; fatty acids (FA); acylglycerols: mono, di and tri; waxes; sterols and sterol esters; phospholipids, and so on [1]. A variety of lipids are present in nature in different amounts along with different physico-chemical properties. Therefore, understanding the properties of such basic lipid systems is necessary to elaborate the questions which are involved in more complex food systems; for instance the problems in the production of good quality confectionery, bakery, etc. products. In food applications, lipid plays an important role in providing nutritional values as well as sensory properties. Therefore, this study is focused on two types of lipids: a) fats and oils as a basis of mixtures of acylglycerols and b) derivatives of wax in terms of hydrocarbons. Understanding the chemical nature of these model systems and their interactions at solid and liquid states will help eventually in practical applications for designing the food products containing these model systems. Therefore, this chapter will highlight the details of the model systems used, the basic concepts of the crystallization process, the crystallization kinetics, and the rheological study on the mixing behavior of these above-mentioned lipids. Furthermore, in this chapter, the conceptual understanding of techniques, which are used to carry out this study is mentioned.

1.1 Fats and oils

Fats and oils are essential components in food, pharmaceutical, and cosmetic applications [2]–[4]. Likewise, in some applications, the lipid system is one of the main constituents, which defines the ultimate product quality and storage life [5], [6]; Therefore, it is necessary to understand the physico-chemical properties of these components. The terms fats and oils are used interchangeably, as they are usually based on their physical state of the material at ambient conditions. Fats exist in the solid-state at ambient temperatures, whereas oils appear liquid [7]. However, the chemical composition defines the physico-chemical and textural characteristics of the individual fat or oil, which eventually determines the suitability of such ingredients in different applications. Fats and oils are the esters of three fatty acid chains; they are called triacylglycerol or triglycerides (TAG). It is a chemical reaction between one glycerol molecule

and three FA chains. The chemical reaction is shown in Figure 1, in which R represents the long chain of carbon atoms (aliphatic hydrocarbons). These hydrocarbons contain at least 4 carbon atoms and depending on their carbon chain length the physical behavior of oils and fats changes [8]. Another parameter to be considered is the degree of saturation, which describes the presence of double bonds between two carbon atoms. Therefore, according to degree of saturation, FAs are distributed typically in two types, one is saturated (with presence of no double bond) and another is unsaturated (at least one (cis) double bond). The general representation of FA is in the form of C(n:s), where, n represents the number of carbon atoms present and s is the degree of saturation i.e. number of carbon-carbon (C-C) double bonds.

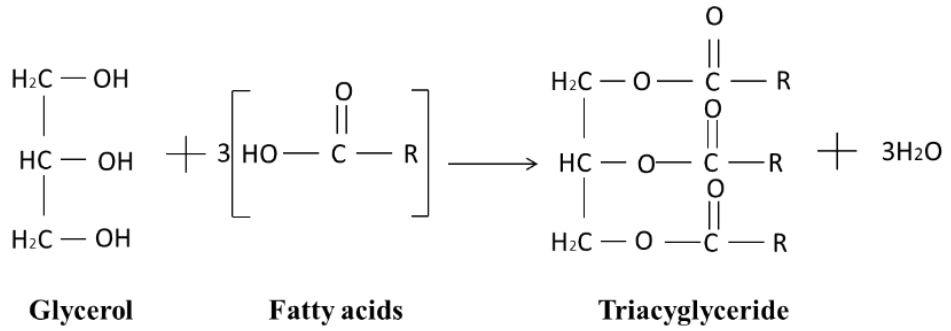

Figure 1: Chemical reaction between glycerol and three fatty acids, which produces triacylglycerol (TAG) along with the removal of three water molecules (R- represents the carbon chain).

Figure 2, shows how the conformation of FAs changes depending on the number of double bonds present in the carbon chain. Octadecane is the n-alkane (aliphatic hydrocarbon) showing the zig-zag structural arrangement of the hydrocarbon chain. Therefore, the structural arrangement of FA is dependent on the type of hydrocarbon chain attached. For instance, in Figure 2, they all contain the same number of carbon atom C (18), but their degree of saturation is increasing from stearic acid to linolenic acid respectively, and so the structure becomes more complex than that of the saturated acid (stearic acid). Hence, during the crystallization process, stearic acid has the advantage of packing itself densely due to its straight chain.

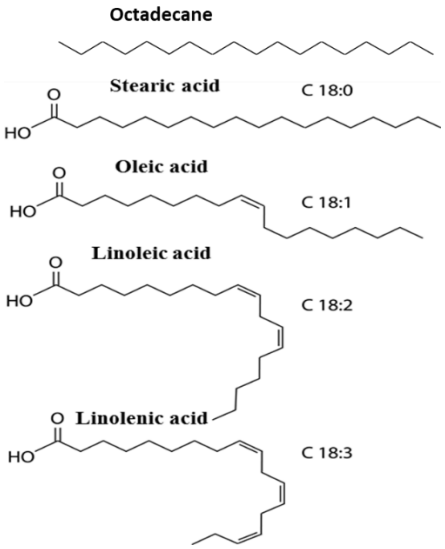

Figure 2: The 2D representation of n-alkane and change in FA structure conformation according to the degree of saturation in the carbon chain. Here the number of carbon atoms in each FA is same [8].

This property helps to form a crystalline structure with a smaller number of defects (almost perfectly arranged crystal structure) and so during melting of these crystals the energy required would be higher as compared to the crystals with more defects. Therefore, due to the presence of fewer defects in the crystal structure, it becomes more stable and eventually, melts at a very high temperature. As the degree of saturation increases, the 'kinks' in the chemical structure form, which creates difficulty in forming a closely packed structure during crystallization. Consequently, improper crystal structure formation occurs, which leads to less stability and hence it melts at a lower temperature. Thus, the melting temperature decreases from stearic acid to linolenic acid (74 °C to -16.5 °C) [8]. As the physico-chemical properties of fats and oils are dependent on the constituents present in them, specifically: various types of TAGs, the crystallization process in TAGs is essential to study. In the next section, the theory behind the crystallization process and how does the TAG tend to form crystals are explained.

1.2 Crystallization of Lipids

How is the crystallization process defined? It is a system arrangement as a result of driven force, that is characterized by total or partial restriction of movements inistigated by physical or chemical bonds between atoms or molecules [9]. These forces could be either, temperature,

pressure-dependent or due to supersaturation state or even involvement of the mixtures of these driving forces altogether in the system. These orderly arrays of the arranged particle are termed as crystals. These crystals are building blocks of a 3D structure having a 'unit cell' as a foundation base. The number of molecules in the unit cell and dimension of the unit cell are denoted by Z and lattice parameters (a, b, c, α, β and γ) (Figure 3). There are 14 types of unit cells, which can order together to form space lattice, which is also called as 'Bravais lattices' [10], [11]. These lattices are distributed into basic seven groups (Table 1) and depending on the presence of atoms or molecules, they are further sub-categorized and hence 14 types of lattices (Figure 4).

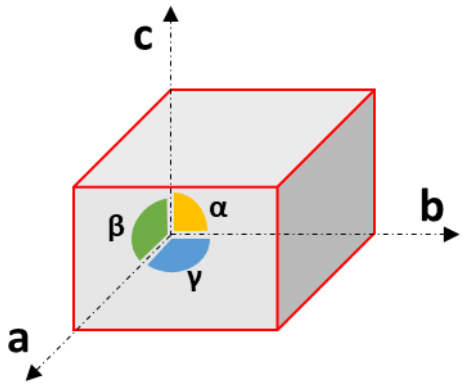

Figure 3: Schematic representing the three crystallographic axes a, b, c, and their corresponding angles α, β, and γ respectively for the unit cell.

Table 1: The seven crystal systems, their corresponding associated lattice types, and structural characteristics [11].

System	Axes	Angles	Lattice Type
Cubic	$a = b = c$	$\alpha = \beta = \gamma = 90°$	P, F, I
Tetragonal	$a = b \neq c$	$\alpha = \beta = \gamma = 90°$	P, I
Hexagonal	$a = b \neq c$	$\alpha = \beta = 90°, \gamma = 120°$	P
Orthorhombic	$a \neq b \neq c$	$\alpha = \beta = \gamma = 90°$	P, C, I, F
Rhombohedral	$a = b = c$	$\alpha = \beta = \gamma < 120° \neq 90°$	P
Monoclinic	$a \neq b \neq c$	$\alpha = \gamma = 90°, \beta \neq 90°$	P, C
Triclinic	$a \neq b \neq c$	$\alpha \neq \beta \neq \gamma$	P

P, simple (primitive); I, body-centered; F, face-centered; C, base centered

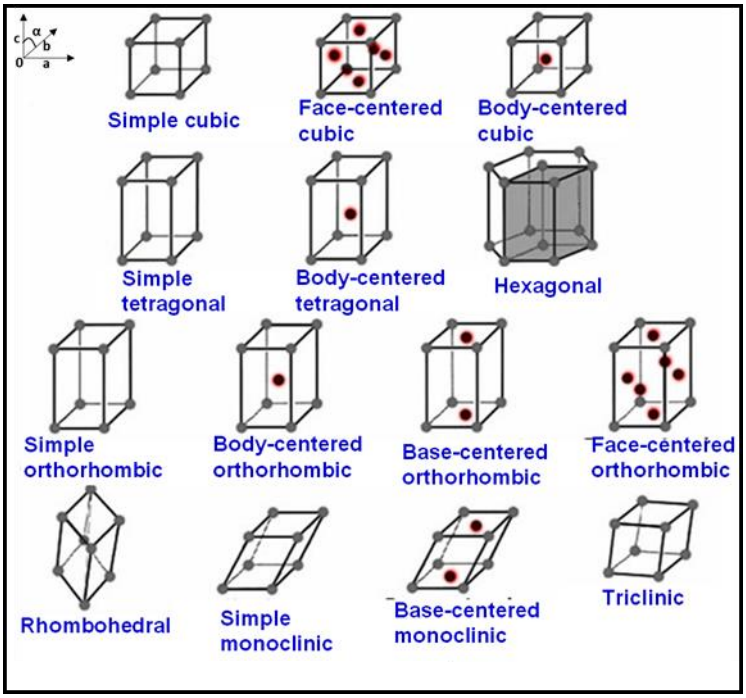

Figure 4: 14 types of Bravais lattices [11].

Those with the lattice points only at corners, are called as simple or primitives, body-centered (I) have lattice points only at the center of their faces, for base-centered (C) unit cells, lattice points are only at two of the four faces of unit cells and face-centered (F) unit cells have lattice points at the center of the faces. Therefore, there are in total of 14 types of lattice structures. Eventually, the symmetry of one of these unit cells corresponds to the specific type of crystal structure.

(a) Polymorphism:

There are evidences that long-chain compounds can exist in various crystalline forms. For instance, solids persisting same composition although potentially can exist in more than one crystalline form are known as polymorphs. Hence, polymorphism can be defined in terms of the ability to manifest different unit cell structures as a result of various molecular packings [9]. The polymorphic forms of fat are identified based on their subcell structure [12]. In lipid systems, there are three polymorphs present: α, β', β. The schematic of the subcell chain packing of these polymorphs is shown below in Figure 5. It is a top view schematic representation of hexagonal (H), orthorhombic perpendicular ($O_{\perp}$) and triclinic parallel ($T_{//}$) subcell structures of α, β' and β polymorphs respectively. Subcell structure defined as the cross-

sectional packing mode of zigzag hydrocarbon chains used to characterize the hydrogen packing. There are more than nine types of subcell structures that have been found in lipid systems [13], [14]. In the case of hexagonal packing, the hydrocarbon chains do not assume specific orientation, instead, they undergo torsional motion with aliphatic *gauche* conformation, and hence 'H' structure leads to less stability. The '$O_{\perp}$' subcell consists of zigzag planes that are perpendicular to its neighboring planes, whereas, in '$T_{//}$' (triclinic parallel plane), all hydrocarbon zigzag planes are in parallel. Therefore, '$O_{\perp}$' subcell structure is metastable, and '$T_{//}$' is a strongly packed configuration and thus is the most stable form of all. As each polymorph has a specific lattice structure and so depending on their packing ability (loosely packed or densely packed) the melting temperature varies.

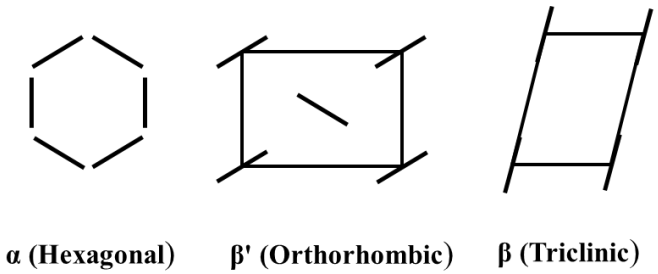

Figure 5: Schematic representation of the subcell chain packing structure which is commonly found in TAG polymorphic forms (top view of crystal planes) (Modified from [15]).

Upon crystallization the glycerol molecule, tend to form two possible kinds of conformation: (a) *chair*; (b) *tunning fork* (Figure 6(a)). In the case of *chair* conformation, hydrocarbon chains at sn-1 and sn-2 positions are packed in the same leaflet, and sn-3 position hydrocarbon is arranged in opposite direction. Whereas, in the *tunning fork* hydrocarbon chain at sn-1 and sn-3 are packed together in one direction and the hydrocarbon chain at the sn-2 position is placed in the opposite direction. However, there is no specific rule on the formation of two types of conformations [15]. Aggregation of these conformation leads to the formation of chain length structure. The possible stacking of TAG molecules is 2L or 3L, in which L indicates the length of FA. This stacking TAG lamella is also described as long spacings, whereas, short-spacing in each polymorphic form associated with the subcell of the structure arises from the unit cell formed from TAG packing. The representation of these terminologies is shown in Figure 6 (b).

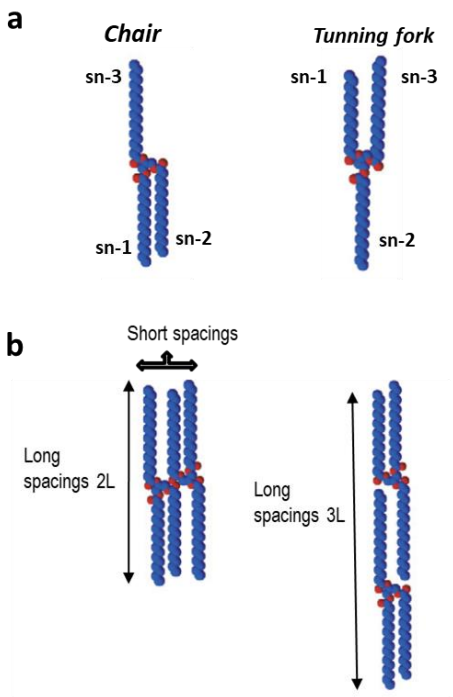

Figure 6: (a) Upon crystallization possible conformations of TAGs: *chair* or *tunning fork* (b) Possible arrangements of TAG molecules, either in 2L or 3L form, where, L represents the length of FA [16].

The packing ability of these polymorphs is also dependent on the angle between the methyl plane and the TAG molecule. For instance, in the case of SOS (Stearate-Oleate-Stearate), four different types of polymorphs exist depending on the crystallization conditions. They differ with respect to their chain length (double or triple) and the angle between the methyl plane and TAG (shown in Figure 7). In case of polymorphs having subcell structure of α, the arrangement of TAGs is of double chain length packing (hexagonal structure) with no angle of tilt, whereas in γ, the double chain length increased to 3L, therefore it is more closely packed, and this leads to a higher melting point than α. Another parameter is the angle of tilt, in the β' polymorph (orthorhombic structure) there is a slight decrease in angle and therefore the chain length is decreased to some extent. Due to tilt, they form closer packing than γ polymorph and hence the melting temperature increased by one degree. In case of β1 and β2 (triclinic structure), the angle decreased to approx. 50° to 70° and due to a decrease in angle, they pack tightly together, and hence the melting temperature is higher than other polymorphs [8], [17]. Two different sub-cell structures melt at two different temperatures due to differences in the angle of tilt. A lower angle of tilt results in a closely packed structure hence higher stability.

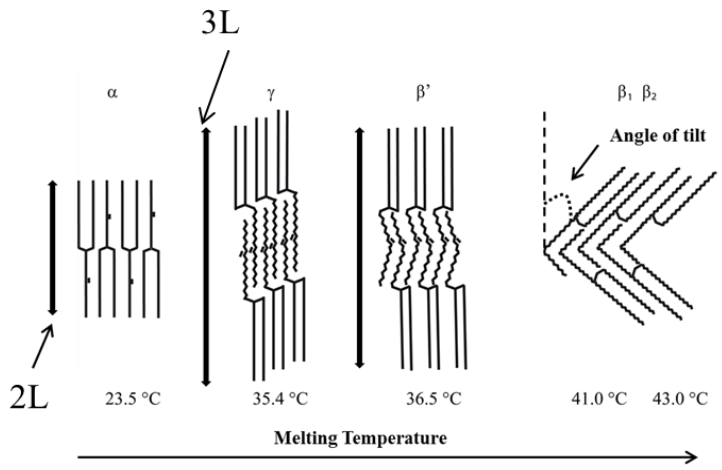

Figure 7: Arrangements of four different polymorphs present in SOS, where S-Stearic acid and O-Oleic acid. The melting temperature changes due to the chain length and angle of tilt [8].

(b) Thermodynamics involved in lipid crystallization:

The driving force for the crystallization process is the difference in the free energy of the supersaturated or supercooled mother phase and the free energy of the newly forming phase. Under constant temperature and pressure, the system goes from a higher to lower Gibbs free energy state. Suppose the binary components, A and B are mixed in a specific ratio, the product for this reaction appears to be in terms of C and D.

$$\boldsymbol{aA + bB \rightarrow cC + dD} \qquad (\mathbf{1.1})$$

However, this is only possible thermodynamically, when,

$$\boldsymbol{\Delta G = (cG_C + dG_D) - (aG_A + bG_B) < 0} \qquad (\mathbf{1.2})$$

This change in Gibbs free energy is denoted as the difference between Gibbs free energy of product (C and D) and reactants (A and B).

$$\boldsymbol{\Delta G = \Delta H - T\Delta S} \qquad (\mathbf{1.3})$$

This change in Gibbs free energy can also be noted as equation 1.3, which is the difference in the enthalpy change (ΔH) and product of temperature (T) and entropy change (ΔS). In case of crystallization from the melt, free energy may also be expressed in terms of temperature difference. At thermodynamically equilibrium state at temperature T_0, the change in Gibbs energy is equal to zero, hence, eq. 1.3 becomes

$$\Delta G = \Delta H - \frac{T\Delta H}{T_0} = \Delta H \Delta T / T_0 \qquad (1.4)$$

Therefore, thermodynamics involved in polymorphic states of TAGs, are to be understood by using a change in Gibbs free energy barrier (Figure 8).

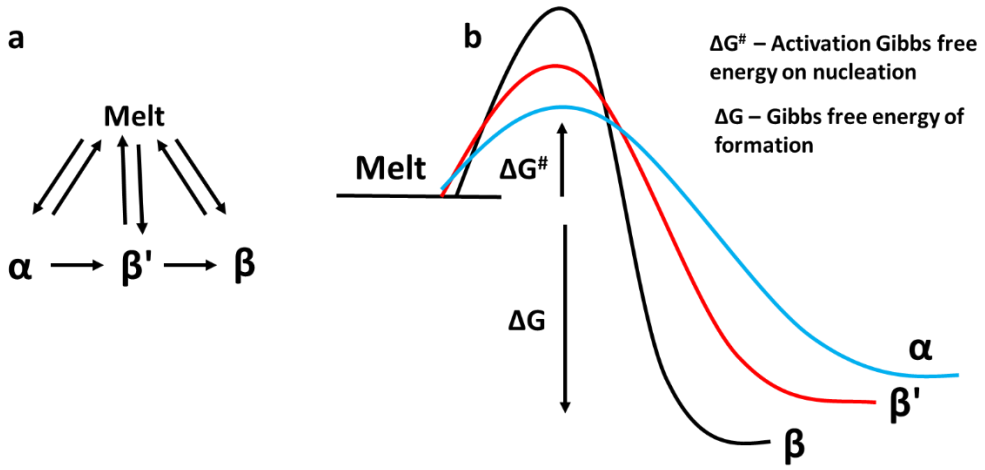

Figure 8: (a) Formation of polymorphs from a melt, and solid-solid transition from metastable form to a stable form. (b) Relation of change in Gibbs free energy to a polymorphic formation from melt [11].

TAGs are relatively large molecules, which take a reasonably long time for long hydrocarbons to align and form stable form. When the molten form of TAG is cooled down to its melting point, the driving force for crystallization is achieved, which is proportional to the extent of undercooling. With low undercooling, the system tries to rearrange and adopt stable packing arrangements for the formation of crystalline solids and decrease the driving force. Whereas provided sufficiently high undercooling to the system, TAGs do not have time sufficient to arrange themselves in a thermodynamically stable configuration, and thus tend to crystallize in metastable or less stable polymorphic form. These thermodynamically less stable forms try to go towards a higher stable form (Figure 8(a)), which corresponds to the lower free energy state. The key concept here is that the metastable forms have a lower activation free energy on nucleation than the more stable form as shown in Figure 8(b). Thus metastable forms more quickly due to kinetic effect. Similarly, the free energy of formation is lower for the metastable state than the stable state. Therefore, due to the kinetic process, the activation energy for nucleation and so the Gibbs free energy for the formation of α form is less as compared to the β form.

(c) Crystallization kinetics:

(i) Nucleation theory: Gibbs-Thomson formulation

Steady-state isothermal nucleation theory is based on Gibbs-Thomson formulation, in which, the overall free energy change is a resultant from the formation of a spherical nucleus, which is the sum of a surface and volume term [18].

$$\Delta G = \Delta G_s + \Delta G_v = 4\pi r^2 \delta - \left(\frac{4\pi r^3}{3V_m}\right) RTln(1+S) \qquad (1.5)$$

Where ΔG is free energy change associated with the formation of the spherical nucleus; ΔG_s is the surface free energy; ΔG_v is the volume free energy (which is a negative quantity, in a supersaturated medium); δ is the solid-liquid surface free energy per unit area (or crystal-melt interfacial tension); R is the ideal gas constant; T the temperature of the blend; S is the supersaturation; V_m molar volume of solid and r is the crystal radius.

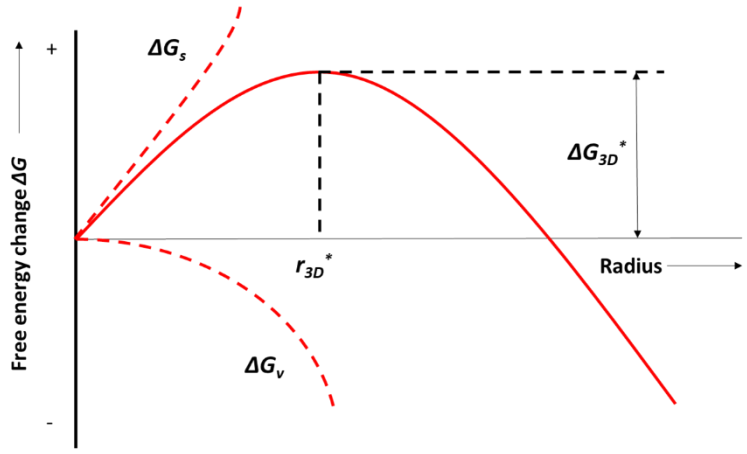

Figure 9: Change in Gibbs free energy as a function of crystal radius [18].

The change in Gibbs free energy is associated with the formation of the nucleus radius. As the ΔG passes through the maximum point, the function $\Delta G_{3D}{}^*$ established at radius $r_{3D}{}^*$, which is called a critical radius. When r is smaller than $r_{3D}{}^*$, the crystal nuclei dissolve into liquid, whereas, if it is larger, the stable nuclei form and grow. The critical size of the crystal nucleus can be determined by calculating the derivation of equation 1.5 and assuming the derivation value is 0. $d\Delta G/dr = 0$. This derivation yields $\Delta G_{3D}{}^*$ and solving this is to obtain $r_{3D}{}^*$.

$$r_{3D}{}^* = \frac{2V_m\sigma}{RTln(1+S)} \qquad (1.6)$$

In terms of change in Gibbs energy, $\Delta G_{3D}{}^{*}$ represents the energy barrier for nucleation and it decreases after a critical size nucleus is formed. Hence, this critical change in Gibbs free energy can be achieved by either increasing supersaturation (S) and temperature or decreasing interfacial tension. This activation energy barrier ($\Delta G_{3D}{}^{*}$), is a measure of 'difficulty' level for embryos to achieve a critical radius of stable nuclei, therefore also helps to derive the nucleation rate J. The nucleation rate is the number of nuclei formed per unit volume per unit time, described as Arrhenius equation:

$$\boldsymbol{J = ASexp\left(-\frac{\Delta G_{3D}{}^{*}}{k_B T}\right)} \qquad (\mathbf{1.7})$$

Where A is a kinetic parameter determined by the attachment of atoms/molecules to the nucleus; S is the supersaturation ratio [20]. The degree of supersaturation of a particular i^{th} TAG in a melt can be quantified by the supersaturation ratio (S),

$$\boldsymbol{S_i = \frac{[C_i]}{[C_i{}^{*}]}} \qquad (\mathbf{1.8})$$

Where $[C_i]$ is the concentration of a particular i^{th} TAG species in the melt under supersaturation condition, while $[C_i{}^{*}]$ corresponds to the equilibrium solubility of the particular i^{th} TAG in the melt under the same temperature and pressure conditions.

(ii) Isothermal Crystal growth- Avrami model

After the nucleation process, the crystal growth of these nuclei takes place. One of the methods to understand this process is with 'Johnson-Mehl-Avrami-Kolmogorow model (Avrami model)'. Avrami model can be used to measure crystallization kinetics along with an understanding of the nature of the crystal growth process [21]–[23]. This equation is based on the assumption that

1) Nucleation occurs randomly and homogenously
2) The growth rate does not depend on the extent of transformation
3) Growth occurs at the same rate in a direction

Hence, the equation of the Avrami model leads to

$$\boldsymbol{\frac{V - V_0}{V_m - V_0} = 1 - e^{-kt^n}} \qquad (\mathbf{1.9})$$

V, V_0 and V_m represents the volume fractions of the solid fraction at specific time t, at time $t = 0$, and maximum fraction obtained at a specific temperature in that period of time respectively; k is the Avrami constant; n is the Avrami exponent. Basically V_0 represents zero value assuming no solid fraction is present at the start of isothermal crystallization and volume fraction can also be represented in terms of mass, hence, for application to the fat crystallization, the Avrami equation transformed to the equation

$$\frac{SFC}{SFC_{max}} = 1 - e^{-kt^n} \qquad (1.10)$$

Where SFC is the solid fat content at a particular time; SFC_{max} is the maximum SFC achieved at a particular temperature [11]. These Avrami parameters give information about the nature of the crystallization process. The Avrami constant (k) is a function of crystallization temperature and considers the relation of nucleation and crystal growth rates altogether. Whereas, the Avrami exponent (n) is an index of crystallization that focuses on the crystal growth mechanism. This is a combination of the function of the time dependence of nucleation and the number of dimensions in which growth takes place. In Table 2, the expected exponent values are shown for various aspects of nucleation and crystal growth.

Table 2: Values of Avrami exponent (n) for various types of nucleation and crystal growth [11].

n	Type of crystal growth and nucleation expected
3+1 =4	Spherical growth from sporadic nuclei
3+0 =3	Spherical growth from instantaneous nuclei
2+1 =3	Plate-like growth from sporadic nuclei
2+0 =2	Plate-like growth from instantaneous nuclei
1+1 =2	Rod/needle/fiber-like growth from sporadic nuclei
1+0 =1	Rod/needle/fiber-like growth from instantaneous nuclei

Nucleation is either instantaneous, with all nuclei appearing at once, or sporadic, with the number of nuclei increasing linearly with time. Crystal growth could be either spherical, plate-like, or needle-like in three, two, or one dimension respectively. Ideally, the exponent value is an integer, however, in reality, the fractional values could also be obtained, due to either the simultaneous development of more than one type of crystal and/or presence of different types of morphologies. Deviations from integer value can also be obtained because of similar crystals from different types of nuclei (sporadic vs. instantaneous). Therefore, the precise interpretation

based on n value is quite difficult hence the microscopic comparison is necessary in order to find the specific crystal growth.

1.3 Fat crystal hierarchy: relation to 'Fractal' nature

Fat crystallization behaves in a hierarchy, which is shown in Figure 10. TAGs stack together to form lamellas of 2L or 3L configuration. The aggregation of these lamellas is due to Van der Waal's attraction forces. These lamellae further aggregate in order to form an ordered structure, which is referred to as 'crystal domain' or 'nanoplatelet'. Aggregation of several domains results in a single crystallite. These crystallites accumulate together to form a primary particle.

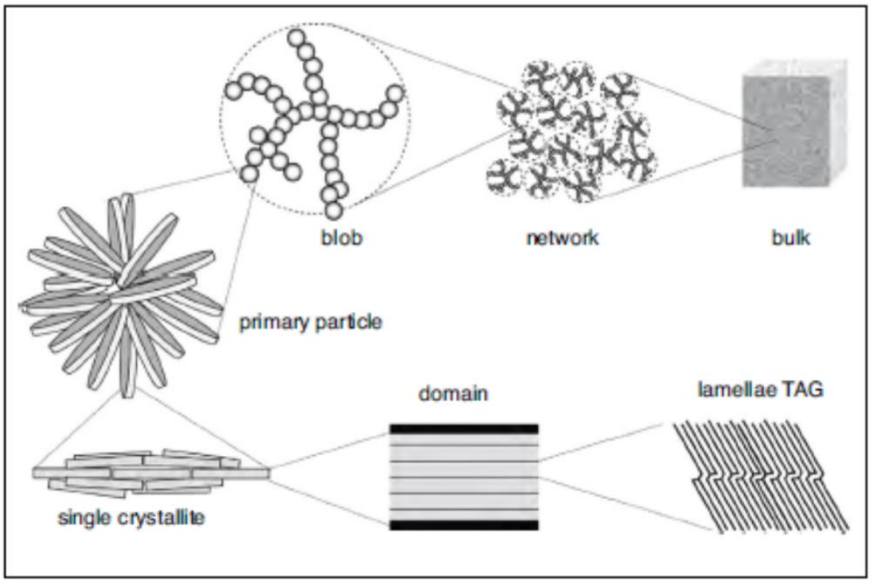

Figure 10: Fat crystal hierarchy shows the different stages where the aggregation of crystal particles occurs [8].

Agglomeration of these primary particles forms a 'blob' structure and later develops a crystalline network. Thus, the fat crystal network shows a resemblance to the colloidal gel particle network, which provides an idea of showing 'fractal nature'. Naturally, fractals can be classified into two types: non-random and random fractals. Non-random fractals represent the 'Sierpinski gasket', which is an aggregation process obtained by simple iterations. Assume, a triangle with unit mass (M) and unit length (L), when joining three triangles together, M =3

and L =2, so if these aggregations continue further, the density measure for each step can be derived by

$$\boldsymbol{\rho(L) = \frac{M(L)}{L^2}} \qquad (\mathbf{1.11})$$

Hence, the density decreases from step 1 (equal to 1) to further aggregations. If the log-log plot of this density as a function of edge length is plotted, the linear size of an object comes as a resultant. Thus, this behavior can also be expressed in terms of the 'power law' mechanism (eq. 1.12).

$$\boldsymbol{M(L) = AL^{d_f}} \qquad (\mathbf{1.12})$$

After inserting equation 1.12 into 1.11, the following equation arrives

$$\boldsymbol{\rho(L) = AL^{d_f-2}} \qquad (\mathbf{1.13})$$

Where, A represents amplitude, which is solely dependent on the definition of M and L, whereas the exponent d_f is the fractal dimension which depends on the iteration process. The slope in the linear plot from density to length scale gives the fractal dimension. In the case of random fractals, the theory of random walk comes into account, and therefore, the relation of mean square displacement as a function of time derives the fractal dimension. The mean square displacement can also be expressed as characteristic length ξ and can be shown as:

$$\boldsymbol{t \sim \xi^{d_f}} \qquad (\mathbf{1.14})$$

Where t is the characteristic time. This relation of characteristic "mass" per unit time to its characteristic "length" gives the fractal dimension value [24]. In terms of fat crystal network, if considers the microscopic images from the initial time 0 to the time when the crystal blobs connect to each other, the characteristic length can be determined. For instance, the point on the one end of the microscopic image is considered and the walk is drawn according to the connectivity between the blobs, it has been observed that with time the connectivity is increased due to an increase in the mass of solids. So the connectivity length is referred as so the characteristic length. Therefore from this relation, the graph between time t and characteristic length can be drawn and the fractal dimension can be calculated. This random walk concept can be useful in the future to determine the exact time for complete crystallization of the samples which takes a long time to crystallize.

Therefore, the fractal dimension in fat crystallization helps to understand the complexity in the crystal structure. As natural fat/oil consists of various types of TAGs, the crystallization

behavior is dependent on the degree of saturation, length of carbon atoms, and the distribution of fatty acids on the glycerol molecule and the cooling process mechanism [8]. These variations in parameters result in a complex fat crystal network. Therefore, it is essential to study this crystal network behavior through understanding the concept of fractality of the crystals, which can be calculated by using rheology, light scattering, and microscopy techniques [11], [25]. Usually, the power law between storage modulus and SFC is used to calculate the fractal dimension in the fat crystal network [26]. For instance, the study of the crystallization of (30%) cocoa butter in canola oil and soybean oil, for the determination of the fractal dimension was calculated by using rheological data and SFC [27]. It is elaborated by the eq.1.15 and 1.16.

$$\boldsymbol{G' = \gamma \Phi^{m}} \qquad (\mathbf{1.15})$$

$$\boldsymbol{m = \frac{1}{3 - d_f}} \qquad (\mathbf{1.16})$$

The storage modulus G' is depending upon the scalar factor γ (which relates to the size of the primary particle and interparticle interaction), SFC and mass fractal dimension d_f. After performing rheological measurements and calculating SFC at different temperature ranges, the results showed that as the crystallization temperature increases, the SFC values decreases and so the fractal dimension d_f. This reflects that the effect of crystallization temperature on fractal dimension can also be studied.

Another method to calculate the fractal dimension is from image analysis. This method describes how space is occupied by a particular curve or shape. The fractal dimension from images can be determined by two methods: 1) box-counting method (D_b); 2) particle-counting method (D_f).

Box counting method (D_b): The principle of this method is to split the image into different box sizes (r) and its relation to the number of boxes which shows the population of white pixels (crystals) (N). The box counting fractal dimension is calculated negative of the slope of linear progression curve of the log-log plot of the number of occupied boxes (N) to the box size (r) [11].

$$\boldsymbol{D_b = -\frac{\Delta \ln(N)}{\Delta \ln(r)}} \qquad (\mathbf{1.17})$$

Particle counting method (D_f): The concept of this method is derived from mass fractal dimension D_m, which relates to the number of particles N to the linear size of fractal object R and linear size of one particle σ.

$$N = \left(\frac{R}{\sigma}\right)^{D_m}, N \gg 1 \qquad (1.18)$$

If the linear size of one particle is assumed to be constant the eq. 1.18 yields

$$N \propto R^{D_f} \qquad (1.19)$$

Where D_f is the particle-counting fractal dimension. The D_f value is determined as the slope of the log-log plot of a number of particles and linear fractal object for varying values of R [28].

The current study implemented the 'box-counting method' and 'Kraus model' derivation to calculate fractal dimension at a specific time by using image analysis and amplitude sweep study respectively. This theory is based on the "Payne effect" initially used for understanding the crystal network in the rubber system as carbon filler particles [29]–[31]. The base of this model assumed that filler network breaks and recombines with various rates, which depend on amplitude and some rate constants. This theory elaborates in terms of a relation of change in storage modulus to the inverse of amplitude. The equation is shown as follows.

$$\frac{(G' - G'_{\infty})}{(G'_0 - G'_{\infty})} = \frac{1}{(1 + K^2(a)^{2m})} \qquad (1.20)$$

Where G' is the storage modulus at a specific amplitude a; G'_{∞} represent storage modulus at infinite amplitude, in this current study case for fitting the data, the value of storage modulus at highest strain amplitude was considered. G'_0 represents storage modulus at initial amplitude (highest value for storage modulus). K is a parameter that consists of system parameters and constants. Exponent m explains the structure of a cluster network made up of filler agglomerates. For determining the fractal dimension, d_f the following relation is used.

$$m = \frac{1}{(C - d_f + 2)} \qquad (1.21)$$

Where spectral connectivity parameter C reflects the cluster-cluster aggregation. Based on the principle of the Kraus model, in this study, the rubber filler network is replaced with a fat crystal network and applies this model for calculating the fractal dimension.

1.4 Mixing behavior in lipid blends

The mixing ratios of a binary system of fat–fat and fat–oil blends determine their solid-liquid phase diagram. The solid-liquid phase diagram helps to understand the differences in the thermal properties of blends when mixed in different ratios. There are typically four different phase diagrams identified by Timms [32]: (a) monotectic continuous solid solutions, (b) eutectic systems, (c) monotectic partial solid solutions, and (d) peritectic systems. If the difference in the melting temperature is large in binary systems, monotectic continuous mixing behavior is likely to occur. In the case of eutectic mixing behavior, both systems, in the phase diagram have different chemical structures, sizes, or polymorphic formation, but similar melting temperatures. Monotectic partial solid solution type of phase diagram is a preference to eutectic behavior but with an increase in melting temperature of binary systems. A peritectic behavior has been found only in one binary system so far, in which mixtures of TAGs have two unsaturated FAs. In Figure 11 typically, two of the aforementioned phase diagrams, which are mostly found in a binary mixture of TAGs are shown.

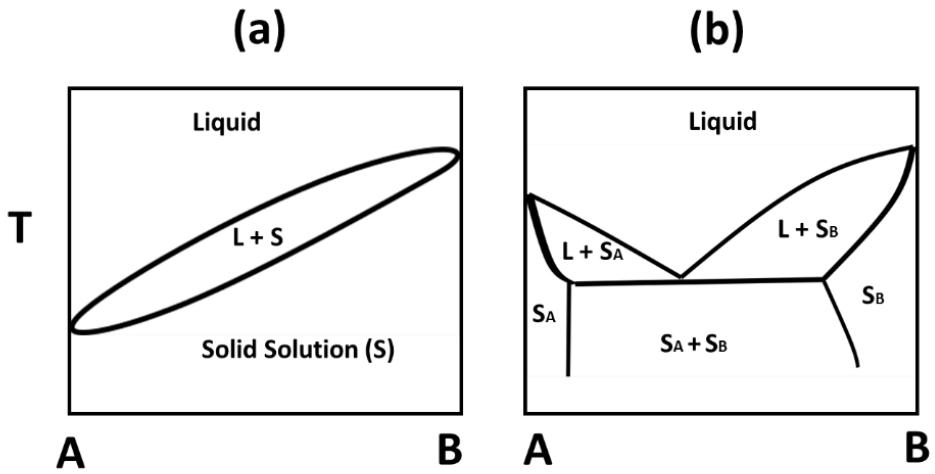

Figure 11: Model schematic of two types of phase diagram in binary mixtures of triacylglycerols (TAGs); (a) monotectic continuous solid solution, (b) eutectic phase behavior (redrawn from [32] with permission).

However, in the case of pure saturated fat, one may have to consider either melt-mediated or solid–liquid-solid (S–L–S) transition or solid-solid (S–S) transition while constructing the solid-liquid phase diagram. Melt-mediated, also known as S–L–S transition, can be explained by the transformation of one polymorph into another via melting. During heating, one

polymorph melts and recrystallizes into another polymorph. On the contrary, S–S transition is the transformation of one polymorph into another form in a solid-state [15]. Understanding such transformations could help to design the technological processes during fat crystallization in food applications.

Furthermore, as fat or oil contains multicomponents, a binary phase diagram is only applicable if ternary or higher number interactions are neglected. Therefore, in this study, a binary phase diagram is implemented in case of CB/TS and CB/CO, and a ternary state diagram for $E_{CB\text{-}CO}$ and derivatives of n-alkanes is plotted.

1.5 Model systems used in this research

This set of study is divided into three parts 1) Cocoa Butter (CB) and Tristearin (TS) mixing behavior; 2) Cocoa Butter (CB) and Coconut Oil (CO) mixing behavior, crystallization kinetics, and rheological properties; 3) CB and CO mixed with n-alkanes along with the eutectic mixture of CB/CO with n-alkanes for understanding the thermal properties, crystallization kinetics, and rheological behavior. The model systems used in this study are explained below.

1) Cocoa Butter (CB)

Cocoa Butter (CB) is a fat manufactured from the cocoa beans during the roasting process. These cocoa beans are taken out from the cocoa tree (*Theobroma cacao L.*), which is also called the 'chocolate tree'. The cocoa tree originates from South and Central America, but now it is grown commercially at most of the places in the world where the temperature is above 27 °C and there is a constant high humidity throughout the year [33]. Hence, the composition of CB differs according to the region of cultivation, climate conditions, etc., and due to such differences in TAG composition, it is a difficult task for industrial personnel to form good food product quality each time. Therefore, it is necessary to study the crystallization behavior of CB more thoroughly since its main application is in chocolate production and its confectionaries. CB consists of mainly monounsaturated symmetrical TAGs, namely POP (1,3-dipalmitoyl-2-oleoyl glycerol), POS (1,3-palmitoyl-stearoyl-2-oleoyl glycerol) and SOS (1,3-distearoyl-2-oleoyl glycerol); where P = palmitic acid, O = oleic acid and S = stearic acid (approximately 17% of POP, 37% of POS and 27% of SOS) [34]. The remaining part consists of mixtures of

monounsaturated and polyunsaturated TAGs, as well as traces of polyphenols and free fatty acids. CB crystallizes into six (γ, α, β_2', β_1', β_2, and β_1) different polymorphs in which melting temperature and their stability increases from γ (17.3°C) to β_1(36.3°C) [35].

2) Tristearin (TS)

TS is a monosaturated TAG composed of three stearic acids (SSS) with 18 carbon atoms each, which crystallizes into three polymorphs namely, α (less stable), β′ (metastable), and β (highly stable) with melting temperatures of 54 °C, 65 °C, and 72.5 °C, respectively [36]. Previous studies were only carried out on the addition of a low concentration of TS to CB. For instance, the study on the effect of 1 wt % and 5 wt % of TS on the crystallization of CB showed the increase in onset temperature of the mixture, and the polymorphic transition from β′ to β was also delayed [37]. However, systematic investigations on higher percentages have not yet been explored; hence, in the present study, the selection of such a combination was used. Interestingly, TS is also present in CB as a minor component [34], and hence, it was intriguing to observe the possible changes that would occur after the blending of TS in a higher percentage with CB.

3) **Coconut Oil (CO)**

Coconut Oil (CO), which is extracted from the kernel of mature coconuts. It consists of a high amount of saturated fatty acids (~90%), with the remainder being monounsaturated and polyunsaturated fatty acids. The TAG composition in CO is of various mixed saturated fatty acids, as- MLaLa, LaLaLa, MMLa, PMLa; where M- Myristic acid C(14:0), La- Lauric acid C(12:0), and P-Palmitic acid C(16:0), but mainly consists of lauric acid (~40%)[38]. After crystallization, these TAGs form polymorphs of α and β' crystalline structure and their melting temperature is very close to the melting temperature of CB [39]. It has also been shown that CO can be used as a cocoa butter substitute [40], [41] as it consists of a high amount of lauric acid (~40%) followed by myristic and palmitic acid [38]. There is a wide range of research studies that have been done previously on mixing behavior and crystallization of CB with lauric fats [42]–[45]. However, the effect of isothermal and dynamic crystallization processes on physicochemical properties and morphological changes of a broad range of CB/CO blends has not been explored yet. Therefore, following this approach will help to determine the exact eutectic point of CB/CO blends.

4) Derivatives of paraffin waxes (long-chain n-alkanes)

To alter the crystallization of this individual fat/oil different additives are used. These additives mainly consist of fatty acid as a hydrophobic part such as monoacylglycerol, sorbitan esters, or sucrose esters [46], [47]. Similar to the aforementioned emulsifiers, another set of additives such as natural waxes also tend to tune the crystallization of different oils. These natural waxes like Candelilla wax, Rice bran wax, Beeswax can be used as additives to form oleogels due to interactions between the molecular composition of waxes and TAGs from oil [48], [49]. Although these natural waxes are used in food or cosmetic industries for the structuring of oil and fat, there are also another set of waxes, which are derived from the petroleum industry such as paraffin wax, microcrystalline wax, which mainly consists of n-alkanes from a range of carbon atom of 18 to 40. The extensive use of paraffin wax (food grade) in chocolate production is due to the shiny appearance and increase in the melting temperature of the chocolate. Even though the use is already been known, the interaction of this wax with TAGs from CB and CO is yet to understand. Hence, in this current study, derivatives of paraffin wax were chosen to understand the interaction between n-alkanes and fat and oil crystals. The n-alkane's type and melting temperature are specified in Table 3.

Table 3: Derivatives of paraffin wax (n-alkane) which are considered in this present study and their respective melting temperatures.

n-alkane	Melting temperature
Icosane (C(20:0))	37°C
Pentacosane (C(25:0))	54°C
Tetracosane (C(30:0))	66°C

1.6 Objectives of the current study

(a) Mixing phase behavior of CB/TS blends in order to understand the effect on thermal and morphological behavior was studied. The variations in thermal behavior in blends were further quantified by obtaining binary interaction parameters. The deep understanding of thermal behavior was further carried out on the basis of microscopic and nanoscale interactions.

(b) Mixing behavior of CB/CO blends for understanding thermal, morphological, crystallization kinetics, and rheological behavior. Moreover, the thermodynamical analysis was also carried out on a binary phase diagram. Furthermore, the interrelation of nanoscopic to mesoscopic relation in fat crystallization was also studied. In order to understand complexity in CB/CO blend crystal network, fractal dimension was also calculated.

(c) Based on results from CB/CO systems, the effect on thermal properties, crystallization kinetics, and rheological properties were studied for the addition of derivatives of paraffin waxes to pure CB, pure CO, and eutectic mixture of CB-CO ($E_{CB\text{-}CO}$).

Hence, to achieve these objectives, the following techniques were used.

1.7 Differential scanning calorimetry

DSC is a thermo-analytical technique, which was used to detect the phase change behavior i.e. changes in melting and crystallization temperature of CB/TS, CB/CO blends, and mixtures with additives from derivatives of paraffin waxes.

Working Principle of DSC

This technique works on the principle of difference in the heat flow between reference crucible and sample crucible while they are subjected to a controlled temperature program [50]. In Figure 12, the general setup for flux DSC is shown. It consists of an oven that has an empty aluminum pan as a reference crucible and a sample crucible with a certain amount of material in it. When a furnace is heated, heat flows to the samples. If the arrangement is ideally symmetrical, the same heat flows to the reference sample. Thus, the differential temperature signal is zero. However, in reality, the steady-state equilibrium is disturbed by sample transition hence, a differential signal is generated. This is described as eq. 1.22.

$$\boldsymbol{\phi_s - \phi_R \sim - \Delta T} \qquad (\mathbf{1.22})$$

Where, Φ_S – heat flow required for sample (W/g), Φ_R – heat flow required for reference (W/g), ΔT – Change in temperature (°C)

When the melting and/or crystallization process occurs, the phase transition heat is measured in the sample with respect to the empty crucible and then recorded as a peak (Figure 13). The

peak area corresponds to the enthalpy change (ΔH) during the process and its direction designates whether the process is endothermic or exothermic.

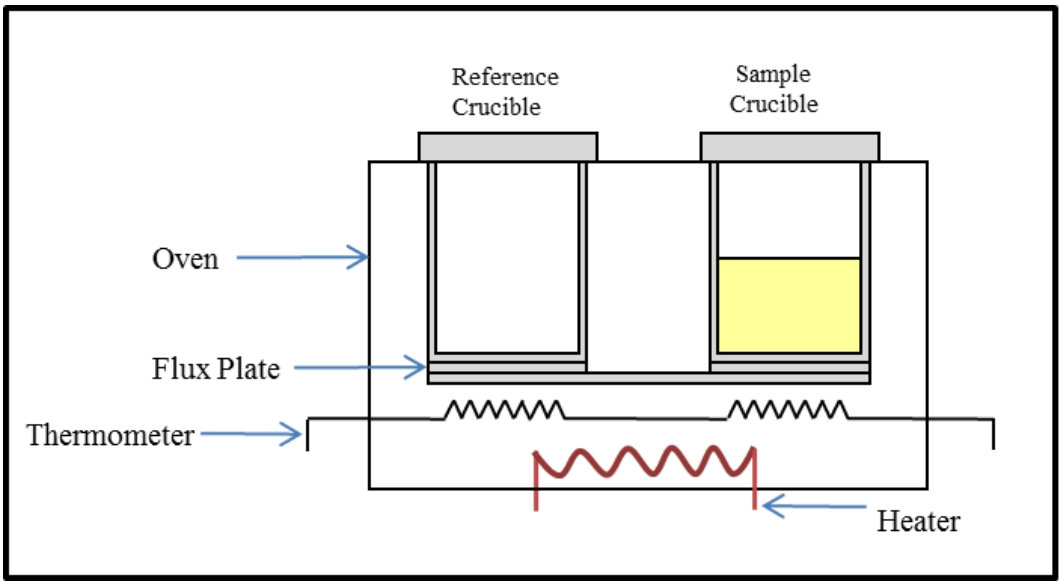

Figure 12: Working Principle of DSC including the general setup [50].

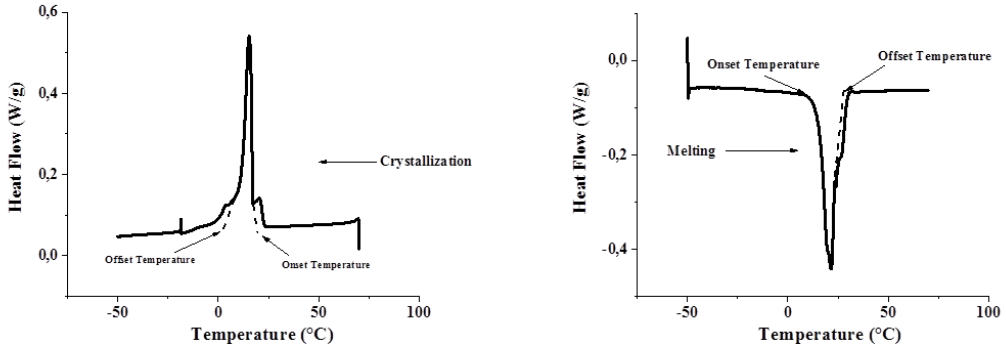

Figure 13: DSC thermograms for phase change behavior; (a) for crystallization process (exothermic); (b) for a melting process (endothermic).

In Figure 13, the graphical representation of normalized heat flow with respect to temperature for crystallization and melting process is shown. In case of the crystallization process, heat is released due to the exothermic process, whereas, the heat is to be taken in the system to carry out the melting process (endothermic process), which is recorded as a peak. The onset and offset temperature represent the start and end of the process (crystallization or melting)

respectively along with peak temperature as the crystallization or melting temperature of the system.

1.8 Polarized Light Microscopy (PLM)

Microscopy was used to observe the changes in crystal morphology of CB/TS, CB/CO, and CB/CO with derivatives of n-alkanes after mixing.

Working principle of PLM

When a beam of ordinary light is incident on the surface of the transparent isotropic sample, the part of the light is transmitted and reflected. These two beams are partially polarized in perpendicular planes and the plane of polarization of the reflected beam lies in the plane of incidence (Figure 14). Polarization is incomplete but reaches a maximum when the two beams are perpendicular, when the reflected beam, but not refracted beam, is completely polarized. The critical angle of incidence for polarization, the polarization angle, is described by Brewster's Law.

$$\tan \theta_c = \frac{n_1}{n_2} \qquad (1.23)$$

Where n_1 and n_2 are the refractive indices of the media above and below the reflecting surface [51]. When a polarized beam of light is incident on the transparent surface, its behavior is dependent on the orientation of the plane or polarization with respect to the surface. If its transverse to the surface, the light beam enters to the material, whereas, if the plane is perpendicular to the surface, the beam is reflected.

The two coherent light rays that are polarized in the same plane however differ with respect to the phase follow the same path in linear vibrations in order to produce elliptical vibrations. Such light is referred as elliptically polarized. Under certain conditions such as: a) when the phase difference between the waves is a quarter or half wavelength, the resultant vibration is circular or linear, hence called as circularly or plane polarized light respectively.

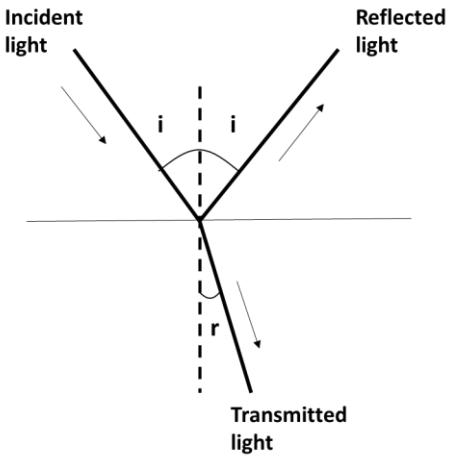

Figure 14: The reflected and refracted beams formed when an unpolarized beam of light falls on a transparent surface are partially polarized in mutually perpendicular planes [51].

Under some circumstances, the state of polarization of the light source is changed when it is reflected or transmitted through a material. This behavior is due to a particular optical property of a specimen, which is called birefringence. This physical property of a material represents the specific refractive index that ultimately defines the way of polarization and propagation of a light beam [52]. In this study, the transmission mode of PLM was used to carry out the experiments (Figure 15 (a)). This experimental setup consists of one polarizer, one analyzer, a condenser lens, tube lens, objective, and sample platform. The polarizer is situated below the sample whereas; analyzer is placed above the objectives. When light source from below, which is illuminating in all direction incident on the polarizing filter, it starts to follow one pathway in one direction. This propagation of light is either in a circular form or in an elliptical form. In this study, the crossed polarization was used with the λ/4 plate (circular polarized light) in between the polarizer and analyzer.

The relation of crystals and transmitted polarized light is shown in Figure 16. When the birefringent specimen is placed under a cross-polarized environment, the extinction occurs when the planes of polarization of the crystal become parallel to those of the polarizers (Figure 16 (b) and (d)). In intermediate positions, light passes through the analyzer becoming gradually more intense until the 45° position is reached (Figure 16 (a), (c), and (e)). Eventually, the crystalline regions of the specimen appear bright which can be seen either through an eyepiece or through a camera shown in Figure 15 (b) (Zeiss Scope. A1 Pol).

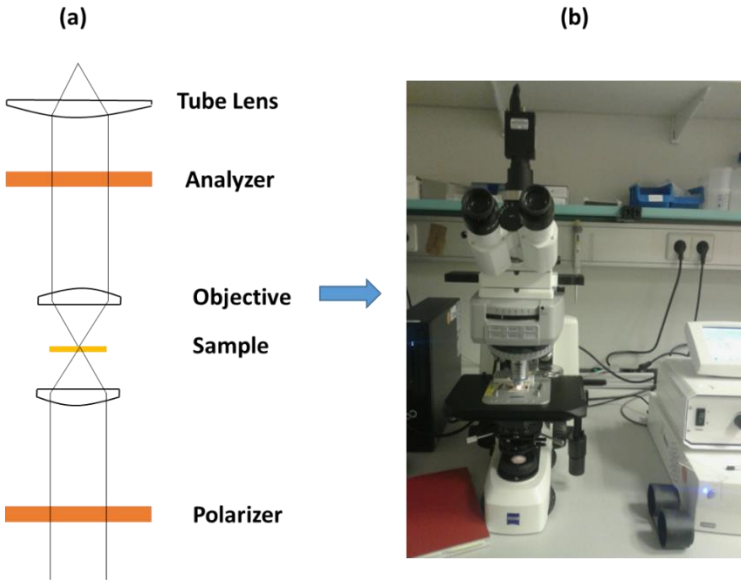

Figure 15: (a) Principle of PLM; (b) Experimental Setup for PLM

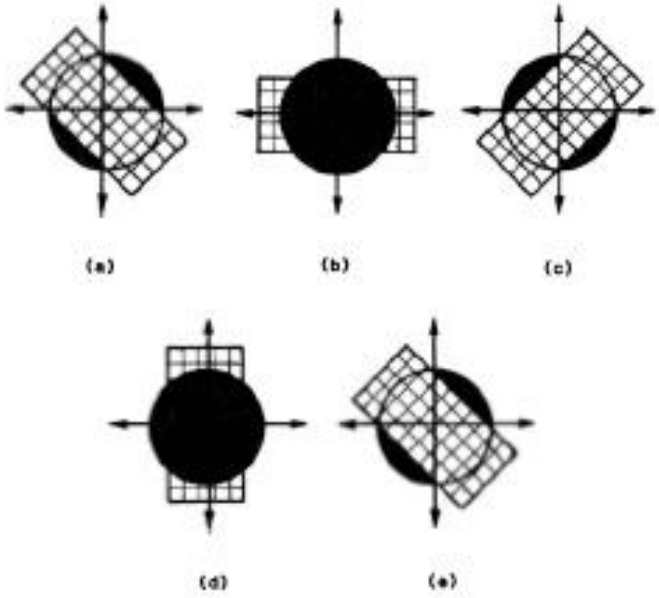

Figure 16: The effect on light transmission of rotating birefringent crystals between crossed polarizer and analyzer [51].

1.9 Coherent Anti-Stokes Raman Spectroscopy (CARS)

Coherent anti-Stokes Raman Spectroscopy was used to understand the mixing behavior of the CB/TS system. This vibrational spectroscopy technique provides information regarding

interactions involved in TAGs in their solid and liquid state. The most sensitive Raman active features in the TAG molecule include C-H and C-C stretching vibrations.

In Table 4, the main modes of vibrations and their respective Raman active wavenumbers are noted for further analysis in order to understand the interactions between CB and TS.

Table 4: List of Raman active modes of vibrations in TAGs and their respective wavenumbers [53], [54].

Modes of Vibrations	Raman active wavenumbers (cm^{-1})
C-H stretching	3000-2700
C=C	~ 1660
CH_2 deformation	1500-1400
CH_2 twisting	1300-1250
C-C skeleton mode	1200-1000
C=O stretching	100-1700
C-D stretching	2175

In the case of the CARS experiment, deuterated TS was used instead of the normal Tristearin to differentiate between C-H stretching from CB and C-D stretching from TS for a better understanding of systems. These regions can provide insight into intermolecular motion, trans and *gauche* conformations of a glycerol backbone, and alkyl chain conformation. Along with the spectral study, the microscopic view of these blends has also been captured for better enlighten of interactions at a microscopic level.

Working Principle of CARS

CARS is a non-linear Raman technique that is used to enhance the Raman signal. In this technique, the coherent laser beams are used to generate a signal with a frequency higher than the excitation frequency, thus called an anti-stoke frequency technique. In the scattering technique, when light incident on a sample with a certain frequency, the photons are scattered in all directions with a certain angle to the incident beam. If this frequency of scattered light is

equal to or lesser than or greater than that of the incident light, the effect is measured as Raman spectroscopy with Rayleigh, Stokes, and Anti-Stokes scattering respectively.

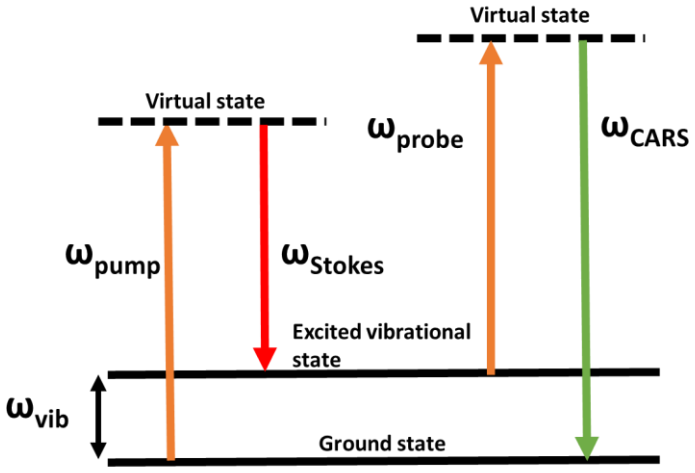

Figure 17: The energy diagram for coherent antistoke Raman spectroscopy [55].

The principle of this technique involved multiple excitation laser sources. This includes pump beam frequency ω_{pump} (ω_p), stoke excitation field frequency ω_{stoke} (ω_s) and probe beam frequency ω_{probe} (ω_{pr}). When incident light focused on the sample and interaction resulted in antistoke frequency ω_{CARS} (ω_{as}), the following equation is used:

$$\boldsymbol{\omega_{as} = \omega_p + \omega_{pr} - \omega_s} \qquad (\mathbf{1.24})$$

A strong signal is produced with a frequency of ω_{as}, when the difference in the frequency of the incident light, is tuned to the Raman active molecular vibration of the sample ω_{vib}. The energy diagram of the CARS technique is shown in Figure 17. On a molecular level, initially, the molecule is at its ground state (lowest energy state). The pump beam excites the molecule to a virtual state, so if the stoke beam is also present simultaneously with a pump beam, the virtual state can be used as a path to the vibrational state (eigenstate) of a molecule. Hence, the molecule is in two states at the same time and thus can be considered to be in coherent superposition states. If this coherence is then probed with probe frequency, the molecule again drives to a virtual state. However, the molecule cannot stay in a virtual state and hence comes back to the ground state with the emission of a photon with a frequency of ω_{as}. This anti-stoke photon emission frequency is dependent on the oscillation of the electron cloud surrounding the chemical bond and hence leads to the difference in frequency according to the functional group.

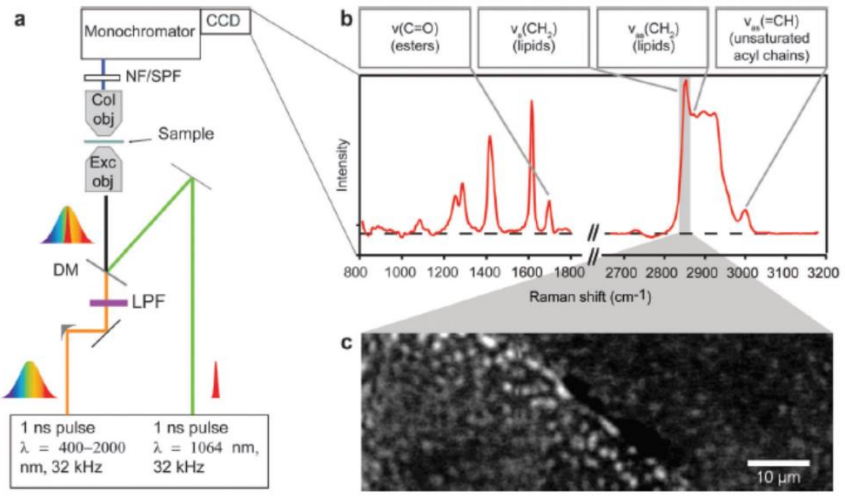

Figure 18: (a) The schematic for CARS microscopy experimental setup, (b) Raman spectra detected (c) spectra with respect to imaging [56].

The experimental setup of CARS microscopy is shown in Figure 18. Pump and probe photons are from the same laser (1064 nm) and stokes laser spans a wavelength range of 1100-1600 nm after being spectrally filtered. These beams are combined by a dichroic mirror (DM), then focused by excitation objective into the sample. The CARS light is collected by the collection of objective and filtered from the Stokes and pump lasers. Monochromator and CCD afterward detect this light. The spectrum after measurement for a certain range of vibrational modes is detected and plotted. At the same time, the 2D image of this sample is captured by using a microscope assembly. These images are allowed to get the spectra for each specific pixel to study in detail the sample interactions.

1.10 X-ray Diffraction (XRD)

XRD technique is used in fat crystallization for identifying the precise polymorphs based on the short spacings. In Figure 19, the typical short spacing values related to hexagonal (H), perpendicular orthorhombic ($O_{\perp}$) and parallel triclinic ($T_{//}$) subcell packing of lipid crystals are shown. In the case of H packing, only one spacing (0.415 Å), $O_{\perp}$ packing depicts two spacings (0.380 and 0.413 Å) and for ($T_{//}$) subcell structure, three spacings (0.386, 0.368 and 0.459 Å respectively) are possible. Therefore, based on these spacings, polymorphism in lipid blends are possible to identify. At the same time, the long spacings (as earlier explained in section 1.2)

give information about lamella spacings. In this study, XRD was used to understand the interaction between CB/TS and CB/CO blends. The changes in long spacings and crystal domain size were determined to understand the effect on mixing behavior due to different mixing ratios.

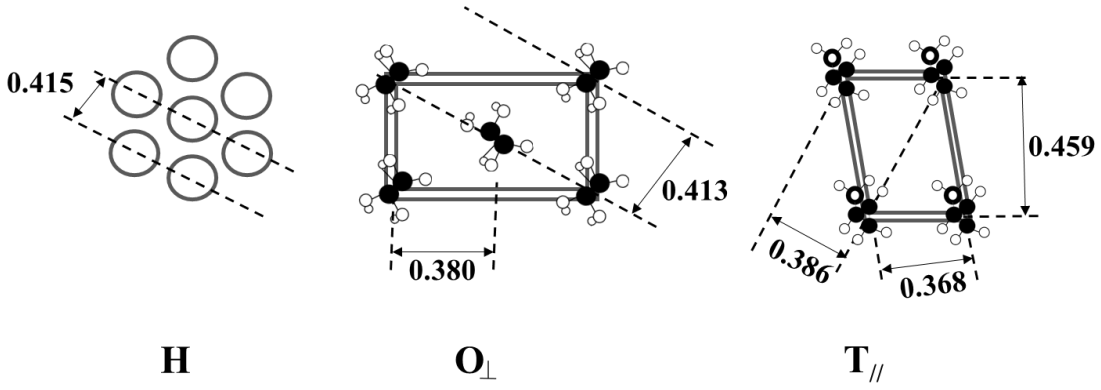

Figure 19: Short spacings for each different subcell structure, which helps to derive the polymorphism (Re-drawn from [15]).

Working Principle of XRD

For crystalline structure, the atoms, or molecules are arranged in an ordered manner, each of these atoms has a nucleus surrounded by the electron cloud (Figure 20 (a)). X-rays are high-energy light (with a certain wavelength) incident on the atoms, the electrons absorb some amount of energy and go to an excited state. When these electrons fall back to the initial state, they emit the same amount of energy at a certain angle of incidence. As the wavelength of the x-ray wave is similar to the distance between the atoms/molecules in the ordered phase, long spacings and short spacings of TAG crystals are possible to calculate by using Bragg's law. In Figure 20 (b), the basic principle for Bragg's law is expressed. The x-ray beam from the source with a certain wavelength (λ) incident on the crystal lattice, the beam scatters with an angle θ. The co-relation between scattering angle and x-ray beam wavelength is shown in equation 1.25, which is called as Bragg's law equation. By rearranging eq 1.25, the long and short-spacing are calculated.

$$n\lambda = 2d \sin\theta \qquad (1.25)$$

where d- Interplanar spacing (nm or Å); λ Wavelength of x-ray beam (nm or Å); θ -Scattering angle (radian)

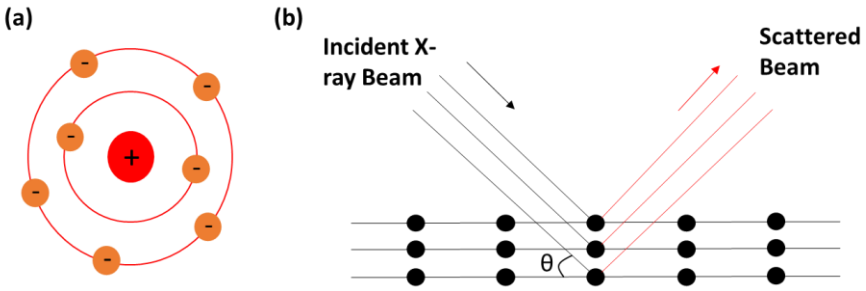

Figure 20: (a) Electron cloud surrounding the nucleus of an atom (b) Schematic diagram representing Bragg's law principle [57].

In Figure 21 (a), the general setup for the experiment is shown. The x-ray generator creates the x-ray beam. The x-rays are produced by an electron bombardment of a water-cooled anode. Copper is often used as a target and after bombardment the electrons get excited, hence the kinetic energy is transformed into photon energy. After reaching to higher energy level the electrons come to their original position and that's when radiation (CuKα) is emitted [57]. This x-ray beam was then incident on the sample with a wavelength (λ = 0.1542 nm, Copper as a target) and later it is diffracted with an angle of 2θ. This diffracted beam was detected by a 2D detector, which is shown in Figure 21 (a). Afterwards, the diffractogram was plotted between intensity and 2θ by using Datasqueeze software (Figure 21 (b)). Based on the diffracted angle, the long and short-spacings are to be calculated. The angle between 0 to 5° is to be associated with long-spacing and above 5° angle for illustration of the short-spacing in the crystal structure.

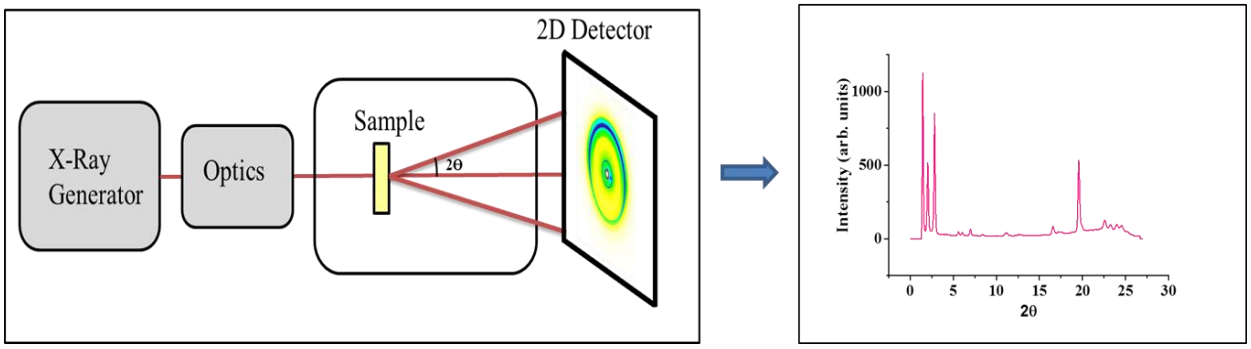

(a) **(b)**

Figure 21: (a) Experimental setup of XRD; (b) Diffractogram.

The small-angle x-ray patterns are usually represented in terms of scattering vector (q) as a function of scattering intensity.

$$q = \frac{4\pi \sin\theta}{\lambda} \qquad (1.26)$$

1.11 ^{1}H Solid State Nuclear Magnetic Resonance (SSNMR)

This particular technique was used in this study to understand the crystallization kinetics in terms of SFC over the period of time. SFC value was calculated based on ^{1}H NMR spectra. As the sample was solidifying the spectra showed a sharp peak for the mobile phase and a broad regime for the solid phase. Based on integration over the peak area, the solid phase (SFC) was calculated over the period of time.

Working Principle

The ^{1}H NMR works on the principle of calculating the resonance frequency of the nuclear spin of a hydrogen atom and its dependence on the strength of the magnetic field at the nucleus. In the case of non-mobile or very fewer mobility samples, the anisotropic local fields or their interactions plays a crucial role in the susceptibility of nuclear spins. The basic concept of understanding this resonance is given by Einstein Planck's Equation.

$$\Delta E = hf \qquad (1.27)$$

Where, ΔE represents the photon energy difference between the equilibrium state (α state) and excitation state (β state) of the H atom after providing electromagnetic field to the sample.

h is a Planck's constant = 6.626*10^-^{34} J.s

f is an operating frequency of light source in Hz.

This operating frequency is further represented by using Larmor precession [58]

$$f = \frac{\gamma B_0}{2\pi} \qquad (1.28)$$

γ represents the gyromagnetic ratio for 'H' atom which is the ratio of its magnetic moment to its angular momentum (radian per second per Tesla); B_0 is an applied magnetic field in NMR (Tesla)

Figure 22 shows the cross-section view of the NMR machine. The NMR machine mainly consists of a radio frequency (RF) generator, a probe carrying sample holder (rotor), a magnet (N-S) surrounded by a liquid N_2 environment (as magnet needs lower temperature for

operating), an amplifier, and a detector for converting signal and noticing the spectrum respectively.

In Figure 23 the effect on the proton of the sample is shown after inserting it into the NMR machine. The sample contains a hydrogen atom at different places in the molecular structure, which are shielded with different electron density due to the place in the triacylglycerol molecule. The hydrogen atom acts as a magnet, hence noted as a magnet bar with N and S poles. The electrons flow from N to S direction hence noted with a blue arrow. Due to differences in shielding two types of models are shown. The black arrow represents the direction magnetic field in the hydrogen atom. Therefore, the orientation of these magnets is different in the sample depending on the conformation of the sample at the equilibrium state. After applying an external magnetic field in the NMR machine, the magnets in the sample orient themselves in the direction of the magnetic field (which is represented as orange arrows). This state is called as 'α state'. Now to spin these magnets in samples to 180°, external energy is required. This energy is provided by a light source (RF generator) with a certain electromagnetic field. After providing this electromagnetic field, the magnets in the sample spins in the opposite direction of a magnetic field by NMR machine. This state is called as 'β state'. The energy difference in α to β state is given by ΔE in eq 1.27. Therefore, as per the energy required for these protons to achieve β state, the spectra are achieved at a different position with respect to chemical shift.

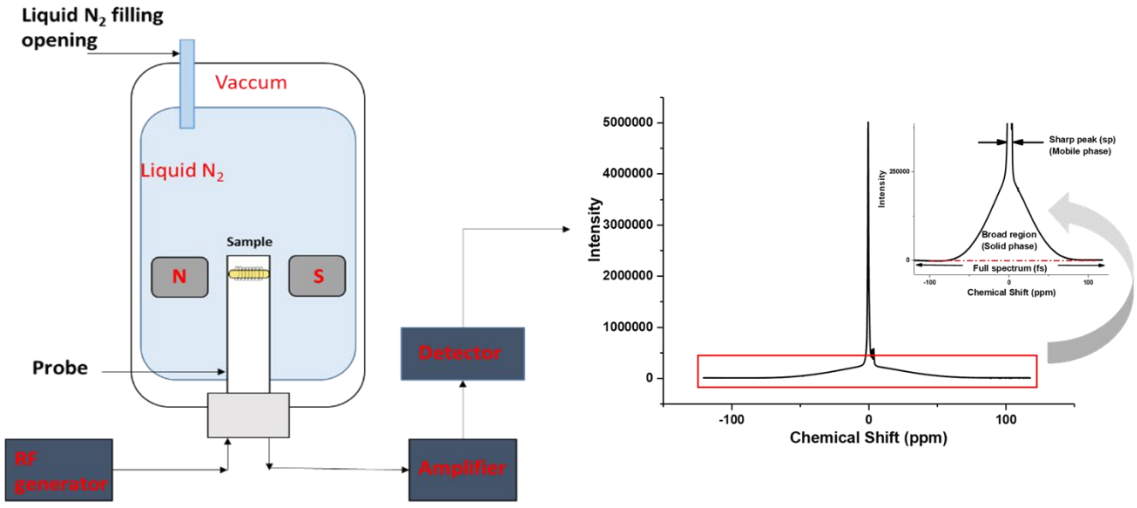

Figure 22: Experimental setup of SSNMR.

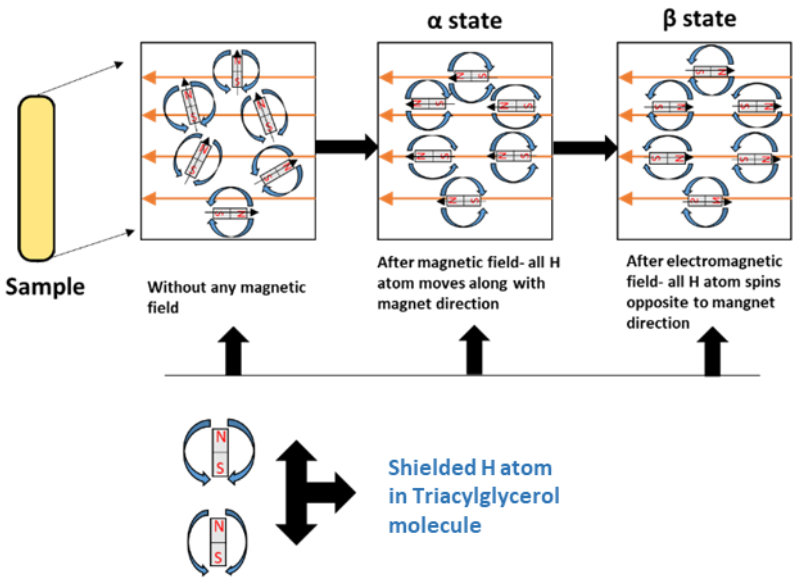

Figure 23: Principle of NMR technique.

But in the case of solid samples, the broadening effects are observed due to additional interactions which are chemical shift anisotropy, dipolar coupling, conformation effects, and quadrupole splitting. To conquer these broadening effects, the Magic Angle Spinning (MAS) method was used in the present study. In this case, the sample spins with a certain angle to an applied magnetic field to achieve the average effects due to the above-mentioned interactions. In Figure 24, the spinning of the sample with a certain frequency at angle Θ to a main magnetic field (B_0) is shown.

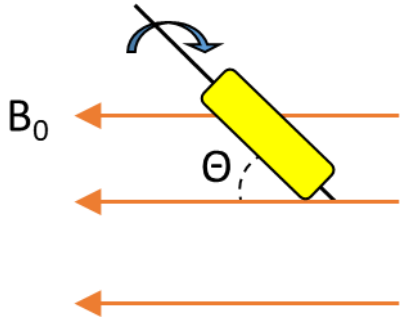

Figure 24: Principle of magic angle spinning.

Therefore, as the sample solidifies, the spectrum divides into a broad regime and sharp peak, which represents, the interaction in the solid phase and mobile phase of the sample to NMR. Thus, the distinction between the mobile and non-mobile phase for the determination of solid fat content is easily obtained.

1.12 Oscillatory Rheology

This technique was used in the current study to understand the crystallization kinetics under a constant oscillatory strain environment and compare the result with the quiescent crystallization kinetics of CB/CO and mixtures of CB, CO, and eutectic of CB-CO with derivatives of paraffin wax. After crystallization under uniform oscillation, amplitude sweep was performed on the developed crystal network of the mixtures for understanding the behavior of fat mixtures using small and large amplitude.

Working Principle

The experiments were performed by using the principle of oscillatory shear rheometry. When torque (stress) is applied to a sample at an angular frequency (ω), the change in displacement (strain) occurs. The amount of change in displacement with respect to the applied stress ultimately gives the viscoelastic property of the material and this response is observed in terms of a sinusoidal waveform (Figure 25). The equation below is given for oscillatory shear rheometry.

$$\gamma = \gamma_0 \sin \omega t \tag{1.29}$$

$$\sigma = \gamma_0 \left(G'(\omega) \sin(\omega t) + G''^{(\omega)} \cos(\omega t) \right) \tag{1.30}$$

$$\tan(\delta) = \frac{G''}{G'} \tag{1.31}$$

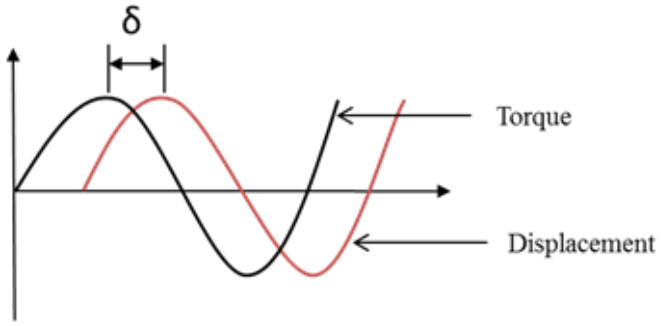

Figure 25: Sinusoidal waveforms for torque and displacement.

Where, γ = strain, ω = angular velocity (rad/sec), σ = stress (Pa), G′ = storage modulus (Pa), G″ = loss modulus (Pa), δ = phase angle (°).

Phase angle distribution represents the type of material characteristic, i.e. δ=0° represents the purely elastic material (ideal solid) and if δ=90°, it behaves as a purely viscous material (ideal

liquid). The condition where, δ is in between 0 to 90° i.e. 0 < δ < 90°, the material shows the viscoelastic characteristic, and at 45°, it represents the boundary of solid-like and liquid-like behavior (which means the start of nucleation process in case of lipid systems). After measurement of the sample, the results can be obtained in terms of storage modulus (G′) - modulus of elasticity i.e. storage of energy; loss modulus (G″) - viscous modulus i.e. energy dissipated as heat; and measure of damping (tan (δ)), which is the ratio of loss modulus to storage modulus [59].

(a) Non-optical rheology

A cross-hatched parallel plate rheometer was used to understand the crystallization behavior under shear conditions. In Figure 26 (a), the general setup for the parallel plate is shown. In which the lower plate is fixed and the peltier heating/cooling system is attached to it, whereas the upper plate is moving with an angular frequency (ω).

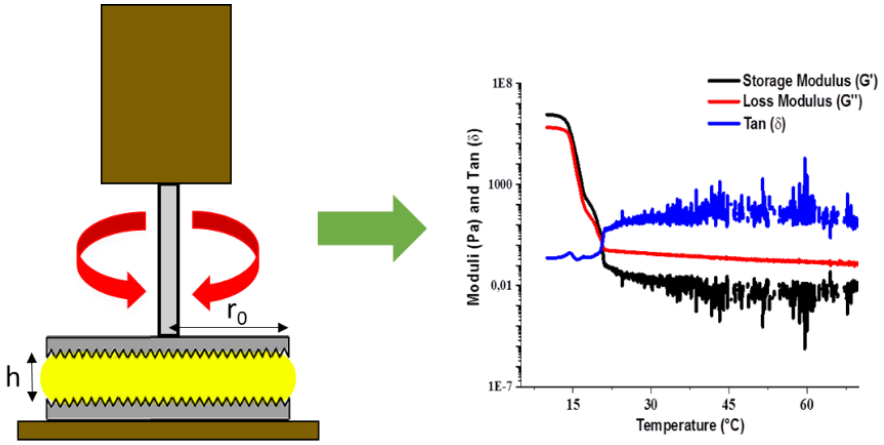

Figure 26: (a) General experimental setup for cross-hatched parallel plate rheometry; (b) Graphical representation of measured data of the sample.

This parallel plate geometry consists of two disks with a radius of 'r_0', separated by a gap of 'h' assuming steady, laminar, and isothermal flow. The shear stress can be determined by measuring the torque M.

$$\sigma = \frac{3M}{2\pi {r_0}^3}\left[1 + \frac{1}{3}\frac{d}{d}\frac{\ln M}{\ln \dot{\gamma}}\right] \qquad (1.32)$$

The shear rate can be derived from the angular velocity, the radius of the disk, and the gap between the plates

$$\dot{\gamma} = \frac{\omega r_0}{h} \qquad (1.33)$$

After doing the measurements, the response of G′, G″with respect to temperature, time, and oscillation strain is recorded. The graphical representation of the temperature sweep is shown in Figure 26 (b).

(b) Rheo-microscopy

To visualize the crystal formation during oscillation, the optics were attached as an accessory to the rheometer. The rheology working principle is the same as explained in section 1.11, for the microscopy principle, the reflected polarized light microscopy module was used for visualization of crystals. Therefore, the working principle for this method is a combination of rheology and polarized light microscopy techniques. The assembly of this unit accessory consists of a lower glass plate, upper stainless steel plate, objectives, camera settings, an external source to control light intensity, upper plate heating/cooling mechanism working on the water source (Figure 27). The sample is placed in between a glass plate (lower plate) and the temperature is managed through the upper peltier plate.

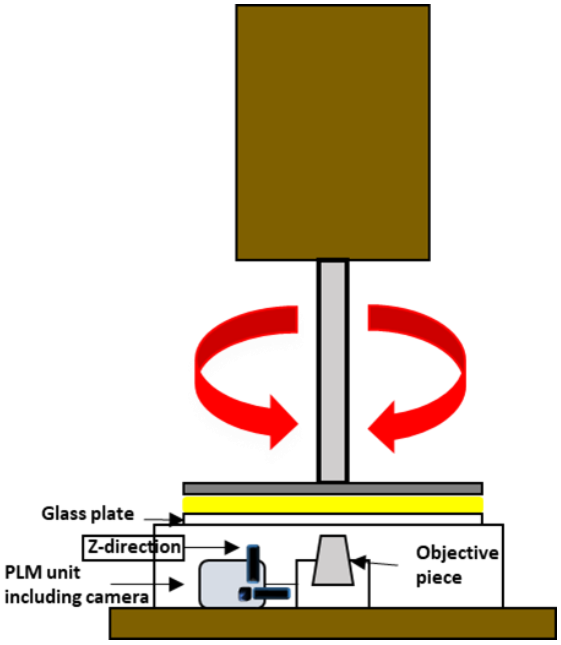

Figure 27: General experimental setup for rheo-microscopy with smooth parallel plate geometry.

Chapter 2: Materials and Methods

2.1 Materials and Blends preparation

CB (Carl Roth GmbH + Co. KG, Germany), CO (Sigma-Aldrich GmbH, Germany), C (20), C (30) (Alfa Aesar), and C (25) (MP Biomedicals, LLC) were used as a model system to study the mixing behavior in CB/TS, CB/CO and $E_{CB\text{-}CO}$ with n-alkanes blends. CB/TS and CB/CO blends were prepared at ratios from 100 w/w % to 0 w/w % in steps of 10 wt% for each experiment. For the preparation of samples, CB and other fat was melted individually for 15 minutes and then added together, this mixture was further heated for another 30 minutes while stirring. Later, the mixture was transferred into a preheated sample holder. Subsequently, the sample was heated again for 15 minutes in the oven for eliminating the crystallization due to temperature difference while transferring the sample. After preparing a sample, it was stored for 24 h at 22 °C in a constant climate chamber (Binder KMF115) with 0% of relative humidity prior to DSC, PLM, CARS, and XRD experiments. For crystallization kinetics studies, after heating to 90 °C, the sample has been moved to sample holders of NMR and rheometer. A similar process was used in the case of $E_{CB\text{-}CO}$ blends with n-alkanes as the preparation of CB/CO blends with the additional step of mixing n-alkanes in CB.

2.2 Compositional Analysis of CB and CO

The fatty acid analysis of CB and CO was determined by GC-FID commercially (Company A, name not mentioned due to confidentiality agreement) and TAG composition of CB was resolved by HPLC analysis commercially (Eurofins Analytik GmbH, Hamburg, Germany).

2.3 Thermal analysis by Differential Scanning Calorimetry (DSC)

DSC was used for thermal analysis of mixtures. The blends were prepared as explained in section 2.1 and then stored in an aluminum crucible (~10 mg to 20 mg sample) for 24 hours at 22 °C prior to DSC (Mettler Toledo DSC3+/700/453) measurements. An empty 100 µL Aluminum pan was considered as a reference cell. Liquid nitrogen was used for cooling at a rate of 30 mL/minute. The experiment was performed in four segments to study the thermal properties of fat/oil blends crystallized via isothermal and dynamic processes. The sample, which crystallized by the isothermal process at 22 °C, was heated firstly to 90 °C to study the

crystal formation after 24 h and kept for 20 minutes for erasing all crystal memory. Later, the sample was cooled down to -50 °C and immediately heated to 90 °C in the next segment. In this study, the peak temperature considered as the melting/crystallization temperature of the system, and the onset and offset point denote the start and end of the thermal process. For a better understanding of the DSC profile, the heat flow parameter is increased in steps of 0.2 W/g in each sample measurement while plotting in the result and discussion section. The analysis was performed in triplicates and the evaluation of the graphs was carried out in STARe software. Moreover, the binary and ternary plot was constructed by using OriginPro software to understand the melting behavior for CB/TS and CB/CO blends and ternary mixing of CB-CO and n-alkanes respectively.

2.4 Thermodynamic analysis of pseudo-binary phase diagram

The phase behavior of binary systems has been explained in detail for fatty acid mixture and phospholipids by using ideal mixing and non-ideality of mixing [60]–[62]. For ideal mixing behavior, the Hildebrand equation is used to simulate the liquidus line derived from the phase diagram [61], [63]. According to this model, the liquidus line of a binary mixture of components A and B being completely immiscible in the solid phase is given by either of the two equations (Eq. 2.1 and 2.2), depending on their composition range [63], [64].

$$\ln x_A = -\frac{\Delta H_A}{R}\left(\frac{1}{T} - \frac{1}{T_A}\right) \qquad (2.1)$$

$$\ln x_B = -\frac{\Delta H_B}{R}\left(\frac{1}{T} - \frac{1}{T_B}\right) \qquad (2.2)$$

Where R is the gas constant, x_A, ΔH_A, T_A represent, mole fraction, molar latent heat of fusion, and a melting point of A respectively, similarly, x_B, ΔH_B, T_B for component B.

On the other hand, the non-ideality of mixing is described by the Bragg-Williams approximation. This equation is based on the non-ideality parameter χ, which explains the interaction between two components in liquid and solid-state. χ is the energy difference between pair (A-B) and the average of (A-A) and (B-B) pair and is described as

$$\chi = z\left(u_{AB} - \frac{(u_{AA} + u_{BB})}{2}\right) \qquad (2.3)$$

Where z is the coordination number, i.e., the number of nearest-neighbor molecules of the individual molecules and u_{AB}, u_{AA} and u_{BB} are the binary interaction energy of pair A-B and

pair A-A and B-B, which describes the interaction of either component in a liquid or a solid phase. For ideal mixing, the difference is zero therefore, χ is zero. Positive χ indicates clustering of similar molecules, which beyond some critical value leads to phase separation into phases of different compositions. Negative χ denotes a tendency for order [61]. The two equations which are shown below represents the Bragg-Williams approximation of non-ideality

$$\ln x_A + \frac{\chi(1 - X_A)^2}{RT} = -\frac{\Delta H_A}{R}\left(\frac{1}{T} - \frac{1}{T_A}\right) \quad (2.4)$$

$$\ln x_B + \frac{\chi(1 - X_B)^2}{RT} = -\frac{\Delta H_B}{R}\left(\frac{1}{T} - \frac{1}{T_B}\right) \quad (2.5)$$

For monotectic behavior, either of the two equations is simulated to obtain the liquidus line, whereas, for eutectic mixture, for composition range between $x_E \leq x_A \leq 1$ equation 2.4 is used and for $0 \leq x_A \leq x_E$ equation 2.5 is used.

In this study, the A and B components indicated as TS and CB in CB/TS blends respectively, and CB as A and CO as B in CB/CO blends. For the calculation of mole fraction of CB and CO, the average molecular weight was calculated based on the TAG profile of both lipids. The TAG profile for CB is evaluated as given in chapter 3 and for CO the TAG profile was taken from the study of Toro-Vazquez group study on physicochemical properties of trans-free and partially hydrogenated soybean oil [65]. The calculated average molecular weight of CB, CO, and TS are 822 g/mol, 627 g/mol, and 890 g/mol respectively. For fitting these equations to the phase diagram derived from DSC, OriginPro 9.1 software was used.

2.5 Morphological studies by Polarized Light Microscopy (PLM)

Morphological Studies: The morphology of the samples was studied by PLM (Zeiss Scope. A1 Pol). 10 µL of the sample was pipetted to a preheated microscope slide and carefully the coverslip was placed on the top of the molten sample to avoid air bubble formation. These slides were stored at 22 °C for 24 h prior to PLM. The pictures were captured after 24 hours for each sample and the result of dynamic crystallization was studied by using a temperature profile similar to the one used in DSC analysis. The heating and cooling were attained by a peltier plate setup (Linkam, model PE120). The sample was heated to 90 °C with a 2 K/minute rate and kept isothermally for 60 minutes to erase the crystal memory. As the heating systems are different in DSC and PLM, a longer isothermal heating time at 90 °C was used as compared

to DSC. Afterwards, the sample was cooled down to 10 °C with a 2 K/minute rate and at this temperature, the pictures were captured by using objective 10x and 20x. All measurements were carried out in duplicates.

Fractal dimension: To calculate the fractal dimension from images, MATLAB software was used. The automated program was used on multiple images to compute the fractal dimension based on box-counting principle. The basis of this program is on the principle of the box-counting method, where the image is split into different box sizes and the number of black pixels is measured in that box size. In the beginning, the image is divided based on 2N (scaling factor), where N represents the real number series starting from 0 to N until 2N equals the dimension of total image size. Therefore, the slope of the logarithmic graph between numbers of black pixels in each box to the size of the box (scaling factor) will estimate the box fractal dimension D_b. This MATLAB code was modified from code developed from [66]. The MATLAB code is shown in section 'Matlab and Python code for data analysis'.

2.6 Coherent Antistokes Raman micro-spectroscopy (CARS)

Raman Spectroscopy: For this study, a nanosecond-based broadband coherent anti-stocks Raman scattering (CARS) spectroscopy was used. The detail of the setup has been described in detail previously in [56], [67], [68].

Sample Handling: Three samples were prepared in order to carry out the study. Pure CB, Deuterated TS (dTS), and CB (50wt%) + dTS (50wt%) mixtures were prepared as explained in section 2.1. One drop of liquid lipids was dropped on glass (24 mm x 60 mm #1 MENZEL-GLASER), and immediately covered with another glass (20 mm x 20 mm #1 MENZEL-GLASER). The glass lipid composite was cooled down at room temperature overnight before the glass composite was mounted on the CARS microscope home-built temperature-controlled stage. A housemade peltier (Quickcool) heater/cooler with a size 30 x 30 x 3.8 mm heat transferring at 8.3 V, 6.5 A and a power of 31.4 W, and the peltier controller was a TE-Technology Model TC-48-20. The sensor was equipped with a 10k Ohm NTC. Overall, the working temperature range in the laser chamber (room temp 22 °C, and humidity controlled environment) was from -15 °C to more than 100 °C with the stability of 0.1 °C. Although the TC-48-20 controller regulates the output power to the TE device (or DC heater) using pulse-width modulation and was not increased linearly, however, the stepwise heating-cooling-heating was carried out with a very small step to the target temperature to ensure no temperature

was above the target temperature. The whole process was executed from 22 °C to 90 °C; 90°C to 10°C and 10°C to 90°C respectively. After reaching the temperature, a 3 min waiting time was applied for heat equilibrium. Samples were placed and pressed down with two clamps on the copper stage, which conducted thermal energy flowing in and out. However, a 3 mm diameter hole was designed to transmit light in the center. The temperature difference was less than a one-degree difference in the center by measuring with a thermal couple after the equilibrium.

Spectra Acquisition: The CARS spectra and hyper images were taken for pure samples and CB-dTS mixture with temperature ramp respectively. The temperature ramp was based on the thermal event of DSC results, and the order was as following: The melting process started at 22 °C (room temp), 45 °C, and 90 °C, continuing with a slow cooling process (room temperature heat dissipation, nonlinear decreasing), which carried on from 22 °C, 10 °C, and the second melting process started 22, 30, 45, 50 °C. The sample was heated up and waited an additional 3 min for equilibrium before each measurement. Moreover, the exposure time for each measurement was adjusted depending on the strength of the signal to avoid the nonlinear effect from saturated CCD.

Data Processing: Nonlinear coherent Raman scattering spectra consist of a resonant and nonresonant component. Liu et al. showed a method of extraction of the resonant component, which reproduced precisely the Raman signal in numerous demonstrations [69]. Raw data was processed, and the spectra were retrieved. In addition to the spectra, hyperspectral images were plotted by the integration of 2000 cm-1 to 2200 cm-1 for carbon-deuterium vibration modes, which stands for deuterated TS, and 2800 cm-1 to 3000 cm-1 for carbon-hydrogen vibration modes, which represent normal CB. The carbon deuterium distribution images were colored in red and carbon-hydrogen distribution images in green. Two images were merged by ImageJ.

2.7 X-ray Diffraction (XRD)

X-ray scattering: The data was measured in transmission geometry using Cu K_α, $\lambda = 0.154$ nm radiation (Rigaku MicroMax 007 X-ray generator). The sample was contained in a 1.5 mm thick glass capillary (wall thickness 0.01 mm). Capillaries were placed in a Linkam stage setup (HFS-X350) and a temperature-controlled copper holder inside a vacuum tube for wide and small-angle scattering experiments respectively. The cooling temperature series was organized by using a liquid N_2 setup linked to the Linkam stage. Scattering data was recorded on an online

image plate detector (Mar345, Mar Research) at a sample-detector distance of 352 mm and 2089 mm. The general experimental setup is shown in Figure 28. Background from high-energy radiation was removed by a Laplace filter-based masking algorithm. Scattering patterns *I (q)* vs. momentum transfer *q* (Eq. 1.26) were obtained by radial averaging of the 2D-scattering patterns.

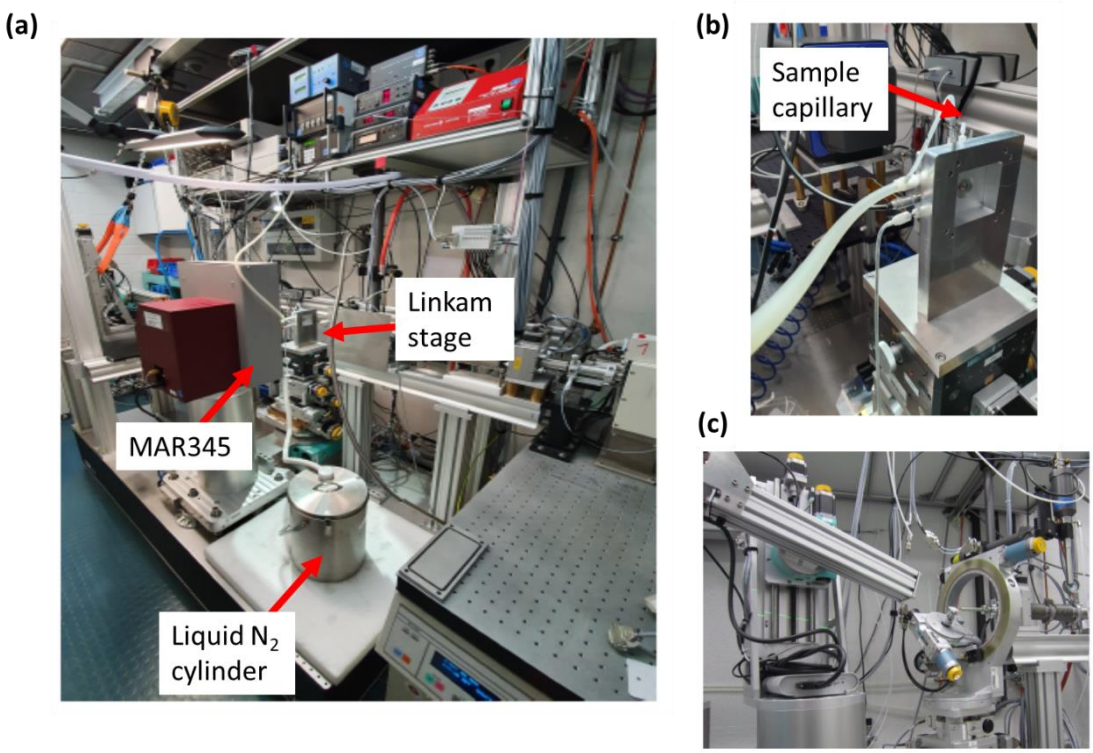

Figure 28: (a) General experimental setup of XRD; (b) Linkam stage with sample capillary; (c) diffractometer setup.

Sample handling: To understand the effect of CB on TS, similar to CARS experiments, pure CB, pure TS, and CB (50wt%) + TS (50wt%) mixtures were prepared as explained in section 2.1., after preparation of lipid blends as explained in section 2.1, the sample was poured into a preheated capillary at 90 °C and kept the sample at 22 °C for 24 hrs. Prior to XRD experiments of samples, calibration was conducted by using 'Silver Behenate sample'. The stepwise heating and cooling segments were carried out at the rate of 10 K/min. Instead of a 2 K/min, 10 K/min temperature ramp rate was used in this technique in order to achieve a better result. As this is a stepwise measurement, the data during ramp was not able to be captured, hence the fast ramp rate was used. Different temperatures were selected between 22 °C to 90 °C for 1st heating segment. After reaching 90 °C, the sample was cooled to 0 °C with the aforementioned rate,

and then the re-melting segment was carried out, by stepwise heating. To complete one spectra measurements, the incident time of x-rays was 300 s, and detection & recording of this scattering data required 90 s. Hence, due to high measurement time, in the case of x-ray measurements, the stepwise cooling was skipped to preserve the precise understanding of changes in long spacings in CB/TS blend. All the experiments were carried out only once.

Data processing: After recording these data, the radial averaging of the 2D pattern was carried out by using *Datasqueeze* software. This data was further analyzed by creating an automated program for the calculation of crystal domain size and long spacings after Gaussian fitting to the peak spectra by using *Python 3* program. The Python code is shown in section 'Matlab and Python code for data analysis'.

The crystal domain size was calculated by using Scherrer equation [70]

$$\boldsymbol{D = \frac{K\lambda}{\beta \cos \Theta}} \qquad (\mathbf{2.6})$$

D is a crystal domain size (Å); K represents the shape factor, usually considers close to 1 for perfectly spherical crystal shape, but varies with a particular crystal shape. In this study, the typical 0.9 was considered for calculation; λ is the x-ray wavelength (1.54 Å); β is full width at half maximum (FWHM) value derives after fitting the peak spectra (radians); Θ is a Bragg angle.

2.8 ^{1}H solid-state NMR

NMR: The NMR experiments have been performed with a Bruker Avance III console operating at 500.22 MHz ^{1}H Larmor frequency at a Bruker superconducting 11.9 T wide bore magnet system using a commercial static ^{1}H/X static solid-state NMR probe. Spherical sample shape was chosen using 4 mm HR-MAS rotors as sample holder, in order to reduce susceptibility artifacts. The ^{1}H rf nutation frequency was adjusted to 62.5 kHz, corresponding to a 90° pulse length of 4 µs. The temperature was adjusted using a Bruker BSVT temperature controller with an accuracy of +/- 0.1 K, which was calibrated using the temperature-dependent chemical shifts of methanol and ethylene glycol.

Sample handling: The blends were prepared as explained in section 2.1 and then transferred to the preheated sample holder of the NMR. The probe and rotor of the machine have been preheated at 90 °C prior to experiments. The sample was cooled to 22 °C from 90 °C at the rate

of 0.5 K/min rate. The lowest possible cooling rate was selected to maintain the system at equilibrium as much as possible. After reaching 22 °C, the sample was kept for 24 h for understanding the crystallization kinetics. The automated program was set to take the spectra each after 15 minutes of the timeline. Each experiment was performed in triplicates, and for plotting in results and discussion chapters, the best two results out of three were considered.

SFC analysis: In order to calculate the SFC, the spectra were further analyzed. The liquid sample is detected as a sharp peak while the broad signal indicates the solid sample as shown in Figure 65. Hence for calculating the SFC, the following equation was used.

$$\boldsymbol{SFC}\ (\%) = \frac{\left(\boldsymbol{A_{fs} - A_{sp}}\right)}{\boldsymbol{A_{fs}}} * \mathbf{100} \qquad (\mathbf{2.7})$$

A_{sp} = Integrated area under the sharp peak

A_{fs} = Integrated area under the full spectrum

SFC for all the spectra was calculated by using MATLAB automated program.

To understand the crystallization kinetics in detail, the SFC vs. time data was analyzed using the Avrami model. This model is being used to measure crystallization kinetics along with an understanding of the nature of the crystal growth process [21]–[23]. In order to represent this model in terms of time dependent SFC in fat crystallization, equation 2.8 has developed

$$\frac{\boldsymbol{SFC(t) - SFC(0)}}{\boldsymbol{SFC(max)\ or\ SFC(\infty)\ -\ SFC(0)}} = \left(\mathbf{1} - \boldsymbol{e^{-kt^n}}\right) \qquad (\mathbf{2.8})$$

Where, $SFC(t)$ is the solid fat content at a particular time *t*; $SFC(max)$ is the maximum SFC achieved at a particular temperature or equilibrium solid fat content $SFC(\infty)$ and $SFC(0)$ is the SFC at time t=0 [11]. Ideally, $SFC(0)$ equals zero as no crystals are formed, however, in the current study at 22 °C already some amount of solids were detected hence, the eq. 2 was used as it is. The Avrami parameter (k) is a function of crystallization temperature and considers the relation of nucleation and crystal growth rates altogether. Whereas, the non-universal Avrami exponent (n) is a number of crystallization which focuses empirically on the crystal growth mechanism. This is a combination of the function of the time dependence of nucleation and the number of dimensions in which growth takes place.

2.9 Oscillatory rheology

Oscillatory Rheology: The cross-hatched parallel plate rheometer (Hybrid Discovery HR-3) was used to perform the experiment, which is shown in Figure 29 (a). To measure the viscoelastic properties using the rheometer, a 40 mm diameter plate was used. Before starting the measurement of the sample, the calibration was performed for 40 mm geometry within the temperature range of 90 °C to 22 °C by using TA Instruments TRIOS software to determine the thermal expansion of the plates due to heating. Afterwards, the temperature of the rheometer was set to 90 °C and the two plates were kept close to each other to ensure the homogeneous temperature in the sample, which was then covered with the thermal insulator as shown in Figure 29 (b). In the meantime, the blend was prepared as given in section 2.1 and before the sample was poured on the lower plate, the gap was again zeroed. The parameters used for the experiment are shown in Table 5. For measurements, axial force control (0 N) has been employed to ensure proper contact when the sample is shrinking due to a change in volume during the crystallization process. Also, the maximum torque limit was set to 100000 µN.m to avoid damage to the instrument in the case of a higher torque value.

Crystallization kinetics and fractal dimension: The effect of oscillation strain on crystallization kinetics of CB/CO blends and CB-CO blends with n-alkanes were studied by cooling the sample from 90 °C to 22°C with the cooling rate of 0.5 K/min and a strain of 0.001%. After reaching 22 °C, the time sweep was performed for 2 h and 30 minutes. This timeline was selected based on the primary results of crystallization kinetics under polarized light microscopy with the same procedure. At this timeline, the crystal growth of CB was showing a dense crystal network. Hence, after crystal network formation, the amplitude sweep was carried out in the range from strain 0.0001 to 100%, for understanding the breaking of the crystal network. From these data, the Linear Viscoelastic (LVE) and non-Linear Viscoelastic (NLVE) regimes were determined based on each different composition. Moreover, the fractal dimension was calculated based on the Kraus model theory (explained in chapter 1). In the case of the connectivity parameter, C is assumed to be 1.3: the cluster aggregation is supposed to be well percolated and therefore the value is assumed to be 1.3. The experiments were performed in triplicates. The evaluation of graphs was carried out in origin software.

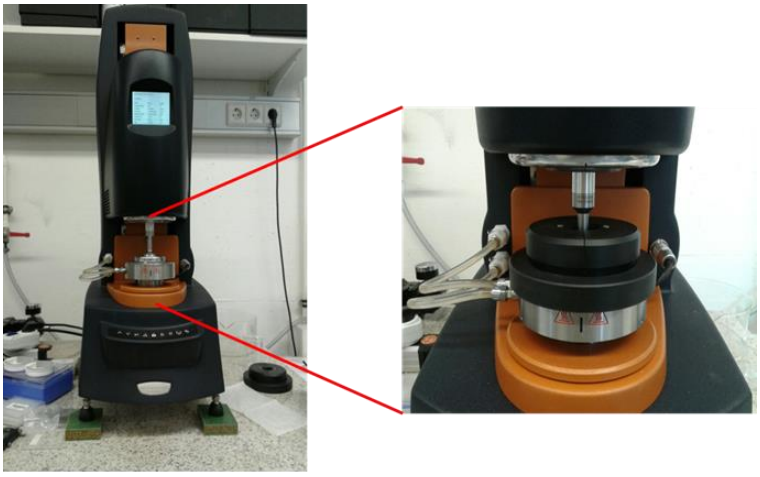

(a) (b)

Figure 29: (a) DHR-3 Rheometer; (b) Thermal insulator for controlling the temperature gradient.

Table 5: Experimental parameters for rheology

Parameters used for the experiment	Rheometer Values	Rhoe-microscopy Values
Start Temperature	90 °C	60 °C
End Temperature	22 °C	22 °C
Soak time at 90/60 °C	15 minutes	15 minutes
Cooling ramp	0.5 K/minute	0.5 K/minute
Strain (%)	0.001	0.001
Axial Force	0 N	0 N
Frequency	1 Hz	1 Hz
Torque	100000 µN.m	100000 µN.m
Gap	1000 µm	100µm
Geometry	Cross-hatched parallel plate 40mm ø	parallel plate 40mm ø

2.10 Rheo-microscopy

The Rheo-optics facility was used to observe the crystal network formation under the rheometer and to understand the effect of oscillation strain on the fat crystal network. To carry out the experiments, some modifications in parameters were considered as compared to usual rheometer settings. The gap between the two plates was taken 10% less than the usual cross-hatched plate assembly to observe the clear images of crystals. 0.001% was used as the oscillation strain rate. As the starting temperature 60 °C was used instead of 90 °C due to limitations of high temperature resistance of the microscope objectives. To protect the glass plate, the timeline for time sweep was differently chosen than for usual experiments according to the modulus value achieved. After reaching the plateau region, an amplitude sweep was carried out. The single video was captured during amplitude sweep in the form of 'multipage tiff' with 9 Hz frame rate. Captured videos showed the crystals at the upper layer, middle layer and lower layer at the bottom plate to visualize the 3D network connectivity of crystals. A 20x objective was used. The parameters used for carrying out experiments are shown in table 5.

After performing the experiments, the videos were analyzed using Image J software. This multipage tiff file was converted into Avi file with 14fps rate for a better view. In total 1712 frames were captured during amplitude sweep and the correct image was selected as per the increase in amplitude for plotting in the graphs in the result section.

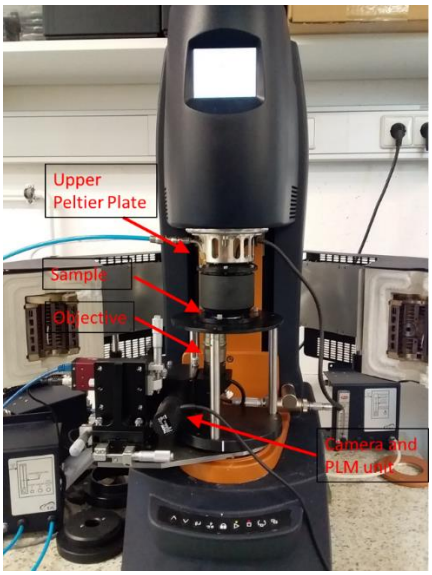

Figure 30: The assembly of in situ microscopy unit to the DHR-3 Rheometer.

Chapter 3: Results and Discussion

Section 1: Compositional analysis of CB and CO

The fatty acid analysis of CB and CO is shown in Table 6. The result depicts that CB consists of long-chain saturated FA ranging from C18:0-C24:0. The concentration of Stearic acid (C18:0), Arachidic acid (C20:0), Behenic acid (C22:0), and Lignoceric acid (C24:0) are significantly high as compared to other studies [71], [72]. As a result, this kind of CB could melt at a higher temperature. Thus, while preparing the samples, the temperature used was 90 °C to ensure complete melting. The concentration of Palmitic acid (25.32 wt%), Stearic acid (36.74 wt%), and Oleic acid (32.48 wt%) in CB are the highest with respect to other FAs present in CB, which is in agreement with other studies [73]–[75].

In contrast with CB, the concentration of (C18:0)-(C24:0) is very low in CO and it mainly consists of small and medium-chain FA ranging from (C8:0)-(C16:0), in which Lauric acid (42.78%) and Myristic acid (17.64%) are present in higher concentration. Although CO was found to contain a high amount of saturated fatty acids, Oleic acid (9.23%) and Linoleic acid (2.99%) are also detected in a significant amount. This mixture of short, medium, and long-chain fatty acids and their sn-position explains the different physical, thermal and mechanical properties of fats [8].

Table 6: Fatty acid composition of CB and CO

Fatty Acid	Cocoa Butter (weight %)	Coconut Oil (weight %)
Caproic acid (C 6:0)	-	0.72
Caprylic acid (C 8:0)	-	7.75
Capric acid (C 10:0)	-	5.64
Lauric acid (C 12:0)	-	42.78
Myristic acid (C 14:0)	0.09	17.64
Palmitic acid (C 16:0)	25.32	9.61
Palmitoleic acid (C 16:1ω7c)	0.24	-
Heptadecanoic acid (C 17:0)	0.21	-
Stearic acid (C 18:0)	36.74	2.87
Octadecenoic acid (C 18:1-trans)	0.02	-
Oleic acid (C 18:1ω9c)	32.48	9.23
Linoleic acid (C 18:2ω6c)	2.88	2.99
Octadecadienoic acid(C 18:2ω6-trans)	0.02	-
alpha Linolenic acid (C 18:3ω3c)	0.17	0.3
Arachidic acid (C 20:0)	1.09	0.1
cis-11-Eicosenoic acid (C 20:1ω9c)	-	0.09

Behenic acid (C 22:0)	0.18	-
Lignoceric acid (C 24:0)	0.1	-
Saturated fatty acids	63.73	87.11
Monounsaturated fatty acids	33.07	9.53
Polyunsaturated fatty acids	3.05	3.29
Trans fatty acids	0.04	< 0.01
omega-3 fatty acids	0.17	0.3
omega-6 fatty acids	2.88	2.99

The TAG composition of CB was determined by HPLC and is shown in table 7. (Eurofins Analytik GmbH, Hamburg, Germany). However, the TAG composition does not show the presence of Arachidic acid (C 20:0), Behenic acid (C 22:0), and Lignoceric acid (C 24:0) in terms of TAGs. Unfortunately, only ~95% of TAGs could be identified; therefore, it was difficult to conclude whether these long-chain fatty acids are in presence of TAG, diacylglycerol (DAG), monoacylglycerol (MAG), or in terms of free fatty acid. Thus, the mixtures of different TAG, DAG, MA, and FA in CB form a complex system with a complicated phase behavior by itself.

Table 7: TAG composition of CB

TAGs in CB	Conc. (wt%)	TAGs in CB	Conc. (wt%)
PPP	0.1	PLL	0.4
MOP	0.1	SSS	0.3
PPS	0.5	SOS	26.5
POP	16.7	OOS	2.2
PLP	1.8	OOO	0.2
PSS	0.6	SLO	0.3
POS	39.8	OLO	0.1
POO	1.7	SLL	0.2
PLS	3.4	LLO	<0.1
PLO	0.3	LLL	<0.1

P = Palmitic acid; M = Myristic acid; O = Oleic acid; S = Stearic acid; L = Linoleic acid.

Therefore, the thermal properties of fats and oils mainly depend on the composition of the individual fat and wt% in the mixture. For instance, blends of CB/canola oil and CB/soybean oil showed different characteristics as canola oil consists of mainly OOO, LOO, and OLnO, whereas, in soybean oil LLL, LLO and LOO are present (where O = Oleic acid; L = linoleic acid; Ln = Linolenic acid) [27].

Section 2: Mixing behavior of CB/TS blend

This chapter focuses on the effect of Tristearin (TS) addition to the crystallization of Cocoa Butter (CB). The effects are in terms of variations in thermal behavior, morphology, and interaction of CB and TS in their respective blends. As TS is a part of CB as well as the stearin part of other oils, for instance, palm stearin. It also can be used along with other fat in order to either replace or substitute CB in confectionery applications [76], [77]. However, palm stearin is rather composed of more than just stearin [77], hence, in this current study, pure TS is used to understand the interaction in detail.

2.1 Characterization of thermal properties of CB/TS blends by using DSC

Figure 31 shows DSC thermograms for three different segments of CB/TS mixtures. After storage of the sample at 22 °C for 24 hours, the melting thermogram (Figure 31 (a)) was performed for studying the effect of isothermal crystallization on blends. The thermogram of CB/TS shows a linear trend with respect to the change in concentration of fats. In the case of pure CB, two endothermic peaks occur during the melting process, which can be ascribed to the melting of two polymorphs, Form IV (30.85 °C) and Form V (33.6 °C) [35]. Similarly, in the case of pure TS, one endothermic peak at 46.8 °C (indicated by α melt arrow) and another at 61.7°C (P_{TS}) are observed. However, according to a study of Windbergs group [36], onset temperatures of 54 °C and 63 °C represent α and β' polymorphic forms. The difference in the melting temperature between this present research work and the Windbergs study might correspond to the difference in sample preparation technique.

For blends, after the addition of TS to pure CB, the peak shifts towards higher temperature, and the peak area increases accordingly as the concentration of TS increases. Another observation, in the pure TS curve, an exothermic peak is observed during melting (indicated with a red arrow in Figure 30(a)). This phenomenon occurs due to solid-liquid-solid (S-L-S) or melt-mediated transition in TS. Firstly, one crystal form is melted at 46.8 °C and recrystallized into another crystal form at 48 °C, which is melted immediately. Therefore, an observable S-L-S transition instead of S-S transition occurs.

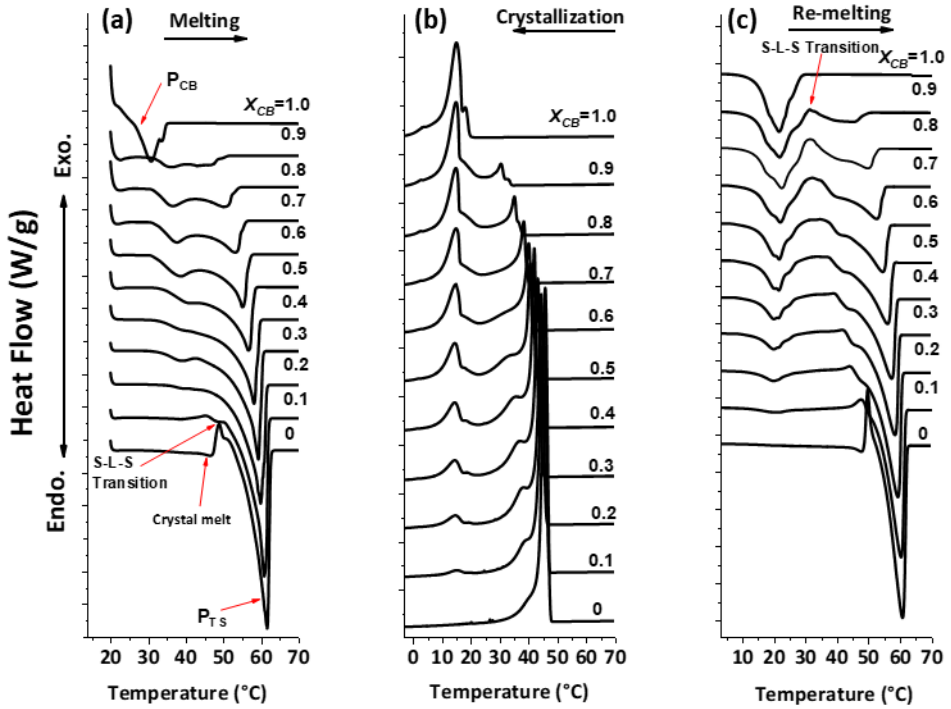

Figure 31: DSC analysis of CB/TS blends. (a) Melting process after crystallization for 24 h at 22°C. The arrows indicate the peak of CB (P_{CB}), the peak representing TS (P_{TS}) and α polymorph melting. (b) Dynamic crystallization from 90°C to -50°C. (c) Re-melting of crystals formed in segment (b). Arrow indicates the S-L-S (Solid-Liquid-Solid) Transition.

Similarly, using DSC and X-ray diffraction, the study of Lavigne and group proved the hypothesis that the phase transition from α to β in TS was of S-L-S type, as the β phase occurred from a melt of α not directly from solid α [78]. The S-S transformation from vertical α form to β' could be due to the collapse of hydrocarbon chains or from bending of each molecule in the glycerol region [12]. However, the physical reason for the appearance of an S-L-S transformation is still yet to understand.

The next segment (in Figure 31 (b)) was designed to observe the effect of dynamic crystallization on the individual fat and their respective blends. A controlled cooling process was achieved by this segment that led to the formation of different crystal forms from the isothermal crystallization for 24 hours. In Figure 31 (b), the crystallization exotherms for all samples are shown. Pure CB crystallizes according to the composition of TAGs present in the CB. The co-crystallization of the high melting fraction (HMF), a medium melting fraction (MMF), and a low melting fraction (LMF) takes place. Likewise, pure TS crystallizes into one crystal form having a higher melting point showing a sharp peak at 45 °C along with a shoulder peak of another polymorph. The blends produce two exothermic peaks, in which P_{TS} represents

TS and P_{CB} indicates CB. Furthermore, P_{TS} shifts towards lower temperature after the addition of CB, and the area of peak decreases accordingly. Whereas, for P_{CB}, only the peak area is decreased after the addition of TS, but not specific change in crystallization temperature of CB is observed.

For determination of ΔH value in crystallization and melting segments of CB/TS blends, P_{CB} peaks are taken as a reference peak as there was no specific peak shift. For the crystallization process, the range from 90 °C to 24 °C is considered for P_{TS} and below for CB, whereas, for the re-melting process the 1st endothermic peak area for CB, the exothermic peak for solid liquid-solid transition and 2nd endothermic peak for TS (refer Figure 66) is considered.

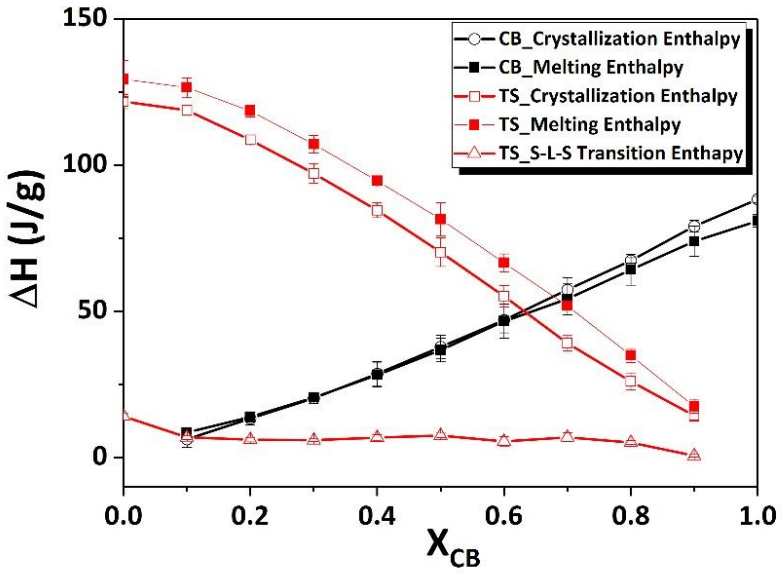

Figure 32: Enthalpy change of CB and TS during crystallization and re-melting process with respect to the weight fraction of CB. Black open square = crystallization, Black filled square = re-melting, Red open square = crystallization, Red filled square = re-melting, Open triangle = enthalpy change in S-L-S transition while re-melting.

The re-melting procedure was carried out for determining the melting profile of crystals that formed during the crystallization process (segment 2) with a heating rate of 2 K/minute. In Figure 31 (c), the melting endotherms detected by DSC are shown. Similarly, as in segment 2, P_{TS} represents the endotherm of TS and P_{CB} represents CB. In the case of pure CB, DSC detects one sharp peak along with shoulder peaks, which ascribes that a mixture of different melting fractions, are melted (from LMF to HMF). In the case of TS two melting fractions are formed, similarly, as of first melting (segment1 in Figure 31 (a)), expect that the peak temperature of higher melting fractions is slightly shifted from 61.4 °C to 60.97 °C

respectively. Hence, from the endotherms of all blends, the melting temperature (MT) of TS decreases after the addition of CB similar to segment 1. However, the exothermic peak (S-L-S transition) does not vanish completely even after the addition of CB. For evaluation of these endotherms, the temperature limit is selected as: below temperature 31.06 °C, the area is considered as CB and above temperature 33.4°C for TS. Figure 32 shows the crystallization, melting, and S-L-S transition enthalpy change against X_{CB}. ΔH for crystallization and melting exponentially decreases as CB increases whereas, for CB, both processes showed a linear decrease in enthalpy as the concentration of TS increases. In the case of the S-L-S transition from the re-melting method, the enthalpy change is almost constant throughout the composition of TS. This result indicates that ΔH for S-L-S transition is independent of the composition. How can this be understood? It is likely that there are always similar fractions of one certain crystal form (for instance Form I) which is forming during the crystallizing process. Since crystallization needs to be considered as a non-equilibrium process despite the slow cooling rates, it is attempted to provoke the stable polymorph during the heating process. Hence, the same energy is required in all blends for recrystallization. However, further investigations are essential to prove the hypothesis of the change in crystal domain size with respect to the temperature could provide the basis for similar recrystallization energy. This will be analyzed in further sections.

2.2 Pseudo-phase diagram of CB/TS system

The solid-liquid phase diagram for CB/TS is plotted by using DSC data from the re-melting segment with respect to x_{CB} in Figure 33 (a) and (b). In Figure 33 (a), the horizontal line (solidus line) achieved from the onset points (P_{CB}) and the monotonously increasing line (liquidus line) plotted from the melting profile of (P_{TS}) describes that two fats are completely immiscible with each other. This solid-liquid phase diagram exhibits a monotectic behavior [79] where a solidus line occurs as a horizontal and liquidus line increases from the melting temperatures of pure CB to pure TS. The phase diagram presents that below solidus line solids of TS (S_{TS}) and CB (S_{CB}) coexists. However, at $x_{CB} = 0$ the S_{TS} exists until the melting of α-form. Above the solidus line liquids of CB (L_{CB}) and S_{TS} coexist until the S-L-S transition line. At this transition line, the liquid transforms into solids of TS and then the melting of the sample starts. Hence, above this transition line, $L_{CB,}$ and partial liquid of TS along with solids of TS coexists. Above the liquidus line, both of the components are present in the liquid phase. A similar phase diagram was obtained in the case of POP/PPP mixtures [80]. According to the

authors of this study, phase diagram (POP/PPP) indicated that the interaction between monounsaturated (Sat-U-Sat) TAG and TAG of monosaturated fatty acid (PPP) could behave as a monotectic partial solid solution (as the difference in melting temperature of TAG component is more). Therefore, the results from the current study agree with the aforementioned study and it might be in case of CB and TS, the mixture behaves as a monotectic partial solid solution.

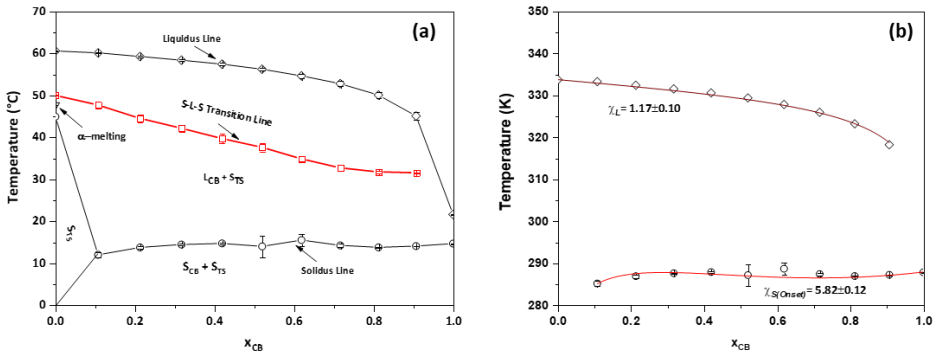

Figure 33: Pseudo phase diagrams of (a) CB/TS blends (b) represents the fitting of phase diagram by using Bragg-Williams approximation. CB/TS phase diagram depicts a monotectic mixture.

The thermodynamic analysis of the liquidus and solidus line is performed by assuming non-ideal mixing in both liquid and solid phases. Hence, Bragg-Williams approximation is considered instead of the Hildebrand model, which describes the ideal mixing behavior [61], [63]. In this study of the CB/TS phase diagram, component A represents TS, and component B: CB. The fitting of the Bragg-Williams approximation is shown in Figure 33 (b). Hence for fitting liquidus line data for CB/TS system, eq. 2.4 is used with the values of ΔH_{TS} = 118387.8 J/mol, T_{TS} = 333.76 K and R as 8.314 J/K.mol. Similarly for fitting the solidus line eq. 2.5 is considered with values of ΔH_{CB} = 66498.3 J/mol, T_{CB} = 294.79 K. For fitting the solidus line, onset temperature was considered. After fitting the experimental data, χ_L value is calculated as 1.17±0.10 KJ/mol (R^2>0.98) and $\chi_{s\ (onset)}$ as 5.82±0.12 KJ/mol (R^2>0.57) respectively. Although interaction parameters for solidus lines show similar results, this equation fits better to the onset data set compared to peak temperatures of CB. These high positive values indicate that the interaction of the energy of the CB-TS pair is more than an average of the CB-CB and TS-TS pair. This result suggests that steric repulsive interaction acts between CB-TS, hence the required energy is higher. Therefore, these results confirm that CB and TS are completely immiscible with each other in the solid phase. The possible reason for steric hindrance in CB-

TS could be due to the structural differences of TAGs in CB and TS. CB consists of mainly monounsaturated TAGs with oleic acid being the unsaturated part. Therefore, a double bond leads to the formation of defects in the TAG structure. Under crystallization, the presence of defects also can be called as kink, results in the loosely packed crystal formation. Whereas TS is a monosaturated fat with a similar chain length as CB TAGs. Therefore, after mixing these two fats together and due to the presence of the oleic acid in the CB structure, the chain packing becomes complex in nature. Thus, TS could have encountered difficulty in arranging themselves in a closely packed manner. Whereas, in the case of mixing two TAGs with at least one unsaturated fatty acid (in both of them), there could be fewer difficulties to pack themselves in a closer manner [17]. Hence, in the case of CB/TS blends, CB could act as an impurity and this might lead to a decrease in temperature of TS as the concentration of CB increased in it. Similar results are also obtained by the study of oleic acid and stearic acid mixtures, where the stearic acid temperature is decreasing after the addition of oleic acid, however, the temperature profile of two polymorphs (α and γ) of oleic acid's does not change [60].

2.3 Analyzing the effect of CB on change in the thermal behavior of TS

Based on thermal properties and thermodynamic analysis, the question remains, why do the crystallization and melting temperature of TS decrease as the concentration of CB increases. To understand in-depth what specific interactions causes such behavior in TS, Coherent Antistokes Raman Spectroscopy (CARS) and X-ray diffraction (XRD) techniques were used on three samples: pure CB, pure TS, pure deuterated TS (dTS), 50 wt% of CB, and TS (CB50+TS50) and (CB50+dTS50).

2.3.1 Asymmetry CH2 stretching as an indicator for solid-liquid phase transition in CB and TS

To detect the liquid-solid or solid-liquid transition in triglycerides, the relative intensity of CH_2 stretching modes (2700-3100 cm^{-1}) is considered [53]. While cooling, close packing of triglyceride molecules is obtained as a result of van der Waals forces. Due to the closely packed arrangements of the TAG molecule, electron clouds are also close to each other, which results in two vibrational states as CH_2 symmetric and asymmetric stretching modes. This perturbation

of two CH_2 stretches creates a Fermi resonance at ~2886 cm-1 [81]. In the solid-state, Fermi resonance is dominant due to tightly packed crystal lattice as well as prevailing lateral methylene interactions. Thus, Fermi resonance serves as an indicator of phase transition in complex natural lipid composition [82], [83].

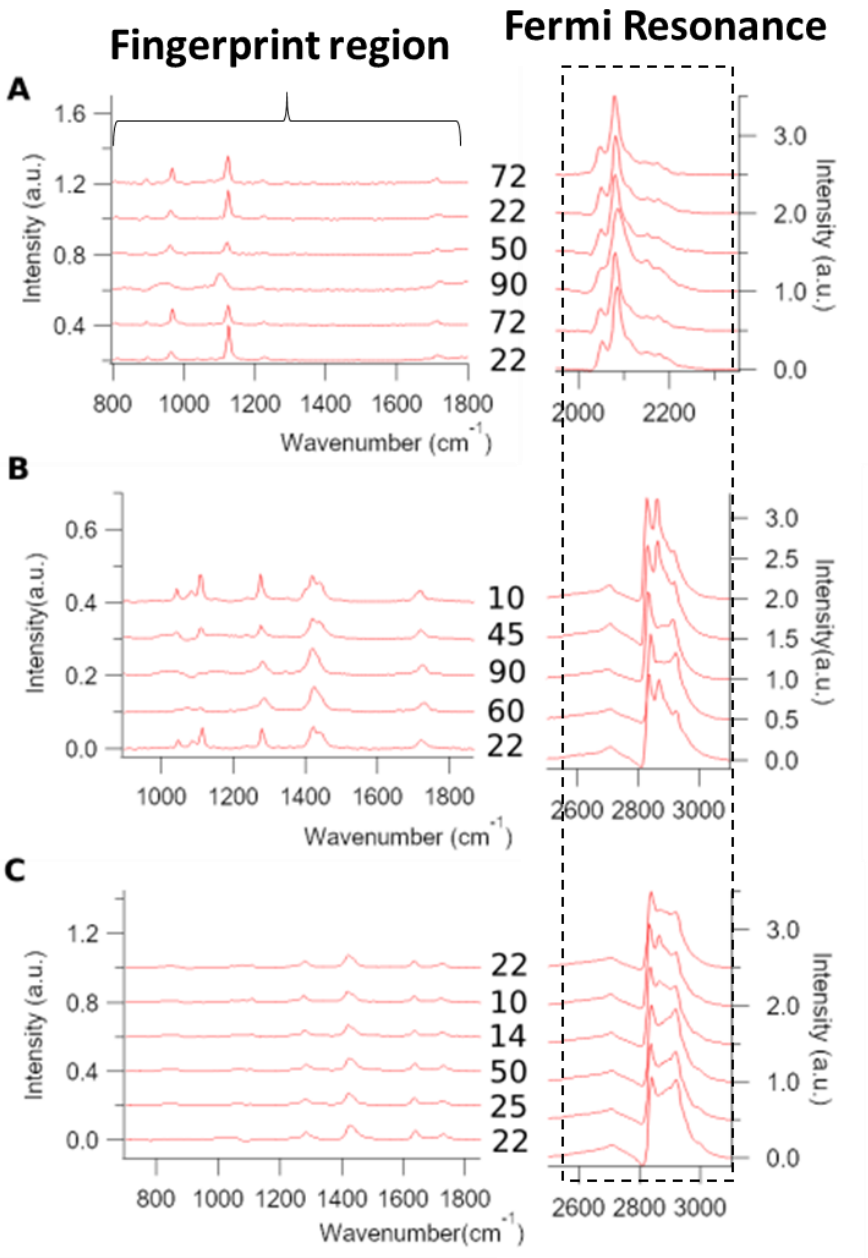

Figure 34: Spectral collection for a pure component. (A) Deuterated TS. The temperature ramp from 22 °C, 72 °C then 90 °C and cooled down to 50 °C then 22 °C, and heated up again to 72 °C. (B) Normal TS. The temperature ramps up from 22 °C, 60 °C to 90 °C and cooled down from 45 to 10 °C. (C) Normal CB. The temperature ramps up from 22 °C, 25 °C, and 50 °C, then cooled down to 14 °C and 10 °C and reheated to 22 °C.

In the current study, to understand the effect on lateral alkyl chain packing in CB/TS blends, initially, the experiments were performed on pure CB and TS. The change in peak shape is observed with respect to the temperature ramp. Similar to DSC experiments, the temperature segments were chosen. The results of pure TS and CB are shown in Figure 34 (B) and (C) respectively. The spectra collected for 1st melting segment at temperature 22 °C, 60 °C, and then 90 °C are shown in Figure 34 (B). The spectra of each temperature and for all samples are divided into two regions: fingerprint region (800-1800 cm^{-1}) and the region consist of CH_2 stretching mode (2700-3100 cm^{-1}) and Fermi resonance (2886 cm^{-1}). The fingerprint region focuses on the C-C stretching (1000-1200 cm^{-1}); the C-H region (1350-1500 cm^{-1}), which represents the rocking, scissoring, wagging, and bending deformation of the C-H functional group and the C=O stretching (1700-1780 cm^{-1}) [53], [84]. At 22 °C, all peak shapes represent the solid-state as compared with the previous study on characterization of three polymorphs and liquid state of Tristearin by Raman spectroscopy [85]. According to their study, with an increase in polymorph stability, the intensity of the C-C starching band decreases as the chains are packed more closely but the shape of the band does not differ with respect to the stability. This suggests that backbone alkyl chain properties are established upon solidification irrespective of the polymorph. Although, C-C stretching band shape does not change with respect to polymorphism, the effect on C-H and C=O stretching is noticeable. Similarly, in the case of the CH_2 stretching region, the effect of polymorphism and liquid state on peak shape can be easily noticeable. Therefore, in this study, as the temperature increases from 22 °C, the broadening of peaks in the fingerprint region and also vanishing of small peaks is observed. At the CH_2 stretching region (2800 cm^{-1} to 3000 cm^{-1}), the fermi peak at 2890 cm^{-1} is disappeared. As mentioned above, the tight packing of the solid phase of lipid-induced fermi resonance peak is disappeared while melting. During the 2nd segment, the sample cooled down at the rate of 2 K/min. The spectrum at 45 °C shows that CH deformation and bending modes reappear at ~ 1450 cm^{-1} similar to the first spectrum at 22 °C. With further cooling to 10 °C, C-C bending (~ 1070 cm^{-1}) and stretching (~ 1130 cm^{-1}) become more distinct than the spectra detected at the first melting segment (22 °C). This result depicts that, during the crystallization process of triglycerides the CH bending vibration occurs initially, which indicates the ordering of CH functional group from either alkyl chain and/or glycerol backbone occurs earlier than any other functional group. Therefore, with these observations, the melting and crystallization of lipids are to be detected by the disappearance of certain peaks for instance CH functional group.

Another observation is that melting and crystallization behavior under CARS setup is in agreement with DSC results, in which, melting temperature is ~ 60 °C and crystallization is ~ 45 °C, where, the mobility of CH is reduced as compared to the liquid.

Next, similar experiments with CB were carried out. In the fingerprint region of CB, similar functional group's vibrational bands are detected as in pure TS along with one new band is identified for C=C stretching (~1600-1700 cm^{-1}), which is also called as an olefinic band. Olefinic band position represents the skew-cis-skew' or skew-cis-trans conformation of the alkyl chain (as shown in Figure 35).

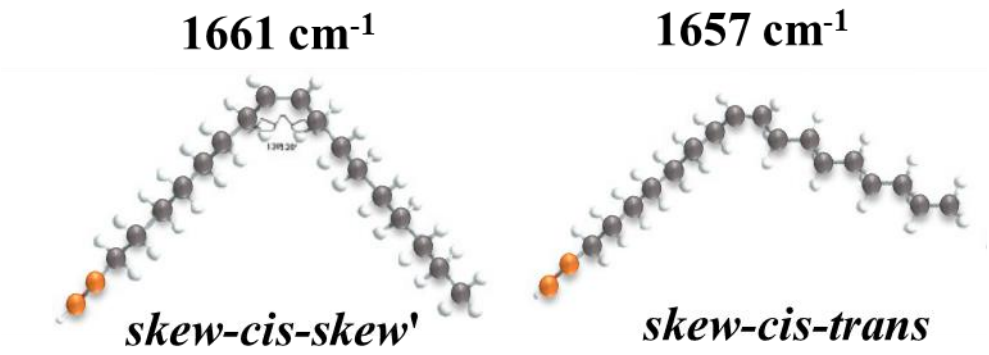

Figure 35: Skew-cis-skew' and skew-cis-trans conformation of alkyl chain with a double bond and their respective frequencies of Raman bands [86].

With respect to the stability of CB polymorphs, the intensity of C=C band decreases from liquid to Form IV as the interaction with surrounding inter or intra-molecular atoms reduced with molten TAGs to crystalline. But with increasing polymorph stability, the conformational changes occur from skew-cis-trans to skew-cis-skew' [86].

In this study, the temperature ramp was considered to understand the effect on different vibration modes of CB. As explained earlier, CB consists of defects due to the presence of a double bond, therefore, the melting temperature is less as compared to TS, which is also observed during CARS experiments. The spectra were collected at 1st melting segment at temperatures 22 °C, 25 °C, and 50 °C. The increase in temperature results in the broadening of peaks in fingerprint regions similar to TS. In the case of the C=C band, no specific change was observed with the melting of the sample. In the case of the C-H stretching region (3000-2700 cm^{-1}), no fermi resonance peak was achieved. Although at 22 °C, CB is supposed to be in a solid-state, the absence of a Fermi resonance peak could mean the sample could be in a molten state due to either laser power or handling of the sample. After heating the sample to 90 °C to

ensure complete melting, the sample was further cooled down to 14 °C as per DSC's peak temperature result. At 14 °C, a small peak of Fermi resonance was detected which indicates the liquid to the solid transition of CB. Further cooling to 10 °C results in a more pronounced peak. After reaching 10 °C, the sample was reheated again and the spectra collected at 22 °C indicates the disappearance of the Fermi resonance peak. This shows the melting of the sample, which is in agreement with the DSC result as the melting point of pure CB is ~21 °C. Therefore, similar results are obtained with CARS and DSC results in terms of thermal behavior.

As observed from these two pure systems, the fingerprint region as well as the fermi peak denotes the change in thermal behavior in the fat system, but, the CH bending or stretching occurs earlier while crystallization process as observed earlier, hence, the focus of the further study went on to the understanding of changes in the CH vibrational mode. However, both fats contain similar functional groups hence, in the case of blends, the effect on changes in vibrational modes was hardly detectable, hence, deuterated TS (dTS) was considered instead of normal TS for a deep understanding. All the hydrogen atoms in normal TS are replaced by deuterated form.

Initially, similar to pure components, the spectra for pure dTS were collected. In Figure 34 (A), the spectra for the 1st, 2^{nd,} and 3rd segments are shown. C-D stretching peak is detected in the region of 2300-1900 cm^{-1}, which is separated from CH stretching (3000-2700 cm^{-1}). In the case of the 1st melting segment, the spectra at 22 °C, 72 °C, and 90 °C show, a broadening of peaks in both fingerprint and C-D stretching region, this denotes, melting of dTS. Moreover, the peak shift is observed in the case of C-D vibrational mode at 90 °C. After heating to 90 °C, the sample is cooled to 50 °C, the sharpening of peaks is visualized, and this represents liquid to solid transition. Further, the decrease in temperature results in more pronounced peaks. Thus, overall, the thermal profile of dTS is in accordance with normal TS, except for the melting temperature. dTS is highly pure as compared to normal TS, hence, melts at ~72 °C instead of ~61 °C (Melting temperature of normal TS), which is in agreement with DSC results (Figure 67).

2.3.2 Merged images of CB/TS blend showed the phase separation after cooling

After understanding the effect of temperature ramps on pure samples, CARS hyperspectral images of the CB/TS blend sample are analyzed to understand the heat absorbance behavior in DSC. In Figure 36A, the overlay of CB and dTS regions from the 50/50 wt% blend is shown

along with the spectral view of the CH and CD region. For simplification and better understanding, the microscopic images are color-coded in red and green for dTS and CB respectively. Therefore, yellowish color in the images means both fats are well mixed, and red and green in the images mean pure species, in this case, phase separate. In Figure 36B, the effect on spectra and its corresponding microscopic images with respect to the temperature segments are shown. The image of the first melting segment at 22 °C (M1-22) depicts a perfectly mixed-phase as the yellow color is observed. According to the spectra, the CH fermi resonance around 2890 cm-1 is strong, which means CB and TS, both are in a solid phase. As the heating continues, in the M1-45 image, the yellowish color is still visible with the distinction of more reddish and greenish colors. However, the difference in spectra is observed as the CH Fermi resonance is demerging but not completely. Moreover, the peaks at 2950 cm-1 are still lower than the 2890 cm-1, which is similar to the pure CB spectra from C1-14, M2-22 (Figure 34C). This indicates CB is in the liquid-solid or solid-liquid transition respectively. Further increase in temperature up to 90 °C, results in complete melting of the sample.

Similar to DSC temperature ramps after reaching 90 °C, the sample was cooled to room temperature (~22 °C) by switching off the heating power. The total process needed about 20-30 min, and the temperature on the stage dropped nonlinearly. More specifically, it was fast from 90 °C to 45 °C but slow from 45 °C till 22 °C. It is remarkable, that, the phase separation can be observed clearly during the cooling process. According to the image (c1-22), the green parts are surrounded by the red region, which indicates, the CB crystals are surrounded by TS. The reason for having such a phase separation pattern is as follows. TS has a higher melting point, around 50 °C, when the temperature is dropped, the local TS crystalizes together and excludes CB, and CB forms around the round crystal blob of TS. The reasons are as follows. Firstly, there is no total exclusion of two triglycerides. Judging from the spectra, both species are coexisting although concentrations are low. When two triglycerides are mixed, the melting point is roughly equal to its proportional point. In the red blobs, the crystallization temperature is lower than the pure TS. On the other hand, in the green rims, the crystallization temperature is higher than that of pure CB. Secondly, in the spectra, the FR peak is existing in the green rims, where it indicates the high-density packing due to crystallization. Thus, this result is in accordance with the thermal data, where at 22 °C, no more heat absorbance is detected (Fig. 31).

Moreover, at C1-10, the spectra were not as good as the others, and a few factors affected them. The triglycerides were not formed equally crystallizing so that the coverslips were not completely flat, and that affected strongly on the background subtraction procedure

of the CARS spectra, due to the change of the refractive angle of the glass, which shifted the reference glass spectrum again. Besides, the cooler temperature at RT, especially at 10 °C, condensed small waters on the glass surface slowly through the scanning. With slight water condensation, the signals were also distorted. However, the signal was good enough to show the difference between CD and CH, and the separation was generally the same as C1-22.

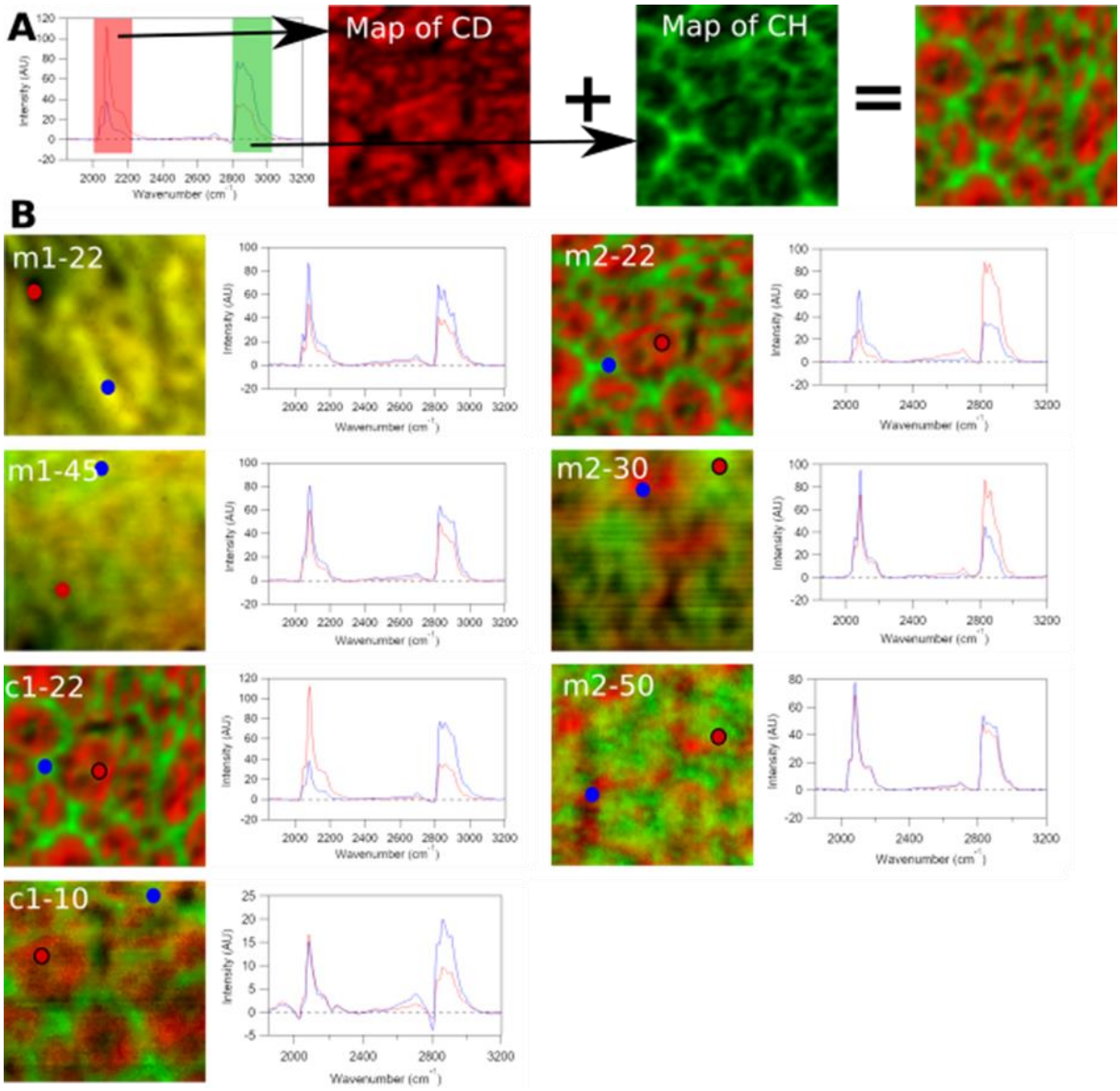

Figure 36: The overlay of cocoa butter (CH) and deuterated tristearin (CD) in temperature ramping. (A) A spectrum was taken from the CARS hyperimage. CD region was at 2000 - 2200 cm-1 and CH at 2800 - 3000 cm-1. By integration of two regions, two images were obtained. Then, using the ImageJ merge function, an overlaid image was created. (B) The mixture of

dTS50/CB50 temperature ramping cycle. The ramping cycle started from 22 °C, 45 °C to 90 °C and cooled to 22 °C and 10 °C then reheated to 22 °C, 30 °C, and 50 °C. At 56 °C, the mixture didn't melt, but when laser applied, the mixture melted and only melted at the focus, so that spectra cannot be obtained.

When reheated in the M2 cycle, the spectra became clear again, similar to C1-22. FR peaks are still visible in the green rims. As the temperature raised to 30 °C, interestingly, part of the green rims were mobilized and started to invade the red blobs. A new mixture is formed, and judging from the spectra, two species started to mix, although only part of the TS and CB mixture are mobilized. At 50 °C, most of the triglycerides are mixed well even more than 30 °C, where CH and CD are mostly at the same intensity. With further heating, the measurement at 56 °C was not able to detect the precise result as TS was melted due to the high power of laser on the sample, hence, a map at 56 °C was not able to present here.

Thus, with respect to all temperature ramps, and their corresponding effect on CARS, the microscopic and spectral results reveal that the distinct phase separation occurs during crystallization and melting of CB/TS blends which is in accordance with the thermal behavior, however, the question regarding the decrease in crystallization and melting temperature of TS after mixing with CB is yet to be answered. Hence, the XRD method was used to answer this question.

2.3.3 The correlation of lamella spacings with the change in the thermal behavior of TS

Based on CARS microscopy and spectral information one understood that there was a phase separation and hence, similar experiments were carried out by using XRD in order to understand the effect on lamella spacing with respect to the temperature and concentration of CB.

The first melting segment temperature ramp spectra for pure TS depicts that the crystal with lamella spacing of ~47 Å is formed after 24 h at 22 °C along with having only one small spacing (~4.12 Å). This is in agreement with the result depicted in previous work where the measurements for all the CB/TS blends after 24 h later at room temperature is measured (shown in Figure 37). These long and short spacings numerical values confirm that Form I (α form) polymorph is formed after 24 h at 22 °C [85]**,** which is in agreement with melting temperature. After the complete melting of a sample at 90 °C, it further cooled down to 0 °C with a 10 K/min rate without taking any spectral measurement. At 0 °C, the lamella spacing and short spacings

are calculated to ~48 Å and ~4.12 Å respectively. These spacing's numerical values represent the formation of Form I (α form) polymorph from the TS molecule [85]. In Figure 38 (A), the change in the peak position of the scattering vector with respect to the temperature for the re-melting segment for pure TS is shown. Each color represents the spectra at different temperatures. According to these graphs, as the temperature is increasing, the intensity of the peaks decreases until 40 °C, later at 45 °C, the peak shifts to a higher scattering vector, representing a decrease in lamella spacing, hence, providing a hint towards partial melting and followed by conformational changes. At 50 °C, the intensity again increases, which proposes that, recrystallization of molten portion to the new conformation. The further temperature rise resulted in reduced intensity, which suggests the melting of TS crystals. Similar to SAXS measurements, the change in the unit cell spacings is also observed with respect to the increase in temperature as shown in Figure 38 (B). At 0 °C, ~4.12 Å and with an increase in temperature the unit cell spacing increased (~4.14 Å), along with peak broadening effect. At 50 °C, four spectral peaks can be detected. This shift in peak position, the new formation of peaks, represents the change in conformation and hence, transformation to another polymorph. Thus, the effect on long and short spacings with respect to the temperature provides further support to the S-L-S transition phenomena, which is occurring in TS.

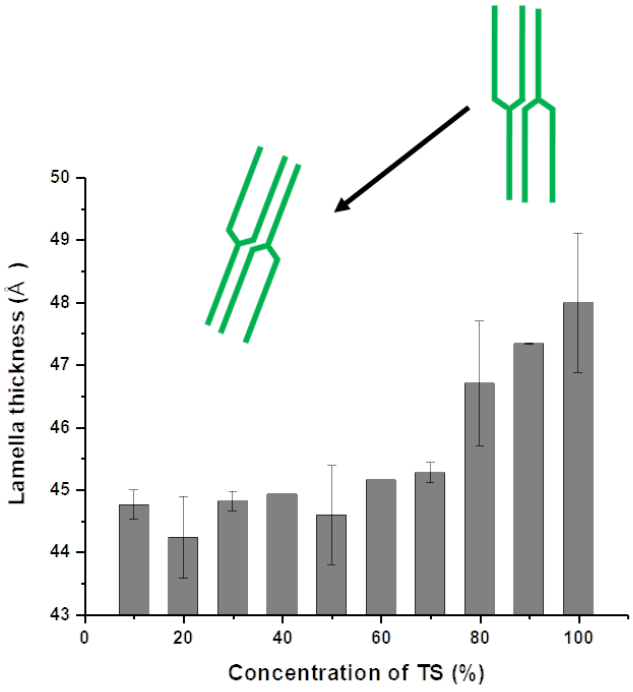

Figure 37: Effect on Lamella thickness with respect to the concentration of TS. 100% TS shows lamella thickness with hexagonal packing and in the blends, the lamella thickness decreased which represents either orthogonal or triclinic packing ability [87].

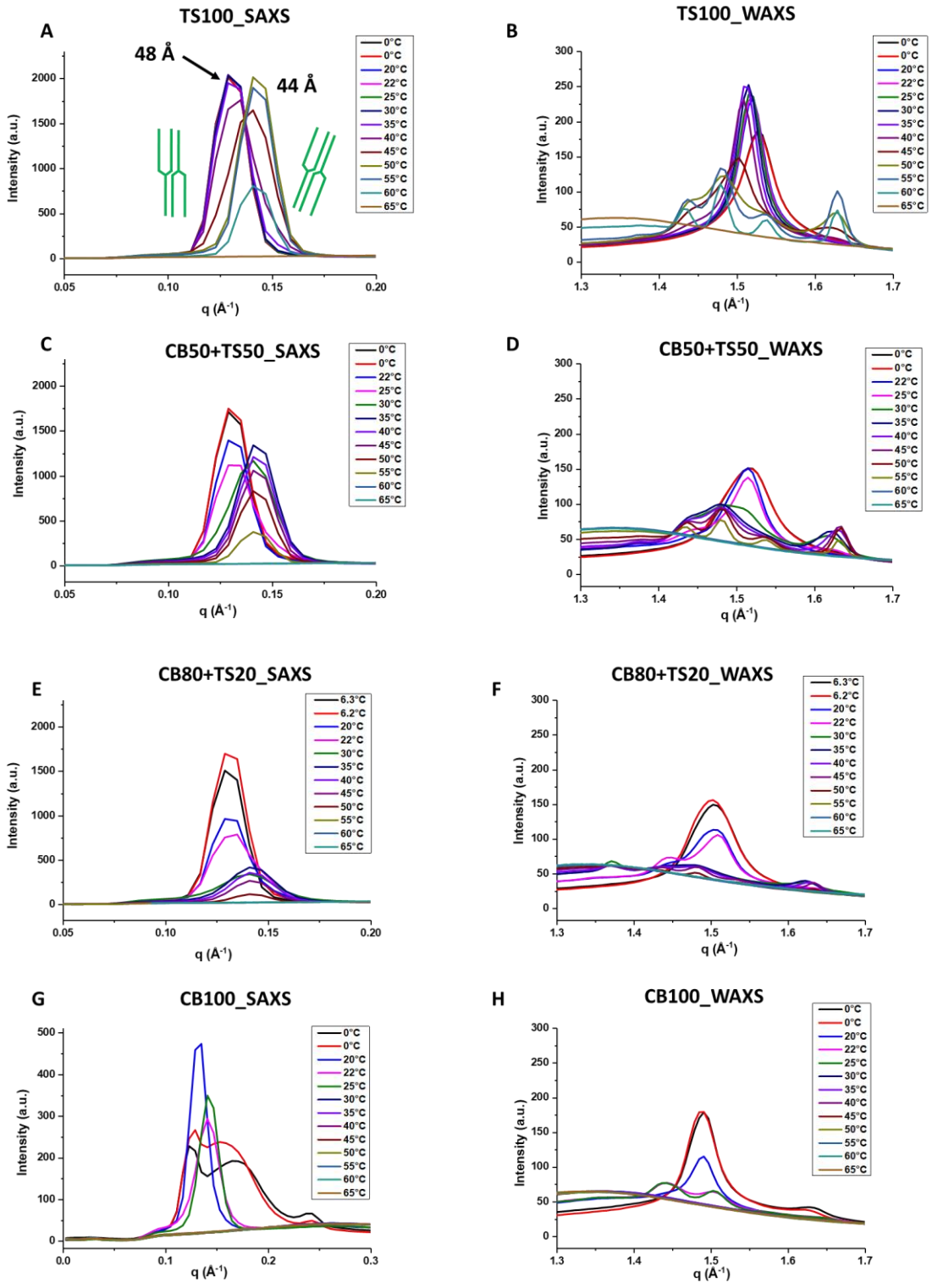

Figure 38: The re-melting segment start from 0 °C with a 10 K/min rate, each spectra capture time is 450 seconds, hence a large heating rate was considered. SAXS and WAXS spectra for A) & B) Pure TS; C) & D) CB50TS50; E) & F) CB80TS20 and G) & H) pure CB respectively. The peak shift with respect to the temperature is observed which helped to calculate and understand

the effect of temperature on lamella thickness and unit cell spacings. These are the intensity (I) vs. scattering vector (q) graphs.

In the case of the effect of CB on TS, two blends with 50 and 80 wt. % of CB is studied likewise. Similar to pure TS, after 24 h, the spectra shows, long spacing at ~44 Å, with broad spectra and reduced intensity. These observations suggest, either formation of more than one polymorph due to broadening effect or defects in crystal domain size due to the presence of CB crystals in it. As the temperature increased, the intensity reduced, which implies that the melting of crystals occurs. After reaching 90 °C, the sample was melted completely and then cooled down to 0 °C. (In case of blend with 80 wt. % CB, the liquid nitrogen was emptied and hence, the temperature could not reach 0 °C, therefore, spectra were detected at 6.3 °C instead of 0 °C). In the case of both blends, the SAXS measurements depict that, at 0 °C, the long spacing is ~48 Å, and as the heating proceeds, the shifts in peak position are detected. Similarly, according to the WAXS measurements, the broadening of peaks and the formation of new peaks with respect to the temperature are observed.

Table 8: The lamella spacing and unit cell spacing are calculated from XRD spectra for four samples and their corresponding subcell packing is depicted after comparing with the literature data.

Sample Name	1st Heating (22°C)			Remelting segment (0°C)		
	Lamella Spacing (Å)	Unit cell spacing (Å)	Subcell Packing	Lamella Spacing (Å)	Unit cell spacing (Å)	Subcell Packing
TS100	47 (α, 2L)	4.12	Hexagonal	48.25 (α, 2L)	4.12	Hexagonal
CB50TS50	44.14 (2L)	4.24;3.88	orthorhombic or triclinic	48.11 (α, 2L)	4.15	Hexagonal
CB80TS20	43.87 (2L)	4.92;4.34;4.18;3.91	orthorhombic or triclinic	48.13(α, 2L)	4.19; 4.31	Hexagonal
CB100	62.48; 31.8 (Form 5 3L); 43.82 (Form 4, 2L);	4.60; 3.93 (form 5 3L); 4.31; 4.17 (form 4 2L)	orthorhombic or triclinic	50.80 (form I, 2L);38.17;25.86	4.62; 3.94; 4.22 (form I)	Hexagonal and mixed crystals

In Table 8, the lamella spacing and unit cell spacing for four samples at 22 °C after 24 h and before the re-melting segment at 0 °C is shown. According to this data, and comparison with a study which indicated the long and short spacings for different polymorphs of TS and CB [35], [53], [85], TS forms a 2L chain length arrangement having hexagonal packing after 24 h at 22 °C, whereas, pure CB forms mixed crystals with 3L and 2L chain length arrangement having orthorhombic or triclinic subcell packing. This result is in agreement with the DSC thermograms after 24 h at 22 °C, as the melting temperature corresponds to the formation of α

form in the case of TS and form 4 and 5 in the case of pure CB. For re-melting segment at 0°C, the lamella spacing and unit cell packing indicate that 2L chain length arrangement having hexagonal subcell packing is formed for pure TS, whereas, CB forms mixed crystals with hexagonal packing, hence, there are three peaks are detected in the spectra as shown in Figure 38 G. As the temperature increases to 20 °C, only one peak with ~50 Å is observed. Further, the increase in temperature shifts the peak to lower spacings. This shift in peak with respect to the temperature suggests that, at 0°C, a mixture of different polymorphs with 2L chain lengths are formed, and as the temperature increases, the melting of the least stable forms occurs. Next, in the case of blends, at 22 °C and 0 °C, the crystals with 2L chain length arrangement with orthogonal or triclinic and hexagonal subcell structures are formed respectively.

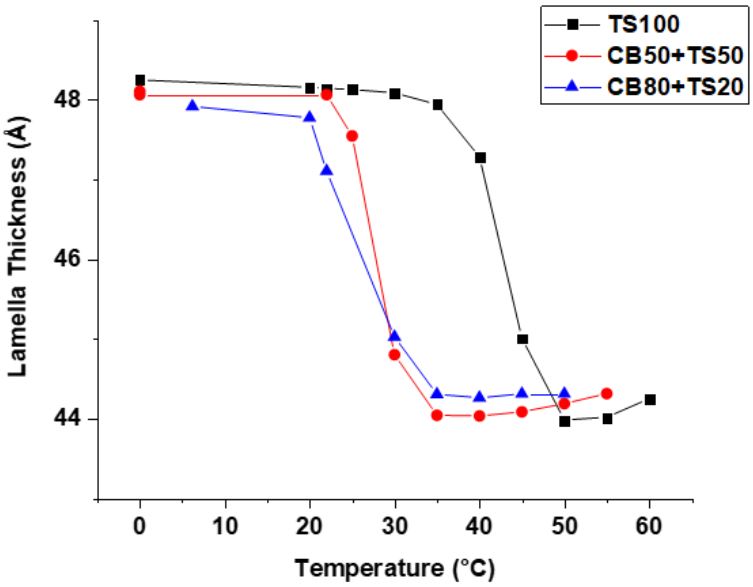

Figure 39: The re-melting segment start from 0 °C with 10 K/min rate, each spectra capture time is 450 seconds, hence large heating rate was considered. SAXS and WAXS spectra for A) & B) Pure TS; C) & D) CB50TS50; E) & F) CB80TS20 and G) & H) pure CB respectively.

To further get a deep insight into understanding the effect of concentration of CB on TS, the lamella spacing vs. temperature is plotted in Figure 39. According to this plot, the decrease of lamellar spacing from ~48 Å to 44 Å occurs in the temperature range of 35 to 50 °C for pure TS. Whereas, in the case of 50 and 80 wt% of CB, the decrease in lamella spacing was observed from temperatures 22 to 35 °C and 20 to 35 °C. This result reveals that the S-L-S transition of TS in blends occurs earlier than pure TS. Similar results were achieved in the

synchrotron radiation study on the phase behavior of triplamitate and sn-1,3-dipalmotoyl-2-oleoglycerol (PPP-POP). In this study, the melt-mediated transformation of PPP is promoted due to the presence of POP in the mixture. Due to the kinetic effect, the solubility of POP in PPP is different between α and β hence also provides monotectic phase behavior between POP and PPP [88].

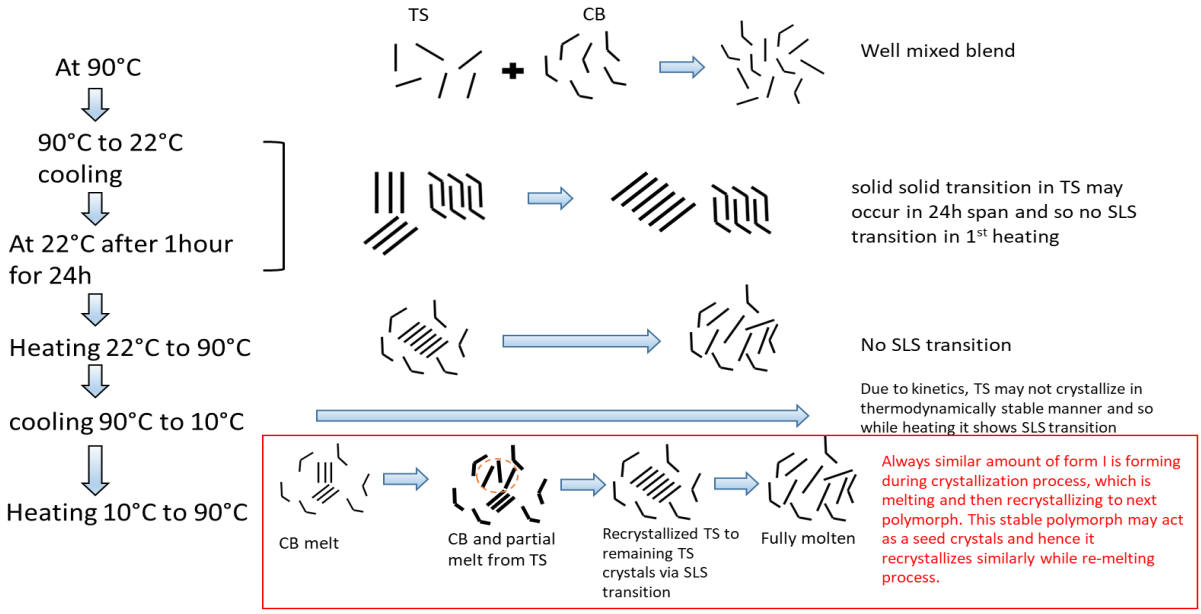

Figure 40: The schematic showing the changes at a molecular level with respect to the kinetics in the case of CB50+TS50 blend.

To explain further in detail the interaction between CB and TS and its effect on thermal properties of blends, the schematic corresponding to the segments has been drawn in Figure 40. This schematic shows the effect on 50 wt% of CB and TS. The sample is melted and mixed using an oil bath at 90 °C, hence, the very well mixed blend is prepared. Immediately, the sample is placed at 22 °C for 24 h to crystallize. During this 24 h timeline, TS immediately crystallizes with one crystal form (α) as a result of the high supercooling effect. However, the CB crystals crystallize relatively slowly, hence, within this duration, and availability of enough space for conformation changes, the TS crystals arrange themselves in a thermodynamically more stable form than the initial less stable form. Thus, during the first melting segment, the S-L-S transition of CB/TS blends are not detected during DSC, CARS, and XRD measurements, whereas, in the case of pure TS, the S-L-S transition is detected during DSC measurement. In the next segment, the molten sample is crystallized again with 2 or 10 K/min rate, therefore, very fast kinetics provide a crystallization of TS crystals first (α form), and the remaining sample which contains CB, crystallizes later, hence, the phase separation during

crystallization is observed. Thus, due to quenching, the conformation changes of TS crystals are not able to take place as similar to the isothermal crystallization segment (24 h at 22 °C). Immediately, after reaching a lower temperature (-50 °C or 10 °C or 0 ° C), the re-melting segment starts, CB crystals melts at ~21 °C, hence, due to the availability of enough space, the conformational changes occur relatively fast as compared to pure TS. Whereas, in the case of pure TS, as the temperature increases, α form melts and transforms into a stable form, whereas in the case of blends. Further, an increase in temperature results in the complete melting of the sample.

Hence, to summarize, due to the presence of CB, the defects in the crystal domain size ascribed to oleic acid conformation tend to provoke the S-L-S transition in TS crystals and thus results in quick melting of TS as the concentration of CB increases. As a result, there is no effect on CB crystallization and melting behavior but TS crystallization and melting temperature decreases.

Moreover, the crystal domain size was also calculated by using Scherrer equation (eq. 2.6) in order to understand the question of why similar enthalpy change for S-L-S transition (from DSC results) is obtained in case of CB/TS blends, however, no significant trend is to be found with respect to the different concentration due to lack of facility. As explained earlier, each measurement required ~6 minutes to complete, therefore, within this timeline, information regarding the quick process as a change in crystal domain size, thus, synchrotron XRD measurements for precise determination is required.

2.4 Morphological studies of CB/TS

The crystal morphology of CB/TS blends has been captured by PLM. Figure 41 shows the crystal morphology of pure CB and TS after 24 h at 22 °C and after heating this sample to 90 °C and cooled down to 10 °C with a 2 K/minute rate.

The pictures captured after 24 h at 22 °C, show the crystal formation after the isothermal crystallization process. Hence one can understand the morphology of crystals, which are melted during the DSC melting segment (Figure 31 (a)). According to DSC and XRD results, for pure CB, the mixture of Form IV (β_1') and Form V (β_2) are formed after 24 h at 22 °C, hence the visualization of these polymorphs can be viewed in Figure 41. The morphology can be described as a high number of small size crystallites along with some spherulites having a

needle-like structure at the periphery. In the case of pure TS, a spherulitic crystal network was formed.

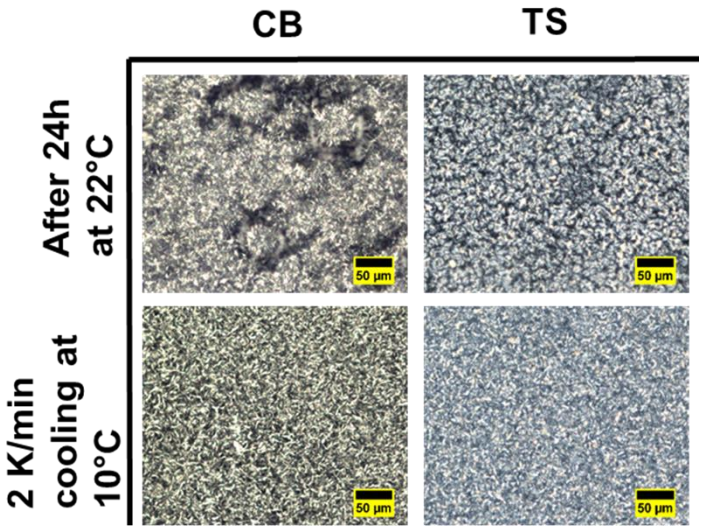

Figure 41: PLM analysis of pure fats after isothermal crystallization at 22 °C for 24 h and dynamic crystallization at 10 °C by cooling with 2 K/minute rate.

After heating at 90 °C and cooling down to 10 °C, the formation of crystal morphology shows the visualization of the crystallization process from DSC (Figure 31 (b)). In Figure 41, for all pure components, the crystal size changed to smaller and denser as compared to isothermal crystallization. In the case of pure CB, the crystals are the aggregation of small needles, and pure TS showed very small grainy structures.

Furthermore, the effect of the addition of different fats on the crystal morphology of pure CB was further studied. Figure 42 (a) shows the changes in crystal morphology after the addition of TS in CB for isothermal and dynamic crystallization. For X_{CB} of 0.90 and 0.80, at 22 °C after 24 h, spherulites consisting of needles are observed. For further compositions, the size of the spherulitic aggregates of needles is decreased as the concentration of TS increased.

For dynamic crystallization, after the addition of TS in CB, crystal size reduced and formed the grainy structure for the composition of 0.90 and 0.80. From 0.70 to 0.30 of CB, the mixture of small spherulitic crystal structure and the grainy structure is observed. Again, for further composition, smaller crystals are formed as the concentration of TS increased.

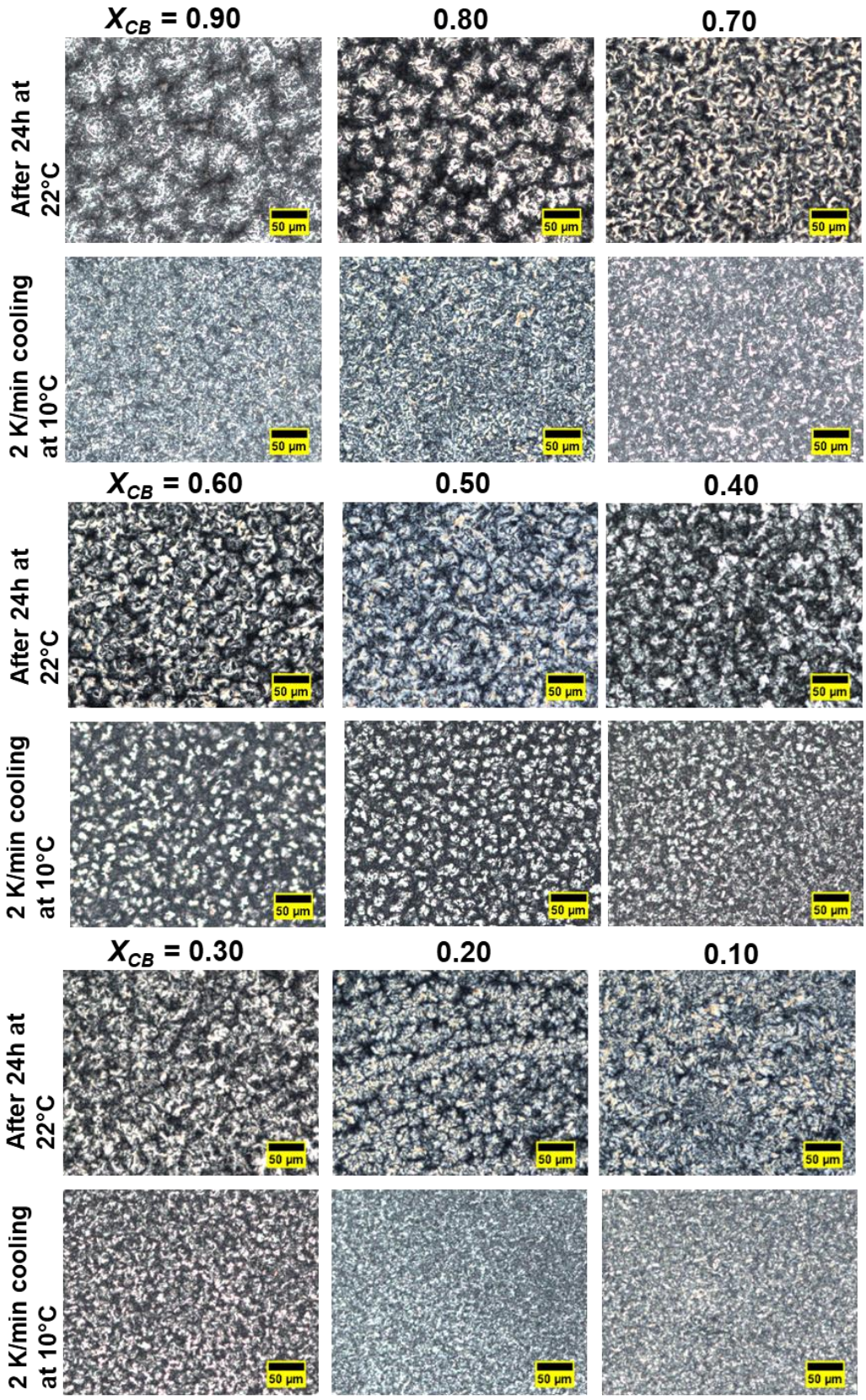

Figure 42: PLM analysis of CB/TS blends after crystallizing isothermally at 22°C for 24 h and then heating the sample to 90 °C and cooled to 10 °C with 2 K/min rate for studying the effect of dynamic crystallization.

2.5 Summary of CB/TS phase behavior

This section focused on the mixing behavior in the CB/TS mixture in different phases based on the solid-liquid phase diagram. DSC results depicted that CB/TS mixtures are completely immiscible in the solid phase and well mixed in a liquid state. Similarly, the thermodynamic analysis of the phase diagram resulted that, the interaction for mixed pair in CB/TS is energetically much more unfavorable than CB-CB and TS-TS pair. Similarly, CARS measurements supported the phase separation in CB-TS blends. The possible arrangement of CB and TS molecules at solid-state is shown in Figure 43. Moreover, the decrease in crystallization and melting temperature of TS after the addition of CB was observed due to faster S-L-S transition.

Isothermal and dynamic crystallization processes altered the thermal properties and crystal morphology of CB/TS blends. From these results of the dynamic crystallization process, one can say that a decrease in melting temperature results in small granular crystal morphology of blends whereas in isothermal crystallization granular to spherulitic structures was formed that resulted in higher melting points. Thus one can conclude that the variations in thermal and morphological behavior of fat and oil (CB/TS) blends are highly dependent on: 1) crystallization kinetics 2) “defects” created in crystal structure arrangements due to the monounsaturated part of CB.

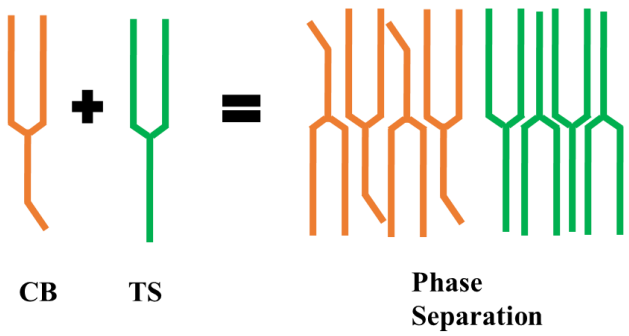

Figure 43: The schematic representing phase separation of CB and TS at solid state.

Section 3:Mixing Behaviour of CB/CO Blends

After studying the effect of the addition of pure fat (TS) on CB, the next study focuses on the mixing behavior of two bulk systems. This chapter emphasizes the effect of the addition of Coconut Oil (CO) on the crystallization of Cocoa Butter (CB). The study involves understanding the changes in thermal and morphological properties after the addition of CO, along with studying the effect on quiescent crystallization kinetics. Furthermore, the rheological properties are also derived. Based on these experimental analyses, the fractal dimension of the fat crystal network is calculated. Moreover, the effect on nanoscale arrangements of fat crystals is monitored and its relation to the macroscopic properties is derived.

3.1 Characterization of thermal properties of CB/CO blends by using DSC

Figure 44 (a), (b), and (c) shows the DSC results of melting after 24 h at 22 °C, crystallization, and re-melting thermograms of CB/CO blends. In the first segment of melting, only the samples with (weight fraction of CB) X_{CB} of 1.0, 0.90, and 0.80 show the melting from the crystals that are formed during 24 hours of crystallization (Figure 44 (a)). This behavior ascribes that CO is inhibiting the crystallization process of CB when added at more than 10 wt%. Likewise, the study [42] of crystallization behavior and kinetics of chocolate with lauric fat showed that at different temperature ranges, the solid fat content was decreasing after the addition of 10%, 20%, and 30% of CO, palm kernel oil and fractionated palm kernel oil. This decrease in solid fat content can be explained by the TAG composition in both the fats. CO contains a mixture of mixed and short-chained saturated TAGs, whereas, CB is a mixture of long-chain monounsaturated TAGs. Therefore, the packing ability is compromised between these fats together and so eventually, the compatibility is reduced.

In Figure 44(b), the results of crystallization are shown. P_{CB} represents the main peak for CB in all mixtures; P'_{CB} indicates the shoulder peaks, which were appearing after the addition of CO in CB. Similarly, P_{CO} and P'_{CO} denote the main peak for CO and the shoulder peak in the blends respectively.

As explained earlier in section 3, pure CB ($X_{CB} = 1$) crystallized in three fractions: HMF, MMF, and LMF. Likewise, for pure CO ($X_{CB} = 0$), two crystallization exotherms are detected, in which, one is a sharp peak at a lower temperature (2.5 °C) and the second peak overlaps with

the same peak at a higher temperature (7.4 °C). This could be because of incomplete crystallization of different TAGs in CO with a 2 K/minute cooling rate. If cooling rate is reduced, the complete crystallization of these short-chained mixed saturated TAGs may occur (CLaLa, LaLaLa, LaLaM, CCLa), as they are given sufficient time to arrange properly [89]. Further up to the mixture of X_{CB} = 0.50, two different fats could be identified, however, for X_{CB} = 0.40, the crystallization of all TAGs overlapped. Although it shows one main peak, there is still the existence of two shoulder peaks of HMF and LMF. For further blends, X_{CB} of 0.30, 0.20, and 0.10, the peaks are differentiated into P_{CO} for CO and P'_{CO} for shoulder peak, which appeared after the addition of CB.

Later, the melting profile of these mixtures was studied. Figure 44 (c) shows the endotherm results of all mixtures. Similar to crystallization, the shoulder peak is developed after the addition of CO in CB, however, the identification of these peaks is only possible up to X_{CB} = 0.70. For 0.60 and 0.50, the overlapping of melting peaks started to occur. For a mixture of X_{CB} = 0.40, endotherm has resulted in one main peak along with small shoulders. For X_{CB} of 0.20 and 0.10, P'_{CO} indicates the shoulder peak along with P_{CO} as a main peak in the mixtures. Hence from both crystallization and melting profiles, the mixture at X_{CB} = 0.40 can be described as the eutectic mixture, however, in the case of crystallization, the peak for this concentration is showing a broad profile instead of a sharp peak. Therefore, to determine the exact concentration profile for showing pronounced eutectic mixture and so the eutectic point, three more compositions were measured, namely as-X_{CB} = 0.34, 0.35, and 0.36.

In Figure 45 (a) and (b) the crystallization and melting profiles of the above-defined mixtures are shown. As the first melting process could not detect any thermogram because no crystallization occurs during 24 h, the 1st segment results are not shown here. The crystallization profile reveals that the shoulder peaks appeared on mixtures of X_{CB} = 0.40, 0.34, and 0.36 (pointed with an arrow and blue ellipse), whereas for X_{CB} = 0.35 mixture, no specific shoulder peak is detected. However, in the case of the re-melting segment, for the concentration of 0.40, 0.36, 0.35 the peak sharpness does not show any specific change. Another observation in both crystallization and melting is that the peak maxima are shifting towards higher temperatures as the concentration of CB is decreasing (shown by the dotted line). The eutectic mixture is when the mixture melts or solidifies homogeneously at one temperature, and this temperature is below the individual melting temperature.

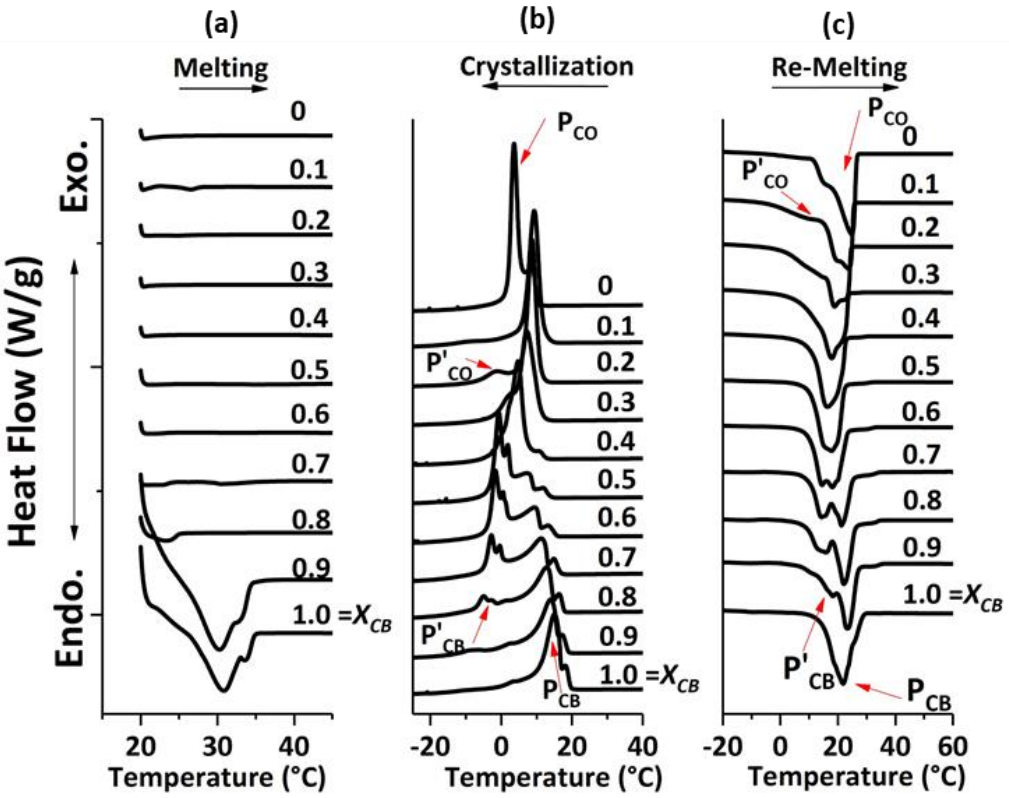

Figure 44: DSC analysis of CB/CO blends. (a) Melting process after crystallization for 24 h at 22 °C. (b) Dynamic crystallization from 90 °C to -50 °C. (c) Re-melting of crystals formed in segment (b). The arrows indicate the peak of CB (P_{CB}), the peak representing CO (P_{CO}), shoulder peaks appearing after the addition of CO in CB (P'_{CB}), and shoulder peaks appearing after the addition of CB in CO (P'_{CO}).

Therefore, the results of crystallization and melting together indicate that 0.35 of CB and 0.65 of CO represent a eutectic mixture, which melts at 16.7 °C. Unfortunately, it was not possible to detect a sharp peak in both the crystallization and melting process. The reason for such a behavior might be the mixture of different triacylglycerol in both fats, as pure Trilaurin (TL) from CO and POP from CB do not show any resemblance with the temperature profile of CB/CO blend (Refer Figure 68). Based on the thermal behavior of the addition of pure fats from CO and CB as TL and POP, the formation eutectic mixture could be possible when the system contains multicomponents such as mixtures of different TAGs. The compatibility between different mixtures of TAGs results in eutectic formation instead of the interaction between pure TAGs, which are present in a high amount.

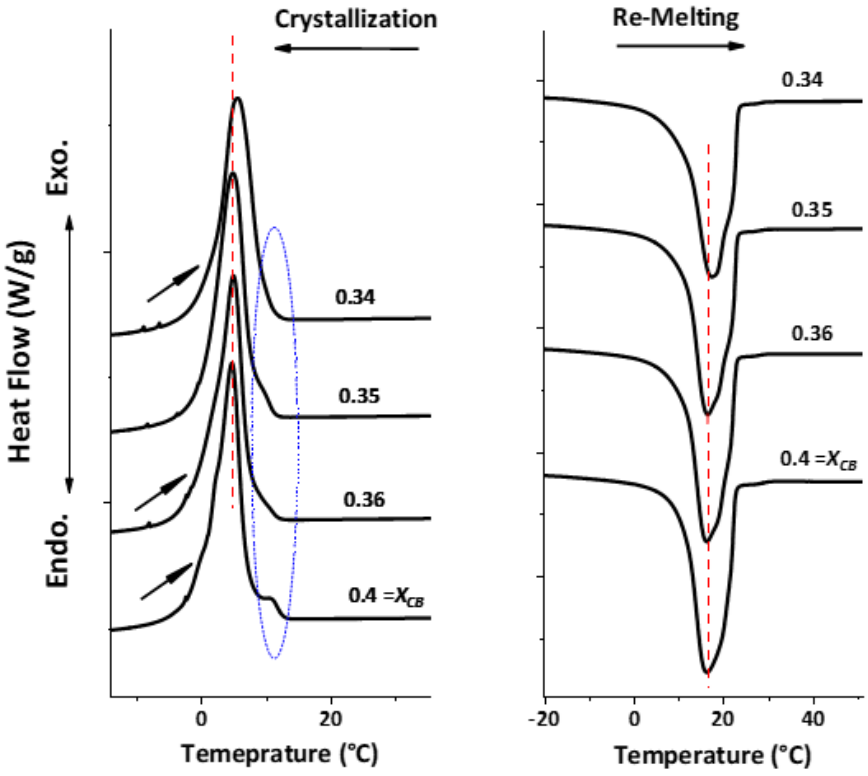

Figure 45: DSC analysis of CB/CO blends for determination of eutectic mixture. The samples were prepared similarly to other blends and the same process was used for DSC measurements. (a) Dynamic crystallization from 90°C to -50°C. (b) Re-melting of crystals formed in segment (a).

Analysis of all thermograms is plotted in Figure 46 (a) and (b) as enthalpy change, ΔH, with respect to X_{CB}. By using in built DSC instrument's STARe software the enthalpy change is calculated for P_{CB}, P'_{CB}, P_{CO}, $P'_{CO,}$ and one ΔH value for eutectic mixtures. The selection of region for CB and CO in CB/CO blends in order to calculate the area under the curve is shown in Figure 69 and Figure 70. ΔH value for P_{CB} is decreasing linearly for crystallization and exponentially for melting as the concentration of CB decreasing in both processes. Whereas, ΔH for P'_{CB} is increasing linearly and exponentially for crystallization and melting as the concentration of CB decreasing in the mixture respectively. Next, for the mixture of $X_{CB} = 0.40$ in crystallization, only one ΔH value is calculated as the addition of P_{CB} and P'_{CB}, similarly for melting process, $X_{CB} = 0.50$, 0.40 and 0.30 shows the broad peak hence one ΔH value is evaluated. In both processes, ΔH for P_{CO} is decreasing as the concentration of CO is decreasing, however, P'_{CO} is increasing as the concentration is decreasing in the mixture. From these

results, one can conclude that P'$_{CB}$ represents the CO phase in the blends and P'$_{CO}$ denotes the CB phase in the mixtures. Hence, from this hypothesis, one can say that there is phase separation in case CB and CO even if both of them have a similar melting temperature. Only the eutectic mixture shows the spatial homogeneity in two fats.

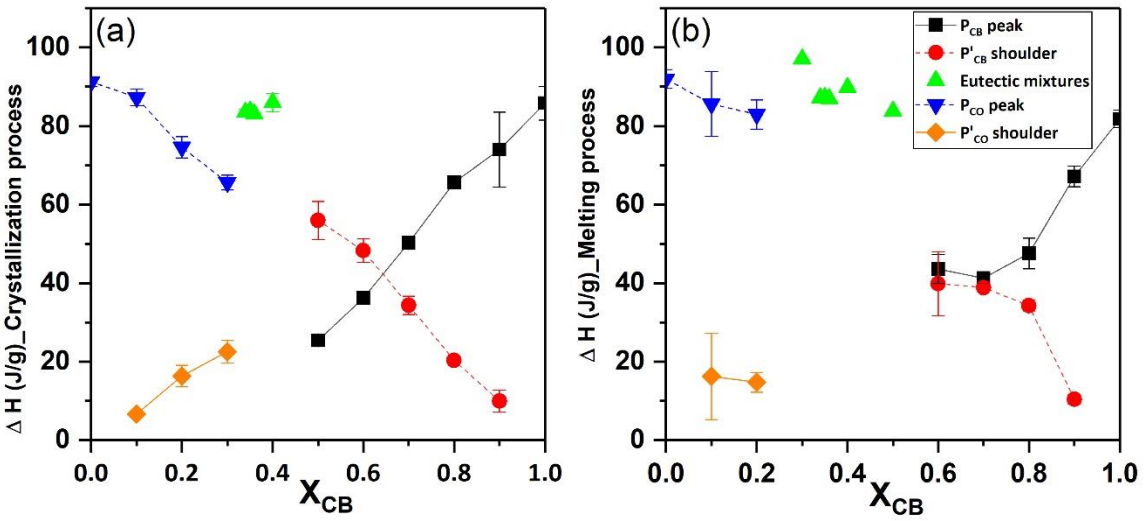

Figure 46: Enthalpy change of CB and CO during crystallization and re-melting process with respect to weight % of CB. Black closed square = P_{CB}, Red closed circle = P'_{CB}, Green closed triangles = Eutectic mixtures (X_{CB} = 0.40, 0.36, 0.35, 0.34), Blue closed reverse triangles = P_{CO}, Orange closed diamonds = P'_{CO}.

3.2 Pseudo-phase diagram of CB/CO system

Similar to CB/TS blends, the solid-liquid phase diagram for CB/CO is also plotted by using DSC data from the re-melting segment with respect to x_{CB} in Figure 47 (a). Liquidus line is constructed by considering peak temperature (P_{CB} and P_{CO} in Figure 44 (c) and Figure 45 (b)) in all blends and solidus line is achieved from onset temperature (blue triangles) and shoulder peak temperature (P'_{CB} and P'_{CO} in Figure 44 (c) and Figure 45 (b)). Up to solidus line, both components are in solid phases and above solidus line from composition, X_{CB} = 0.35 to 1, liquid of CO (L_{CO}) and solid of CB (S_{CB}) coexists, whereas, for composition range of X_{CB} = 0 to 0.35, liquid of CB (L_{CB}) and solid-state of CO (S_{CO}) coexist. Above the liquidus line, both components are in the liquid phase.

In the thermodynamic analysis of the pseudo phase diagram of CB/CO blends, Bragg-Williams approximation is considered instead of the Hildebrand model [61], [63], similar to

CB/TS blends. In this study of the CB/CO phase diagram, A denotes CB and B as CO. The fitting of the Bragg-Williams approximation is shown in Figure 47 (b). For fitting the liquidus line of the CB/CO phase diagram, Eq. (2.4) and (2.5) is used from the composition range of $x_E \leq x_{CB} \leq 1$ and $0 \leq x_{CB} \leq x_E$ respectively. Hence, the values of $\Delta H_{CB} = 66498.3\,\mathrm{J/mol}, T_{CB} = 294.785\,\mathrm{K}, \Delta H_{CO} = 57217.78\,\mathrm{J/mol}, T_{CO} = 297.815\,\mathrm{K}$ are considered from DSC results for fitting the experimental data. According to investigations of Abes et al. for binary mixtures of saturated fatty acids (SS/MM), the interaction parameter gives only one value for the whole composition range [61]. However, in the present studies, for composition range from 0 to 0.35 wt% of CB, the value of χ is -8.15±1.15 kJ/mol (R_2>0.54) and for other range is 3.8±0.47 kJ/mol (R_2>0.59). Due to differences in molecular structure and its volume, this approximation is not very well suited for CB/CO blends. From these values, it can be described that for CO and mixture with CB, the CB-CO pair is more compatible than the CB-CB pair and CO-CO pair in the liquid phase. For CB/CO blends of composition range from X_{CB} = 0.35 to 1, it is calculated the large positive value, this leads to the hypothesis that, CB-CO interaction energy is more and hence there is phase separation in the liquid phase. The reason for such behavior is their molecular structure. CB has monounsaturated TAGs, and because of oleic acid, the molecular length is reduced due to the kink of the double bond, and hence, the molecular length of CB and CO becomes similar to each other and thus leads to the CB-CO pair instead of like pairs. In case of further composition from eutectic to 1, an arrangement of CO having a mixture of short-chained (C12, C10, C8) saturated TAGs and CB as monounsaturated TAGs, could not pack densely due to the presence of a high percentage of CB which is not flexible even in the liquid state.

Although Bragg-Williams type approximations used in this current study for understanding the phenomenological interaction between CB/TS (in section 2) and CB/CO blends and the results obtained are in agreement with DSC results, it is still unclear how these interactions specifically take place in such complex fat/oil mixtures. A precise molecular interpretation is difficult since in the original Bragg-Williams approach the interaction parameters are defined by pseudopotentials between monomers only. In the mixtures of the fatty acids most of the monomers are identical, i.e., carbon-carbon bond and esterified glycerol bond. The main difference of the energy mismatch has its origin in the appearing cis-double bonds and the different chain lengths of the fatty acids. Both cause a large number of "defects" in the different polymorphs, which cause a major contribution to the energy balance. Hence,

the Bragg-Williams model can be considered in general only as a phenomenological model to describe the phase diagrams for fat blends.

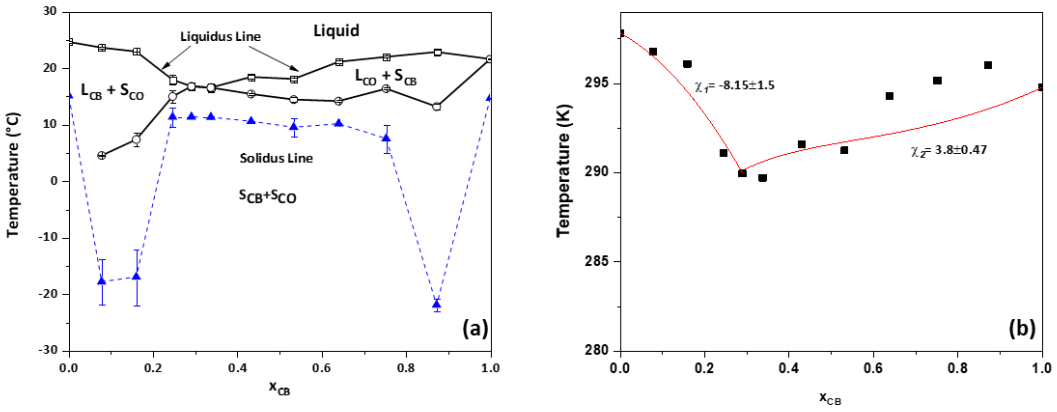

Figure 47: (a) The pseudo phase diagrams of CB/CO blends. CB/CO mixture shows eutectic mixture at X_{CB} = 0.35. (b) Represents the fitting of phase diagram by using Bragg- Williams approximation for CB/CO blends.

Nevertheless, the fitting results lead to the prediction that such interactions could occur due to either aliphatic chain packing of which several forms exist and/or differences in carbonyl group conformational changes [15]. Hence, precise pinpointing of interaction causing such behavior in both current systems is rather challenging. Additionally, according to current data, one can say that this approximation does not take into consideration various polymorphic states that exist in several other systems used in such studies and hence makes it rather difficult to comprehend interactions between distinct fat/oil blends.

3.3 Morphological studies of CB/CO system

The crystal morphology of CB/CO blends has been captured by PLM. Figure 48 shows the effect of the addition of CO on CB morphology after 24 h at 22 °C and after heating this sample to 90 °C and further cooled down to 10 °C with a 2 K/minute rate.

The pictures captured after 24 h at 22 °C, show the crystal formation after the isothermal crystallization process. Hence, one can understand the morphology of crystals, which were melted during the DSC melting segment (Figure 44 (a)). According to previous sections, for pure CB, the mixture of Form IV (β_1') and Form V (β_2) is formed after 24 h at 22 °C, hence the visualization of these polymorphs can be viewed in Figure 48.

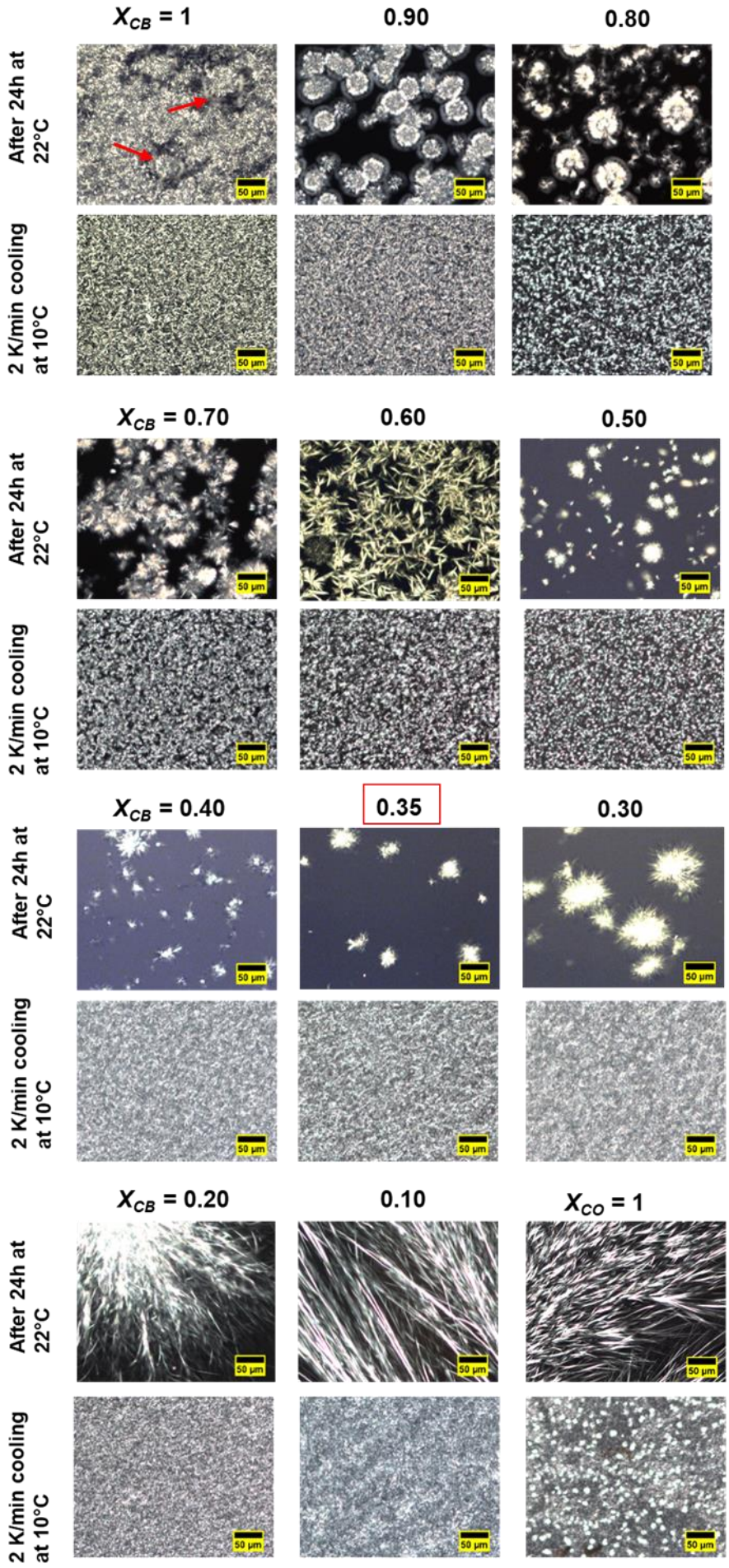
X_{CB} = 1
0.90
0.80
After 24h at 22°C
2 K/min cooling at 10°C
X_{CB} = 0.70
0.60
0.50
X_{CB} = 0.40
0.35
0.30
X_{CB} = 0.20
0.10
X_{CO} = 1
50 µm

Figure 48: PLM analysis of CB/CO blends after crystallizing isothermally at 22 °C for 24 h and then heating the sample to 90 °C and cooled down to 10 °C with 2 K/min rate for studying the effect of dynamic crystallization. The eutectic composition is marked in a red square. Scale bar = 50µm.

The morphology can be described as a high number of small size crystallites along with some spherulites having a needle-like structure at the periphery (indicated by red arrow for X_{CB} = 1). For pure CO, a sharp needle structure is observed at 22 °C, however, in the case of DSC, no sharp melting is detected.

After heating at 90 °C and cooling down to 10 °C, the formation of crystal morphology shows the visualization of the crystallization process from DSC (Figure 44 (b) and Figure 45 (a)). For all pure components, the crystal size is changed to smaller and denser as compared to isothermal crystallization. In the case of pure CB, the crystals are the aggregation of small needles. Similarly, for pure CO, the combination of small denser spheres and granular structures is formed.

Furthermore, the effect of the addition of different fats on the crystal morphology of pure CB was further studied. In contrast to CB/TS blends (in section 2), a mixture of CB and CO shows various changes in crystal morphology depending on the CO concentration after 24 h. For X_{CB} = 0.90, spherulitic morphology is observed, likewise, 0.80 and 0.70 also showed the combination of needlelike and spherulitic crystal nature. However, at 0.60, more sharp needles are viewed as compared to spherulitic. For 0.50 and 0.60 compositions, the size of spherulites is reduced and so is the amount of crystallinity of the whole sample blend. As the concentration of CO increased further, more sharp needlelike crystal morphology is captured. After dynamic crystallization, the size of crystallites decreased drastically which is in agreement with CB/TS results.

In the case of the eutectic composition ($E_{CB\text{-}CO}$) which is X_{CB} = 0.35, the least crystals as compared to other blends are detected, therefore, this morphological observation is in agreement with the DSC results where the lowest melting temperature is determined as compared to the other blends.

3.4 Effect on quiescent crystallization kinetics of CO on CB

To analyze in more detail the influence of CO addition on thermal properties of CB/CO blends, isothermal crystallization studies in terms of the solid fat content (SFC) were carried out. Figure 49 (a) shows the SFC content profile for all CB/CO blends after reaching 22 °C from 90 °C at the cooling rate of 0.5 K/min with respect to time (24 h). In Figure 49 (a), each color indicates the SFC profile for each different concentration of CB (in terms of X_{CB}). According to the SFC profile, at 22 °C, the solid fraction is decreased after the addition of CO. In the case of CB, ~70% of SFC is obtained at 22 °C after 24 h, whereas, ~23% is detected for pure CO at 22 °C. To get further insight into the trend of the SFC decrease after the addition of CO in CB, the SFC value after 24 h at 22 °C is plotted in Figure 49 (b) with respect to the concentration of CB (X_{CB}). Figure 49 (b) represents that the SFC value is decreased until the formation of the eutectic mixture of CB/CO and increased later for the remaining blends. A similar result could be observed with DSC experiments in section 3.1, where, the melting temperature is decreased until eutectic is reached and increased again for further concentrations. Hence, the reason for the least melting temperature for eutectic mixture could be explained as the less amount of solids can crystallize at 22 °C for eutectic mixture, which results in a quick melting as compared to the other blends of different composition. This result is also in agreement with the microscopy observations from Figure 48, in which the least crystallization is to be visible for $X_{CB} = 0.35$.

For further understanding of crystallization kinetics profile, these SFC profiles are fitted by using the Avrami equation. After fitting the Avrami model to the present data, the parameters: Avrami constant (k), Avrami exponent (n) are obtained. The fitting parameter values are described in Table 9. According to the fitting parameters, the Avrami constant (k) value of all the samples does not depict any significant difference with respect to the concentration of CB. Hence, the ability to describe the crystallization rate in terms of the 'k' value is minimal. Furthermore, Avrami exponent (n), originally meant to reflect the crystal growth geometry, provides kind of evidence about nucleation and growth mechanism [21], [23]. The phenomenological Avrami equation addresses the crystal growth as a combination of the function of the time dependence of nucleation and the number of dimensions in which growth takes place. Nucleation is either instantaneous, with all nuclei appearing at once, or sporadic, with the number of nuclei increasing linearly with time. Crystal growth could be

either spherical, plate-like, or needle-like in three, two, or one dimension respectively. According to the original model, the exponent *n* is an integer, however, in all real experiments, fractional values are observed, due to the simultaneous development of more than one type of crystal. In this study, the fractional values obtained after fitting the equation, which explains either the aforementioned reason or similar crystals from different types of nuclei [11].

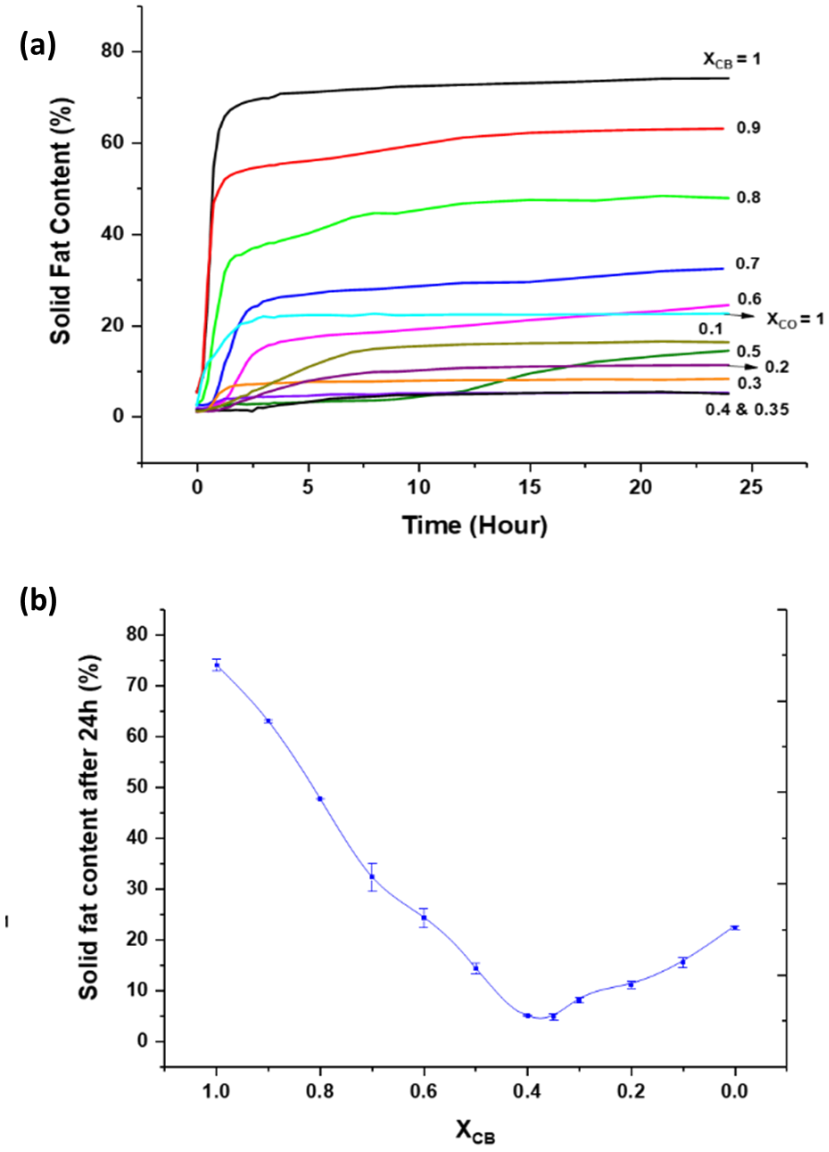

Figure 49: (a) Effect on solid fat content (SFC) profile after addition of CO in CB with respect to the 24 h timeline at 22 °C. (b) SFC content distribution after 24 h at 22 °C with respect to the weight fraction of CB (X_{CB}).

The exponent *n* of pure CB (*n*=2.69, which is more close to ~3) indicates either plate-like growth from sporadic nuclei or spherical growth from instantaneous nuclei. By comparing this

result to the microscopy images (figure 45_after 24 h at 22°C), spherical growth is observed hence, the spherical growth from instantaneous nuclei. For considering instantaneous nucleation can be due to high degrees of supercooling, resulting into lower free energy and higher rate of nucleation hence formation of large number of nuclei [11]. After the addition of CO in CB, the '*n*' value is decreased until the mixture X_{CB} = 0.7. According to the Avrami equation, this value (*n*=2) represents either plate-like growth from instantaneous nuclei or rod/needle/fiber-like crystal growth from sporadic nuclei formation. By comparing this result to the microscopy images, spherical crystal growth as a result of aggregation of needles is observed for X_{CB} = 0.9 and 0.8, whereas, clustered microstructure composed of small needles is captured for X_{CB} = 0.7. Therefore, the contradiction of the original assumptions of the Avrami exponent value with respect to the microscopy experiments is visible and shows generally that the growth process during crystallization can generally not be described by the oversimplified models as suggested by the Avrami model. For X_{CB}= 0.6, the exponent value increased to 3.21. This value exhibits either plate-like growth from sporadic nucleation or spherical growth from instantaneous nuclei. After comparing to the microscopy image, the combination of spherical microstructure composed of a small number of granular crystals and random orientation of small needle-like microstructure is visible. Thus, the exponent value does not correlate with the microscopy result. Hence, the limitations of the Avrami equation can be understood from this observation. For the next mixture of X_{CB} = 0.5, the value decreased to 1.16. This value indicates, rod-/needle-/fiber-like growth from instantaneous nuclei. By comparing this observation from exponent value to the microscopy image, the spherulitic microstructure composed of a needle-like structure is observed. Another observation is that according to Figure 49 (a), the nucleation process is a relatively long time as compared to the other samples due to the presence of a long plateau region. This provides that the formation of stable nuclei requires a longer time to acquire. Thus, this crystallization kinetics represents the delay in the formation of nuclei along with providing a hint towards the formation of sporadic nucleation at random places instead of instantaneous nucleation.

For eutectic mixture X_{CB} = 0.35, the exponent value depicts either plate-like growth from instantaneous nuclei or rod-/needle-/fiber-like growth from sporadic nuclei. After comparing to the microscopy image, a spherulitic microstructure composed of small needles is formed. For further concentrations, long needles arranged in tree branches like structures originated from the edge and progresses towards the center of the coverslip. This result from Avrami fit is in agreement with the morphological results. Thus, due to the presence of co-

crystallization effect in the case of higher concentration of CB as well as the presence of different morphology for other blends, the fitting of the Avarmi model to CB/CO blends provides ambiguous fitting parameters. Therefore no specific conclusion with crystallization rate (constant *k*) can be made, likewise, the contradiction with exponent value for some blends with respect to the microscopy images is found.

Table 9: The values of Avrami constant (*k*) and exponent (*n*) for the addition of CO in CB.

X_{CB}	*k*	SD_*k*	*n*	SD_*n*	R^2
1 (CB100)	2.66E-05	3.83E-05	2.69	0.3683	0.9812
0.9	3.96E-04	3.14E-04	2.18	0.2200	0.9889
0.8	2.48E-04	1.60E-04	2.01	0.1558	0.9904
0.7	3.59E-05	2.54E-05	2.16	0.1491	0.9849
0.6	1.57E-07	2.66E-07	3.21	0.3483	0.9746
0.5	1.95E-09	1.39E-09	2.93	0.1046	0.975
0.4	0.00517	0.00273	1.16	0.1121	0.9415
0.35 ($E_{CB\text{-}CO}$)	1.06E-06	8.08E-07	2.33	0.1297	0.9685
0.3	3.49E-04	2.64E-04	1.86	0.1760	0.9728
0.2	4.75E-04	6.71E-05	1.34	0.0242	0.9937
0.1	7.69E-05	7.45E-06	1.66	0.0169	0.9985
0 (CO100)	2.09E-04	4.37E-05	1.76	0.0431	0.9939

Furthermore, the mechanism for the formation of a eutectic mixture needs to be understood. The formation of a stable crystallization nucleus requires total overcome a certain (free) energy barrier determined by the balance of volume and surface energy. As seen from the preliminary experiments, the formation of nuclei and the crystallization of CO initiates from the edges of the vessels or microscope slides and progresses to the center.

A) Due to the structural differences between TAGs of CB (monounsaturated TAGs), the attachment of these TAGs to the short-chained saturated TAGs increases the total free energy. On the contrary, the detachment of CB crystal from CO crystals reduces the free energy to the states of higher preference.

B) Another aspect arises from the supercooling as the crystallization temperature is 22 °C (CT), which is close to the melting temperatures of CB and CO. The CB and CO crystals have an ample amount of time to arrange the best possible lamella having stable 3D nuclei with the least amount of free energy and surface energy. Therefore, the demixing of CB and CO could take place except for the crystals formed at eutectic mixture composition.

Similar results were achieved by the study of Hartel and the group showing a decrease in crystal growth after the addition of lauric fat due to diluent interaction between them [90]. Therefore, irrespective of the process conditions, CB/CO mixtures tend to form a eutectic mixture. Thus, the delay in the crystallization rate of CB/CO blends is confirmed.

3.5 Effect on oscillatory crystallization kinetics of CO on CB

To compare the result with crystallization kinetics under quiescent conditions, the effect of continuous oscillation on crystallization kinetics was studied further. The sample was crystallized during rheometer experiments by using a temperature sweep from 90 °C to 22 °C followed by a time sweep for 2 h 30 min. This particular time was selected after studying the effect on morphology under polarized light microscopy where the crystal growth was obtained in a plateau manner for higher concentrations of CB. To understand the viscoelastic behavior of the forming crystal network, the amplitude sweep was carried out after 2 h 30 min at 22 °C. In figure 47 (a), the graph of storage modulus vs. temperature/time superposition is shown. Each color indicates a different blend of CB/CO representing with respect to the weight fraction of CB (X_{CB}). In the graph for all blends, the samples were in a liquid state until the point where storage modulus crossed loss modulus and increased thereafter. This crossover point is considered as the crystallization temperature (CT) for each blend. At CT=26 °C, X_{CB}=1 is started to crystallize. After the addition of CO in CB, for X_{CB}=0.9 and 0.8, the CT value is decreased to 25 °C and 22.5 °C respectively. For further blends, the CT is 22 °C. Thereafter the time required for crystallization at 22 °C is monitored. The maximum time required for a crossover of storage modulus and loss modulus is for X_{CB}=0.5 (~9 minutes for crossover point of *G'* and *G"*), which is also in agreement with the SFC profile of this blend. The activation energy barrier for the formation of stable nuclei might be high for this blend as compared to others and hence required more time for crystallization. As explained earlier in the introduction, the formation of stable nuclei is dependent on increasing supersaturation and temperature and decreasing interfacial tension [19], therefore, the precise reason for inhibition of nucleation for this particular blend is difficult to address.

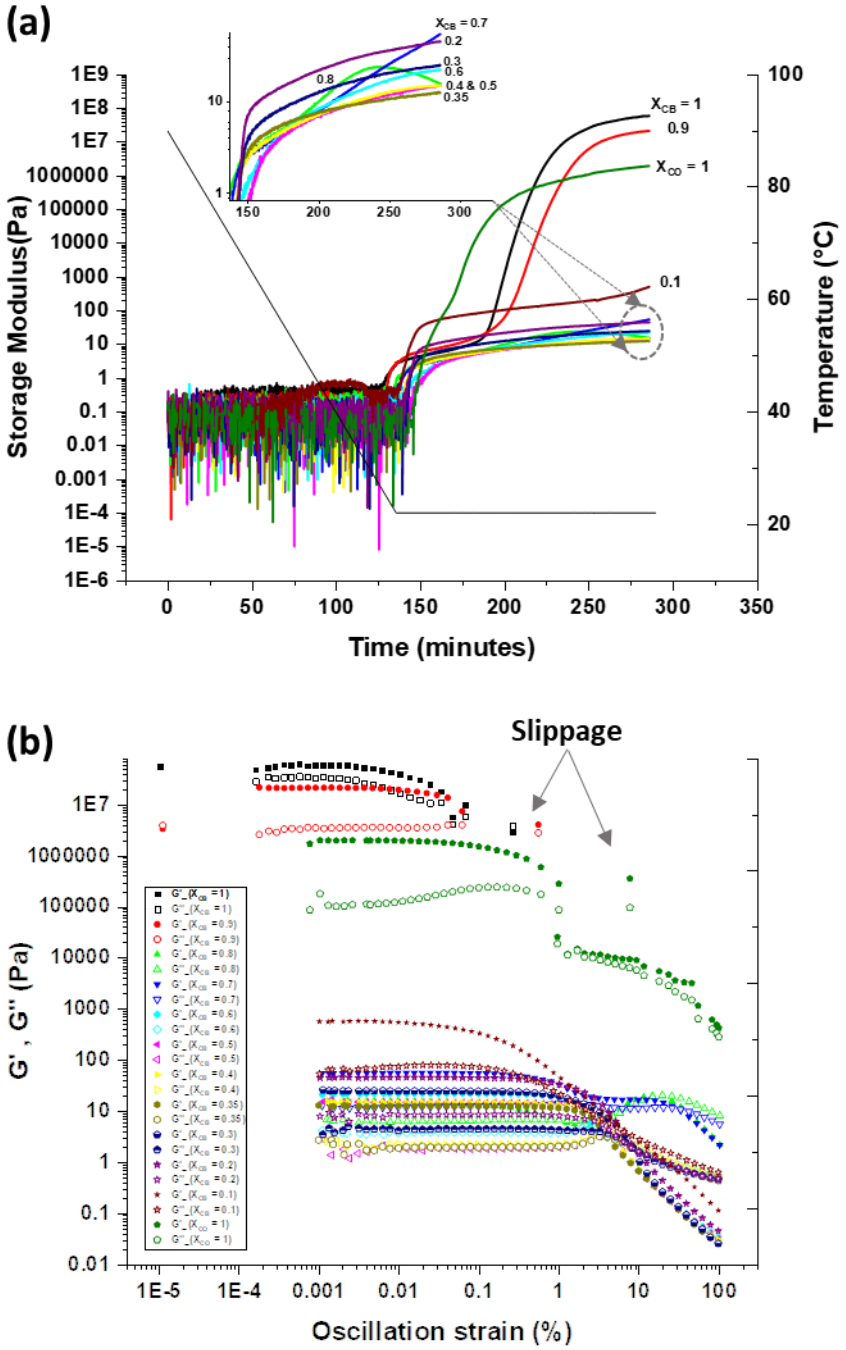

Figure 50: Effect on rheological properties after addition of CO to CB. (a) Represent temperature and time sweep plotted against time in minutes and black graph profile is the temperature vs. time which provides precise temperature detection with respect to rheological properties for CB/CO blends. (b) Represent the amplitude sweep profile for the same sequence. The slippage occurs in the case of X_{CB} = 1, 0.9, and X_{CO} = 1 samples due to high rigidity to jamming of needlelike morphology at higher strain value respectively.

For understanding the variation in rheological properties of CB/CO mixtures during temperature and time sweep, only storage modulus is considered for better visualization. The storage modulus (*G'*) decreased after the addition of CO as similar to NMR results. The least storage modulus is obtained for the eutectic mixture (X_{CB}=0.35) as shown in the magnified view in Figure 50 (a). During crystallization, two-step crystal growth of for X_{CB} =1, 0.9 and pure CO is observed, which suggests that either polymorphic transition or co-crystallization of two polymorphs is occurring [91]. As explained in section 2.3.3, SAXD and WAXD peak analysis for pure CB after 24 h indicates the formation of two polymorphs (Form IV and V), this confirms co-crystallization of two polymorphs. Furthermore, after addition of 10 wt% CO in CB, the occurrence of two polymorphs could not inhibit, hence, two-step crystallization kinetics is observed. However, in the experimental timeline, the addition of a higher concentration of CO in CB leads to the formation of one-step only. This result indicates that for more concentration of CO in CB, there is neither co-crystallization nor polymorphic changes occurring. Hence, CO addition is inhibiting the crystallization process by preventing either the co-crystallization or polymorphic transition. Following to the step-growth crystallization, the plateau region is attained, which indicated no further solid-solid transition. Therefore, the amplitude sweep is performed for understanding the viscoelastic properties of the crystal network.

In Figure 50 (b), the amplitude sweeps for all CB/CO blends are shown. Filled symbols represent the storage modulus (*G'*) and empty symbols indicate the loss modulus (*G''*). For pure CB and X_{CB}=0.9, the measurements could not proceed beyond strain of 0 .1% due to slippage. Also for pure CO, the slippage occurs from 1 to 10% of strain.

Most of the previous work on fat crystals is performed in LVE range as it focused on interaction forces that holding the crystal network. In the LVE range, the inter-particle in the current case of crystal aggregate network hold together by van der Waals' attractive and Born's repulsive forces [92]. These forces can also be denoted as the bonds between the particle-particle clusters. Therefore, with a small amplitude, the stretching of these bonds between particles is small enough to regain its potential. For CB/CO blends, the LVE range is increasing after the addition of CO in CB as the solid fat content decreases and hence the connection between aggregates is underdeveloped.

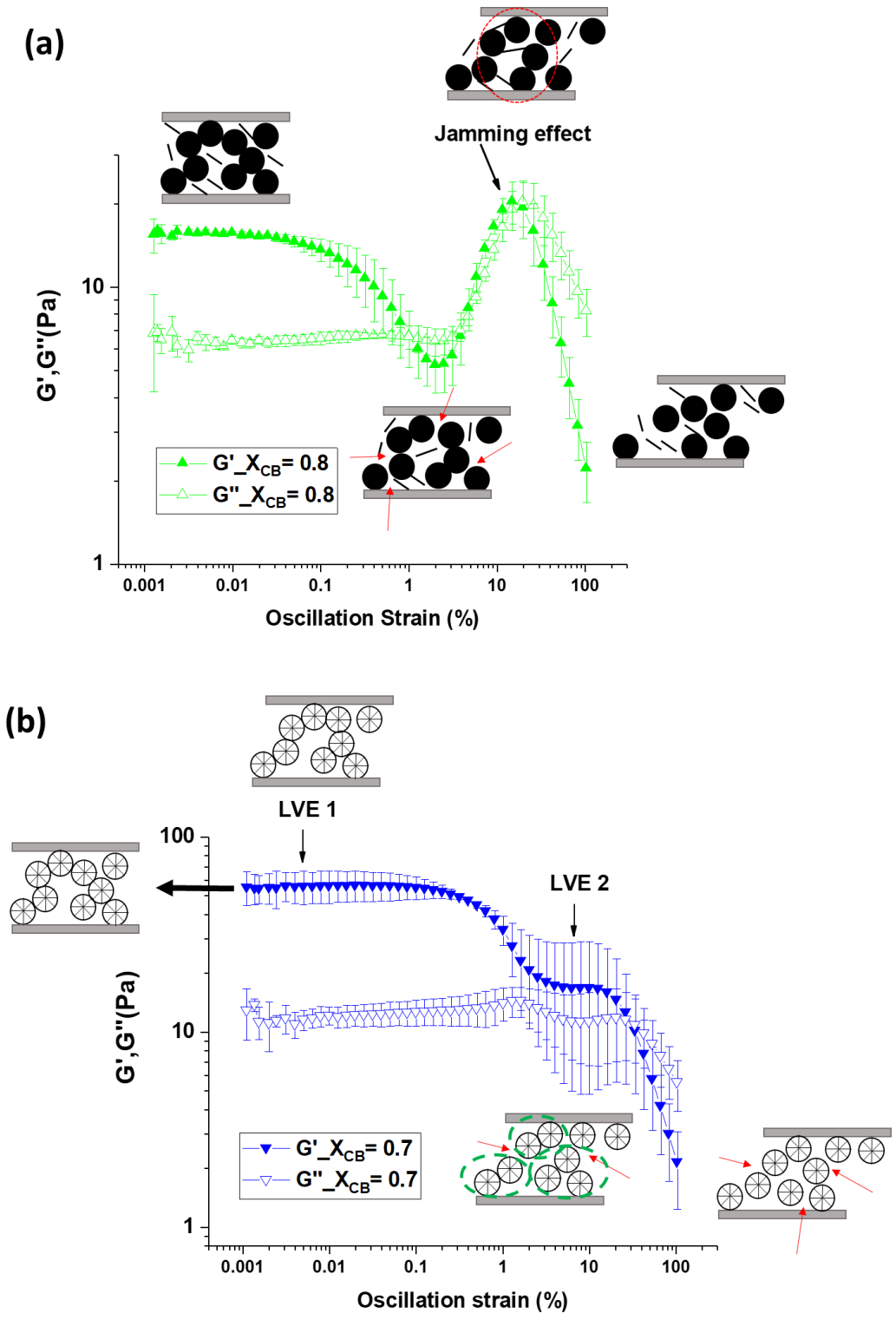

Figure 51: Amplitude sweeps after 2 h 30min at 22 °C for (a) X_{CB} = 0.8 (b) X_{CB} = 0.7. Red arrows indicate the breaking of connectivity between crystal networks. The red dotted circle in (a) represents the jamming of needles and spherulites. The green dotted circle in (b) indicates that the connectivity between some crystal blobs is strong enough to regain its potential at the higher strain and hence indicating the LVE 2 regime.

As the LVE regime is focused on elastic deformation, the NLVE regime undergoes plastic deformation [59]. Therefore breaking of these bonds takes place at large amplitudes. The fracture of these bonds is strongly dependent on the measure of bond stretching. These all different blends show unique behavior of breaking the crystal network as each blend show variety of (mixtures of needles and spherulitic) morphology under crystallization. In the current study, three types of network breakup are typically observed. 1) For X_{CB}=0.8, breakage of the crystal network occurs after LVE, which is followed by an increase in *G'* and *G''* before the whole crystal network is destroyed (as shown in Figure 51(a)). The reason for such behavior could be the jamming effect. As can be seen from microscopy images, the small needlelike growth is developed and after breaking the primary network, these needles are jammed in between the remaining crystals, which results in an increase in the moduli. Thereafter an increase in further strain, help to remove these jammed needles from the remaining spherulitic network, which is followed by the destruction of the whole crystal network. Hence the increase in *G'* is occurred.

2) For X_{CB}=0.7, two LVE ranges are obtained from 0.001% to 0.1% and from 1% to 10% as shown in Figure 51(b). For further explanation, a simplified schematic in which a crystal blob consisting of an aggregation of needles is considered. After LVE1, the microfractures are developed between the linking particles between the clusters, 'interblob', which are bonded together to form the crystal network. Whereas for LVE2, either the connectivity of some crystal blobs' is strong enough to stay intact with high oscillation strain due to higher strength between the bonds, or the connection within the crystal blob can be referred as 'intrablob connections' have regained their potential. However, the precise reason for such behavior is yet to understand. 3) For X_{CB}=0.35, only a small number of crystals are formed which are not interconnected. Hence, the breaking of this blend could refer to the dissolving of small crystals back to a liquid and small fractures in individual crystals.

For a better understanding of the strain-dependent breaking of crystal structure, in-situ microscopy was used under rheological measurements. Figure 52 shows the amplitude sweep along with microscopy images indicating the breaking of the crystal network for CB. The amplitude sweep was carried out after 30 minutes instead of 2 h 30 min to protect the glass plate (as an increase in modulus (solidity) could destroy the glass plate, which was used instead of stainless steel plate). The videos were captured from the upper plate towards the lower plate (Appendix video V1). These videos were taken at the edge of geometry instead of the center, as the amplitude is higher at the edge hence the movement was easy to capture. Images

extracted from these videos are shown in the graph, where it can be seen that for the LVE range, the network is just moving altogether with the small amplitude, as the amplitude increased the crystals network brake down into individual crystals and these crystals are leaving its cage with large amplitudes. The movement of the caged crystal is noted by using a red dotted elliptical. Overall, the breaking of the crystals takes place gradually, as per the amplitude. As the amplitude increased the bonds at weak link breaks and the 3D network breaks into pieces, while further increase in oscillation strain, the cracks or fractures develop at further points or links and continue until each crystal separates from each other and slide along each other as the amplitude increases further.

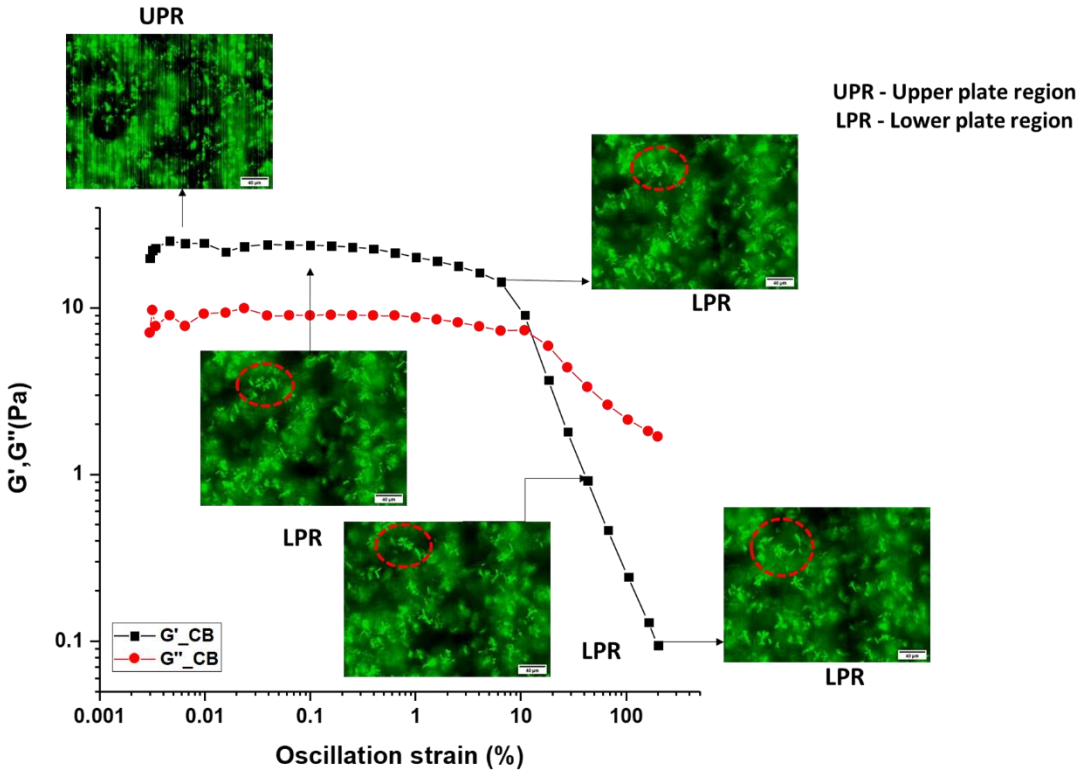

Figure 52: In situ microscopy to CB sample representing the amplitude sweep after 30 minutes at 22 °C. The videos during amplitude sweep are taken from the upper plate towards the lower plate, hence individual images with a change in crystal network with respect to the amplitude are marked with a red zone. The scale bar = 40µm.

In case of pure CO, the slippage occurred at 1% to 10 %, therefore, in order to understand this in more depth, in situ rheo-microscopy was performed. For CO, the crystallization has occurred

at the edges of geometry, and hence at high amplitude, the plates were slipping and moving faster than expected. The directly visual observation shows, as the amplitude increased, small branches of needles detach from the mother branch of the tree-like structures and these small needles further promote slippage. They are caged between the mother branches, hence for higher amplitude, proper values cannot be detected. However, after breaking off small needles the mobility of the upper geometry becomes smooth again and hence the measurement took place in a correct manner (Appendix video V2).

3.6 Fractal nature of fat crystal networks

A quantitative description of the structure of fat aggregates is evaluated in terms of the fractal dimension, which quantifies how the mass of a cluster increases with its size. In the current study, the relation of a mass of cluster with respect to the time is studied by polarized light image analysis. The sample was cooled down to 22 °C from 90 °C at the rate of 0.5°C to ensure the uniform temperature change over the whole sample volume and then kept at 22 °C for 24 h. The images were captured for each minute throughout 24 h to observe the crystallization process. For the determination of the fractal dimension of such a large image dataset, the automatic MATLAB program was used. The detailed description of the program is explained in chapter 2. The analysis of only four samples is shown here as the images are taken at the center position of microscopic slides, the samples with a higher concentration of CO could not be crystallized in the center part as explained earlier the process progressed from the edge towards the center. Hence, precise crystallization kinetics were not able to obtain.

In Figure 53 (a), the graph between D_b and logarithmic time is shown for various concentrations of CB. Each color represents a different set of the mixture. The error bars are relatively high as the box count is dependent on the threshold chose during the binarization of images. For pure CB (X_{CB}=1), two plateau regions are detected. At the beginning of the crystallization process, the primary crystals are formed, which could be the aggregation of HMF. After attaining the stable radius, the slow crystal growth is observed for ~20 minutes (1^{st} plateau). Then steep increase in D_b value indicates fast crystalline growth until the connectivity between crystal-blob aggregates is attained. This two-step crystallization is observed for three concentration with X_{CB} = 1, 0.9, 0.8. To provide an example, the set of binary images of X_{CB} = 0.9 is shown in Figure 53 (b). Wherein the crystallization with respect to the 24 h timeline is shown.

According to these images, at 0 min, small black crystals are captured already as explained earlier crystallization of CB takes place earlier than 22 °C. While at 10 minutes, the increase in crystal mass is visible. This crystal mass increases slowly (1st plateau) until 1 h 40 min. Following the 1st plateau region, the size of the crystal increases as the crystallization process progresses, which corresponds to the 2nd step in a graph. After 2 h the size of crystals becomes nearly constant or the increase in the mass of the crystal is very slow (2nd plateau). According to the images from 2 h 30 min to 24 h, a minute difference is observed as compared to the earlier timeline. This observation provides that the system goes towards equilibrium. Therefore, a 2 h 30 min timeline is considered for crystallization kinetics under rheometer and thus the amplitude sweep for understanding the crystal network. For understanding the crystallization kinetics related to the 2nd growth step, the linear fitting of the data is carried out, which provides the reduction in the slope of a line as the concentration of CO increases (m_{CB} = 0.96±0.04; m_{CB90} = 0.47±0.01; m_{CB80} = 0.24±0.01). This result suggests that, as the concentration of CO increases, the inhibition in co-crystallization is achieved, which supports the current hypothesis from crystallization kinetics with the analysis using rheometer. Hence, for the X_{CB} = 0.7 sample, only one step of crystallization is observed, which is in accordance with the crystallization kinetics by using the rheometer (refer to Figure 50 (a)) over the time period. Therefore, the study of D_b over time shows that it's a time-dependent parameter, which displays the connection between mass and spectral connectivity with time. However, the result obtained from microscopy images is in 2D, hence the obtained fractal dimension value is also within the 2D region, whereas, the fat crystal network is formed in the 3D network [93]. Therefore, the Kraus model fitting to the amplitude sweep is used to achieve the precise fractal dimension value.

The Kraus model-fitting method for amplitude sweep was implemented for all the blends of CB/CO. In Figure 54 (a), the Kraus model fitting is shown for X_{CB}=0.5. After fitting the Kraus model to the amplitude sweep, fitting parameters *K* and *m* values are obtained. By using equation 1.20 (chapter 1), the fractal dimension is calculated. In Figure 54 (b), the change in fractal dimension with respect to the concentration of CB in the blends is shown. In the case of X_{CB} = 0.8, the fitting of the Kraus model was invalid due to an amplitude sweep profile (refer to Figure 51(a)). Whereas, for X_{CB} = 0.7, the data from LVE1 was fitted to calculate the fractal dimension value. Thus, according to Figure 54 (b), the fractal dimension is higher/larger than 2, which suggests that the 3D fat crystal network is achieved.

(a)

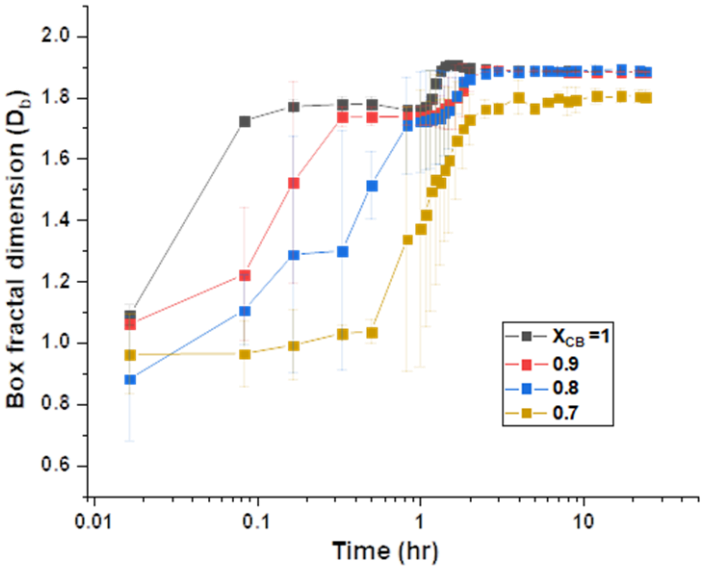

(b)

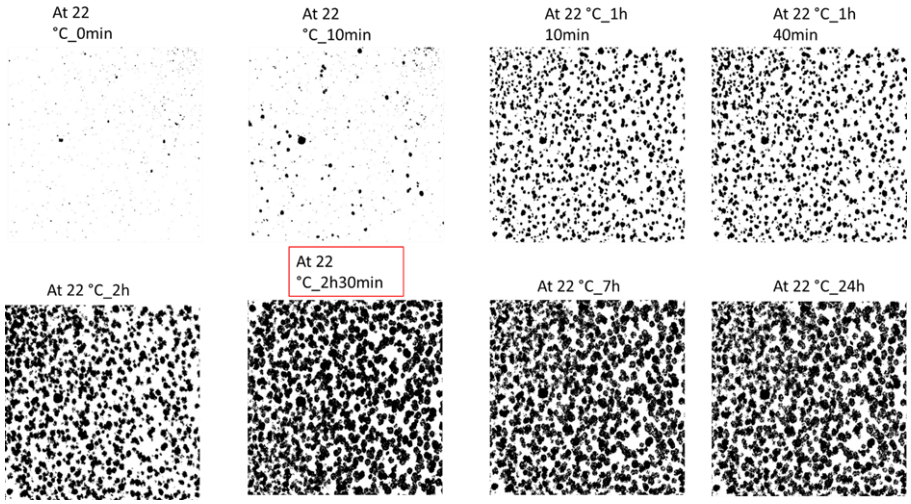

Figure 53: (a) The correlation between box fractal dimension and time for different concentrations of CB in CB/CO blends. (b) The thresholded images showing the increase in the mass of crystals with respect to the timeline of 24 h at 22 °C.

The d_f value is decreased to below 2 for the pure CO and 90 wt% of CO in CB, hence, providing a hint towards the formation of a 2D crystal network. This result is in good agreement with the morphological observation as well as the Avrami exponent value, in which the spherulitic crystal network transformed into a needlelike crystal network. This concludes that the crystal growth mechanism and the possible expected nucleation of the fat crystal are related to the

fractal dimension. As the fractal dimension is a combination of mass and spectral dimension, the crystal growth can be predicted.

Another aspect of fractal dimension relation is that as higher the fractal dimension is, the lower the solid fat content and hence, the softer the material is. For instance, in the case of blends of CB/CO, for mixture from X_{CB} = 0.7 to 0.3, the mixture shows the least SFC content, storage modulus, and melting temperature as compared to other mixtures, whereas high value of the fractal dimension (d_f) at 22 °C. Thus, the product containing mixtures of X_{CB} = 0.7 to 0.3 will be softer with a good spreadability effect due to fewer intercrystalline interactions [94], [95]. For instance, the fat crystal network for the above-mentioned blends is underdeveloped at this particular timeline, i.e. crystal blobs are not very well connected hence not able to hold the crystal network due to weak van der Waals interactions, therefore, referred as less intercrystalline interactions. Similarly, the series of experiments performed to calculate the particle (D_f) and box-counting (D_b) fractal dimension by using PLM images to develop a model that describes the rheological properties based on microstructural features by Narine and Marangoni [28], [96] and Awad et.al [97]. According to their study, larger crystals have been associated with softness and spreadability, whereas, small crystals correspond to a harder structure and lower spreadability. Therefore, altogether the current results also confirm that there is a correlation between morphology, the shape of crystals, and fractal dimension.

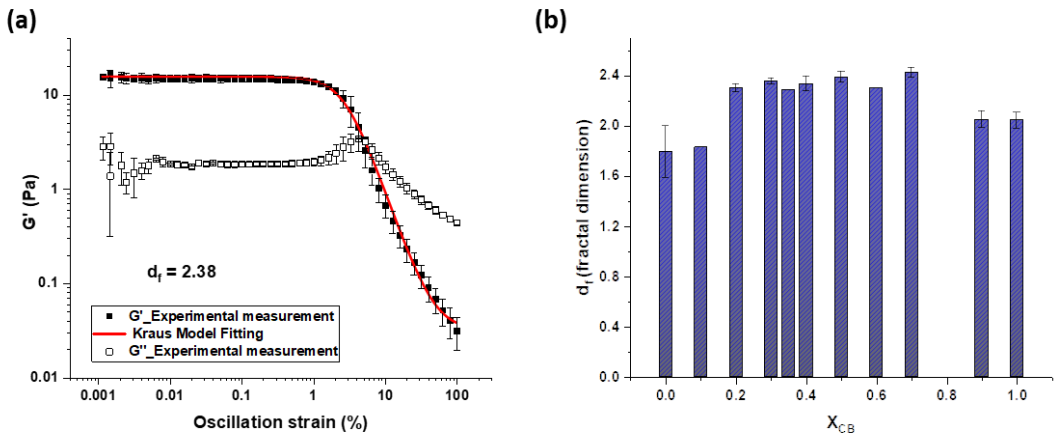

Figure 54: (a) Kraus model fitting to the experimental data of X_{CB}=0.5 (b) The deviation in fractal dimension with respect to the concentration of CB (X_{CB}).

Several other studies also pointed out that the relation of SFC with fractal dimension. These are characterized based on D_f, D_b through modeling and computer simulations.

According to their studies, 3D box-counting fractal dimension (D_b) and particle counting fractal dimension (D_f) was calculated based on 3D-FD software for a high melting fraction of milk fat. The distribution of the fractal dimension was characterized based on solid fat content. D_b (1.87 to 2.09) was increased as the SFC increased from 5 % to 9 %, while in the case of $D_{f,}$ (~2.73), the value remains unchanged with respect to the SFC. Similar results were achieved after the simulation. Thus the study revealed that D_b was sensitive to the area fraction and crystal size and not affected by distribution order, whereas, D_f is not affected by area fraction, randomness, and crystal size [98]. Similarly, the study on the modified fractal model and rheological properties on colloidal networks of HMF of milk fat, anhydrous milk fat (AMF), palm oil, and cocoa butter showed that for high SFC content less fractal dimension value was achieved in comparison to low SFC [99]. To summarize, the thermal, rheological properties are dependent on the interactions between the particles at the microscopic level.

Furthermore, for calculations of fractal dimension in fat crystal network (rigid system), Kraus model provides precise value as compared to the power-law for the relation between *G'* and a solid fraction (SFC) which is widely used in fat crystallization [93], [100]. As the fractal dimension is calculated from the slope of the logarithmic graph of *G'* with solid fat content, the experimental values are to be considered for plotting the graph are in different time zone. Hence, the fractal dimension value is the average value to be achieved. As the current study shows that the fractal dimension is a time-dependent parameter, these values should be interpreted vigilantly for a proper understanding of the fat crystal network.

3.7 Effect of nanoscopic arrangement on macro or mesoscopic properties

To get deep insights into the formation of the eutectic mixture, the effect on lamella spacing and crystal domain size is calculated by using X-ray diffraction experiments. In Figure 55, the graph of intensity vs. scattering vector for pure CB, CO, and $E_{CB\text{-}CO}$ after 24 h at 22 °C is shown. As discussed in detail regarding CB polymorphism at 22 °C in chapter 4 section 4.3.3, the crystal forms IV and V with 2L and 3L are formed after 24 h at 22 °C. Whereas, in the case of pure CO, the lamella spacing is calculated as ~ 34.06 ± $9.2e^{-3}$ Å and subcell structure with WAXD peak at ~4.34, 4.15, and 3.84 Å. According to the previous studies on understanding the polymorphism behavior in CO, α and β' form have lamella distance of 38.4 and 32. 9 Å and sub-cell structure with WAXD peak at 4.12 and 4.29; 3.83 Å respectively. However, in

their study, while heating process, at 12 °C, another crystal form (CO-β') having lamella spacing at 33.5 Å and short spacing at 4.3, 4.16, and 3.84 Å are formed. According to their study, CO-β' crystal form is a solid solution of α and β' fractions [101]. Hence, after comparing the subcell packing dimension as well as lamella distance of the present study with the previous work, at 22 °C, CO-β' crystal form may form. Further, a similar experiment was carried out on $E_{CB\text{-}CO}$ to understand the effect on polymorph formation. $E_{CB\text{-}CO}$ crystallized at 22 °C with lamella spacing of ~36.6 ± $3.7e^{-2}$ Å and sub-cell structure of 3.85 Å. As the eutectic sample is not completely crystalline at 22 °C, the peak intensity is very low as compared to CB and CO. Therefore, the same sample is measured at 10 °C after cooling from 22 °C. $E_{CB\text{-}CO}$ crystallized at 10 °C with lamella distance of ~36.6 Å and sub-cell structure with the WAXD peak having strong signal at 3.85 Å along with broad-spectrum containing 4.3, 4.16 Å. Along with the SAXD main sharp peak, another shoulder peak is also detected having ~44 Å lamella distance. This behavior suggests that two different lamellae are forming at a lower temperature. Although DSC results (Figure 44) detected the single crystallization and melting peak at X_{CB} = 0.35, at the nanoscale, the incompatibility of CB and CO at this particular concentration still occurs at a minor level. Due to the presence of different polymorphic forms of two fats along with the differences in chain length and degree of unsaturation, the weak co-crystallization is visible. Thus, the lamella spacing of the $E_{CB\text{-}CO}$ is higher as compared to CO. Additionally, there is more than one unit of cell spacings observed in the case of both $E_{CB\text{-}CO}$ and CO, which excludes the possibility of formation α polymorph instead of CO-β' in $E_{CB\text{-}CO}$. Therefore, all these observations provide a hint of the possibility of the formation of mixed crystals with CB-CO.

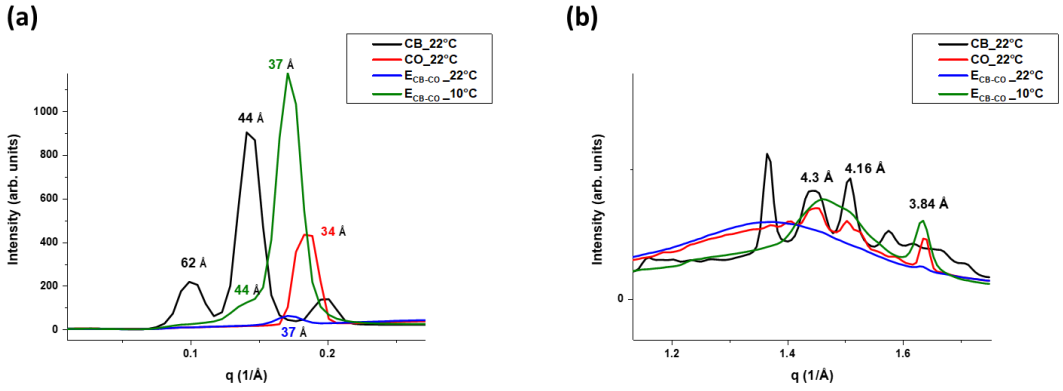

Figure 55: The X-ray profile of pure CB, CO at 22 °C after 24 h and for $E_{CB\text{-}CO}$ at 22 °C after 24 h and at 10 °C. (a) SAXS profile showing the change in lamella spacing (b) WAXS profile indicating subcell packing.

To understand the correlation between nanoscale interactions to the mesoscopic properties of fat blends, a mathematical formulation of the relation between Young's modulus with the forces acting between particles or flocs was developed by Narine and Marangoni [28], [102], [103]. This is further developed for understanding the relation between storage modulus and nanoplatelet size. The equation is given by:

$$G = \frac{A}{6\pi\gamma a {d_0}^2}\,\phi^{\frac{1}{d-D}} \tag{3.1}$$

Where G = Storage modulus (Pa); A = Hamaker coefficient, describes the interaction between two slabs of nanocrystalline fats separated by an oily medium; ϕ = solid fat content (%); d = Euclidean dimension of the embedding space; D = fractal dimension; γ = strain at the limit of linearity; a = nanoplatelet diameter (nm); d_0 = is the equilibrium distance between flocs (nm). According to their calculation, in the case of fully hydrogenated canola oil (FHCO), as a media and medium is high oleic sunflower oil (HOSO), G = $6.78*10^6$ Pa was acquired, when, A= $0.55*10^{-21}$ J, d_0 = 0.39 nm; a =109 nm; ϕ ~1 and γ = $1.9*10^{-4}$ was used [104]. This estimated value is in agreement with the experimental values. Similarly, this equation was used to calculate approximately the nanoplatelet diameter (a) from experimental storage modulus values of the current study. For calculation, the values for A, γ were assumed to be the same for all three samples, whereas, d_0 values in the case of CB and CO were assumed to be similar to the HOSO and FHCO study. For CB, $E_{CB\text{-}CO}$, and CO, the solid fat content value at 22 °C is assumed to be after 2 h 30 min as the time sweep is carried out for 2 h 30 min. As the solid fat content for $E_{CB\text{-}CO}$ is relatively low as compared to CB, the equilibrium distance between floc will be relatively high hence, the 15 nm value is assumed for calculation. Therefore, depending on the assumed values and experimental values, the nanoplatelet diameter is calculated. The detailed assumed values and calculated values for three samples CB, $E_{CB\text{-}CO,}$ and CO are shown in Table 10.

According to the calculations, the smallest nanoplatelet diameter for CB at 22 °C is achieved whereas, the largest diameter was achieved for a eutectic mixture. This result shows that the relation of mesoscopic properties of fats is in inverse relation to the nanoplatelet size, as the smaller the size of nanoplatelet, the higher the storage modulus as well as the higher the melting temperature. For instance, the smaller the size, more surface area for interaction is available, and resulting in compact packing. This is in agreement with the previous finding. Unfortunately, from XRD measurements only the nanoplatelet thickness is achieved. To obtain

the nanoplatelet diameter, width and length needs to be determined as well. Hence, to confirm these estimated values, further experiments with Cryo-TEM need to be performed.

Table 10: Approximate estimation of nanoplatelet size (a) based on experimental values. The calculated values are indicated by a red rectangle.

Parameters	CB100	E_{CB-CO}	CO100
G' (Pa)	3.51E+07	12.39938	1.55E+06
A (J)	5.00E-22	5.00E-22	5.00E-22
γ	0.0001	0.0001	0.0001
a (nm)	30.62	332.12	296.23
d_0 (nm)	0.39	15	0.39
ϕ	0.63	0.018	0.2
D	2.04477	2.2899	1.79472
d	3	3	3

3.8 Summary of CB/CO blends

To summarize this study, CB/CO blends show incompatibility due to the difference in the molecular structure, presence of different polymorphs, and their arrangement. Phase diagram analysis shows the eutectic behavior tends to occur and X_{CB} = 0.40, 0.34, 0.35, and 0.36 describe as a eutectic mixture, however, 0.35 being the great extent of eutectic behavior. This DSC result is in good accordance with the microscopy results, solid fat content, and storage modulus.

Furthermore, the relation between d_f (fractal dimension from Kraus model) to D_b (box-counting fractal dimension) reveals that the fractal dimension is dependent on time and to add 1 to D_b to achieve a 3D value is not recommended. Moreover, the Kraus model provides a precise calculation of fractality in the fat crystal network as compared to the 2D image analysis. According to this result, the 3 dimension fat crystal network is formed for pure CB, and which leads to a quasi-two-dimensional fat crystal network with increasing CO concentration, as shown in Figure 56. Similarly, the Avrami exponent (*n*) shows the crystal growth mechanism where, the value is higher for CB and decreases with increasing CO concentration in range of needle-like morphology. Therefore, the correlation between the microstructure aspect with

Avrami exponent (*n*) and fractal dimension (d_f) is achieved. This will ultimately help to understand the connection between mouthfeel and fractality in the future.

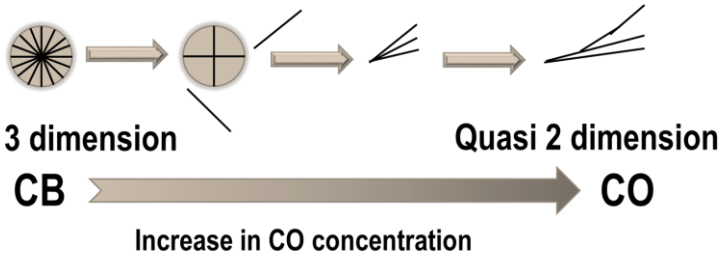

Figure 56: The schematic representing the shift of 3 dimensions to quasi 2 dimensions as the concentration CO increases in CB/CO blends.

Section 4: Effect of paraffin wax derivatives on the crystallization of $E_{CB\text{-}CO}$

This section focuses on the effect of different concentrations of paraffin wax derivatives (C (20), C (25), and C (30)) on the crystallization of $E_{CB\text{-}CO}$ in terms of micro and macroscopic behavior. Based on these results further analysis on thermal, morphological behavior of 1wt % of n-alkanes addition to the $E_{CB\text{-}CO}$ along with pure CB and CO is analyzed. According to the thermal analysis, the ternary state diagram is plotted for C (20), C (25), and C (30) in addition to the CB and CO. Moreover, crystallization kinetics and rheological properties are also examined.

4.1 Selection rule for further analysis

This section illustrates the initial experimental results, which contributed to set the path for the current study. Initially, 1, 2, 3, and 5 wt% of C (20), C (25), and C (30) were added to $E_{CB\text{-}CO}$ for understanding the effect of different concentrations of n-alkanes on crystallization in terms of crystal morphology. The microscopy results (Figure 57 (a)) show that after the addition of 1 wt% of C (20), the random aggregation of the small needlelike structure takes place. Further addition of 2, 3, and 5 wt% of C (20) indicates that these random aggregations of needle-like structures form spherulitic morphology. At this stage, the results depict that a larger percentage of C (20) results in a lower number of crystals with large and defined crystal sizes and shapes. Similar results are observed in the case of 1 and 2 wt % of C (25), however, the 'fiber or rod-like' morphology (indicated with red arrow) is observed for 3 and 5 wt% of C (25) along with small spherulitic structure formation. Further, the addition of 1 wt% of C (30) reveals that small crystals granules are situated at the surface of 'fiber-like' structures. While, more addition of C (30) from 2 to 5 wt%, resulted in the formation of 'fiber-like' to vague (unspecific) morphological structures respectively. The evidence from this primary study implies that two separate types of morphologies form in the case of 3 and 5 wt% of C (25) and for all concentrations of C (30) addition to $E_{CB\text{-}CO}$. Additionally, the effect on bulk samples of pure $E_{CB\text{-}CO}$ and its comparison with addition of 1, 2, 3, and 5 wt% of C (20), C (25), and C (30) reveal that, after 24 h at 22 °C, the samples with addition of C (20) crystallize as a thin layer on the surface of a liquid part. Similarly, a thin layer of crystals due to 1 and 2 wt% of C (25) is visible (Figure 57 (b)), whereas, the samples with 3 and 5 wt% of C (25) represent opaque

mixture instead of transparent (as pure $E_{CB\text{-}CO}$ and samples with all concentrations of C (20), which are in transparent liquid state), which is the effect of crystallization of samples. Furthermore, the inverted position of these two glass bottles does not allow the liquid portion to flow by gravity. Similarly, in the case of C (30) addition to $E_{CB\text{-}CO}$, all the samples show crystallization, however, only, 2, 3, and 5 wt% of C (30) show the effect of holding the liquid fraction of $E_{CB\text{-}CO}$ against the pull of gravity. Therefore, micro and macroscopic point of view affirm that a large quantity of $E_{CB\text{-}CO}$ likes to stay in the liquid state at 22 °C after 24 h, while, crystals of 3 and 5 wt% of C (25) and 2, 3 and 5 wt% of C (30), act as a network, which entraps the liquid fraction of $E_{CB\text{-}CO}$. This behavior resembles 'oleogel-like' properties. An oleogel can be defined as an organic liquid entrapped within a thermoreversible three-dimensional gel network. This network is either to be formed by polymers or low molecular weight organo gelators (LMOGs) [105]. In this study instead of only liquid fraction entrapment in three-dimensional networks of LMOGs, the solid and liquid fraction of $E_{CB\text{-}CO}$ entrapped within a colloidal network of C (25) and C (30) with the strength sufficient to immobilize the liquids against the pull of gravity [106]. The 'oleogel-like' behavior is possible to visualize for 5 wt% of C (25) and C (30) addition respectively (Figure 57 (c)). Inset microscopic images represent the morphological view of a respective gel-like structure.

To further proceed towards understanding the effect on $E_{CB\text{-}CO}$, parallel experiments were performed on pure CB and CO. As similar to $E_{CB\text{-}CO}$, phase separation is observed in case of 2, 3, and 5 wt% of C (30) in CB, along with showing 'gel-like' network of long rods entrapping crystals of CB in between. As shown in Appendix Figure 71 (a), the microscopy image for 2 wt% of C (30) addition, the red line represents the continuous network of C (30) crystals in which small granulitic crystals of CB at the surface of these rods as well as the space in between are entrapped. Hence, the microstructural view provides a resemblance to an oleogel like structure.

Similar to $E_{CB\text{-}CO}$, the macroscopic view of glass bottles with the samples of pure CO and its comparison with 1, 2, 3, and 5 wt% of C (25) and C (30) are shown in Figure S2 (b). As CO tends to crystallize after 24 h, the behavior of the 'oleogel-like' property was observed after 1 h and 24 h. After comparison with pure CO, the samples with 2, 3, and 5 wt% of C (25) and all samples with C (30), after 1 h, demonstrate the opaque mixture as compared to the transparent liquid part of CO. The tendency to behave as an 'oleogel-like' structure can be confirmed by inverting the glass bottles of 3 and 5 wt% of C (25) and C (30) (Appendix Figure 71 (b)).

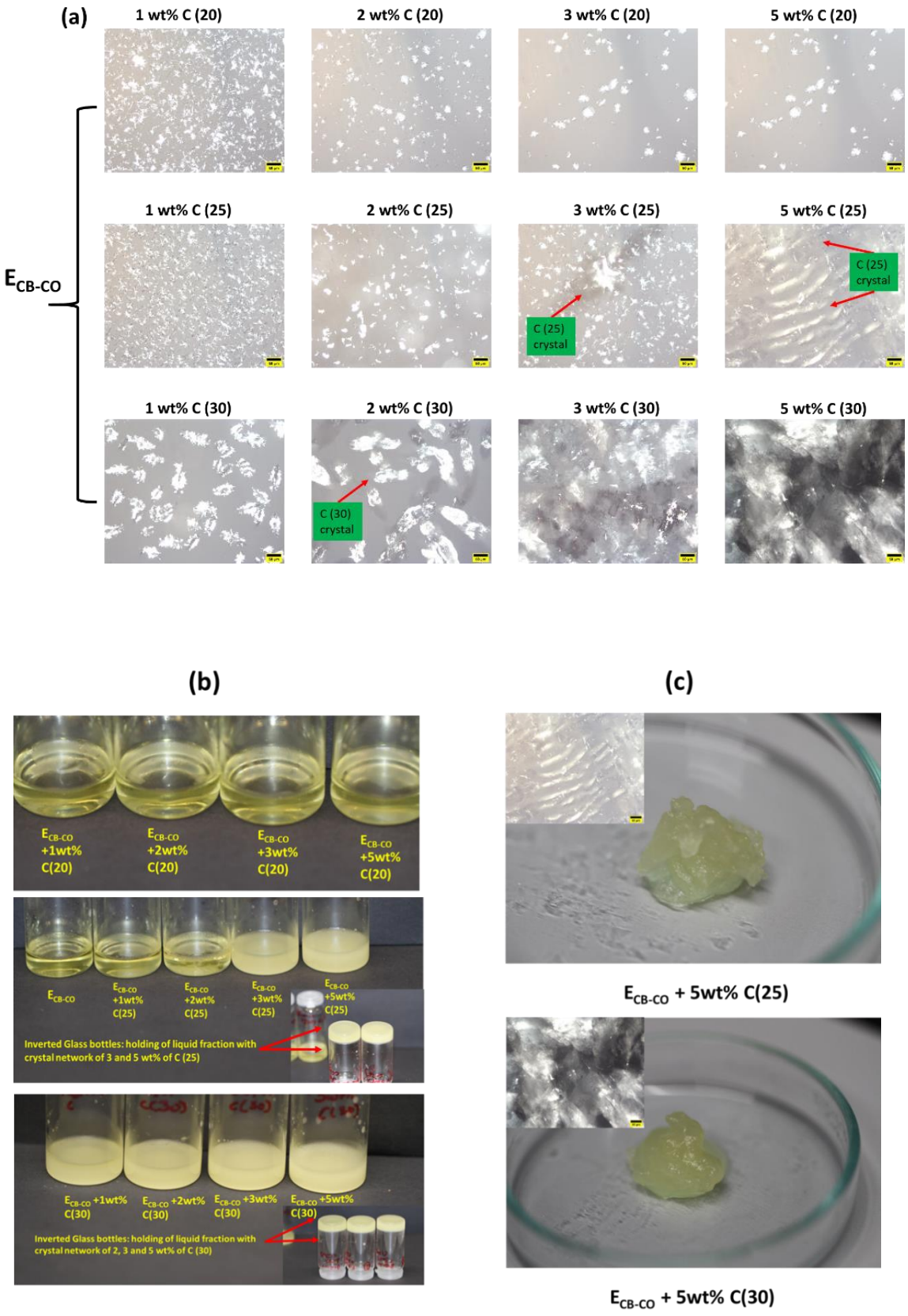

Figure 57: (a): Microscopic representation of changes in morphology with respect to the addition of 1, 2, 3, and 5 wt% of C (20), C (25), and C (30) in E_{CB-CO}. 3 and 5 wt% of C (25) and all C (30) addition shows two different morphologies, which is shown with a red arrow. The

scale bar represents 50 µm. (b) The glass bottles represent the macroscopic view of pure $E_{CB\text{-}CO}$ and its comparison with 1, 2, 3, and 5 wt% of C (20), C (25), and C (30) addition after 24 h at 22 °C. The inset reveals that inversion of glass bottles for 3 and 5 wt% of C (25) and 2, 3, and 5 wt% of C (30) sample, holds the liquid fraction of $E_{CB\text{-}CO}$. This indicates oleogel-like property. (c) An example of 'oleogel-like' property after addition of 5 wt% of C (25) and C (30). Inset represents the microscopic view of gels.

The comparison with the microscopy images depicts that, after 1 h, the C (25) crystallizes (unspecified or vague morphology) and entraps the liquid oil. Whereas, after 24 h, the needle-like morphology from CO crystals appears (Appendix Figure 71 (c)). The reason for such specific behavior after 1 h could be because, CO is in the liquid state, while, a network of C (25) behaves as isotropic in nature, and hence partially polarized micrographs are detected. Therefore, the difference between liquid domains and C (25) crystals is hard to detect in the case of samples with 3 and 5 wt% C (25) addition. However, in the case of C (30) addition to CO, the network formed by C (30) crystals inhibits the long needlelike growth of CO crystals, by restricting the phase space. Therefore, the current study observation depicts that, due to the aggregation of needles, small spherulitic crystals are formed instead of long needles. This suggests that as the length of C (30) is higher, the stronger connectivity of C (30) crystals to be achieved, and hence, entrapped CO cannot be crystallized in the long needle-like structure due to C (30) crystal barrier. Thus, the micro and macroscopic observation provide a hint towards the formation of 'oleogel-like' behavior.

Therefore, according to these initial observations, phase separation occurs at a higher percentage of C (25) and C (30) in all mixtures of CB, CO, and $E_{CB\text{-}CO}$. The possible reason for these phase separations at a higher percentage would be that the center to center distance of one to another molecule of C (25) and C (30) decreases as the concentration increases, which eventually leads to fast segregation of 'like' molecules and thus the solidification of n-alkanes takes place earlier and separated from rest of liquid and solid fraction. Also, n-alkanes likely provoke a "selective crystallization" of saturated fats. Hence, to avoid the effect of phase separation, in the further study, only the effect of 1 wt% of C (20), C (25), and C (30) on the crystallization of $E_{CB\text{-}CO}$, CB, and CO in terms of the effect on thermal, morphological and the mechanism for the variations in these properties is further understood.

4.2 Thermal behavior

a) Effect of n-alkanes on E_{CB-CO}:

After keeping the samples for 24 h at 22 °C the thermal behavior of E_{CB-CO} with n-alkanes was analyzed by using DSC. In the case of the 1st melting process, no specific thermogram is observed, hence only crystallization and re-melting behavior are shown in Figure 58 (a). Each color represents a different mixture of E_{CB-CO} with n-alkanes, which are compared with the control sample (pure E_{CB-CO}). During crystallization, for 1 wt% of C (20) and C (25), the onset temperature, as well as the main exothermic peak, has shifted to a higher temperature (peak ~ 8 °C) as compared to pure E_{CB-CO} (peak ~ 4 °C). Whereas in the case of 1 wt% of C (30), two exothermic peaks appeared, one at ~ 30 °C and followed by a second at ~ 10 °C. The exothermic peak at 30 °C represents the crystallization of C (30) when compared to the DSC patterns of pure n-alkanes (Appendix Figure 72). These two different exothermic peaks represent that a mixture of 1 wt% C (30) with E_{CB-CO} displayed phase separation in solid-state. Moreover, these results also propose that high melting fractions (HMF) of eutectic mixtures (from CB or CO) interact or co-crystallize with n-alkanes and hence tend to crystallize at the higher temperature. After crystallization to -50 °C, the melting process was implemented to observe the variations in melting behavior after the addition of n-alkanes to the eutectic mixture. This result illustrates that for all the mixtures, the melting temperature is increased with respect to the eutectic mixture, however, no significant change is observed for three different alkyl chain lengths. These results confirm that the addition of 1 wt% of C (20) and C (25) shows an increase in crystallization temperature with no phase separation, whereas, phase separation occurred at 1 wt% of C (30) in the solid-state.

As the result shows a significant change in the thermal behavior of E_{CB-CO}, but it is difficult to predict specific reasons behind it, hence, in further experiments, 1 wt% of n-alkanes were mixed with CB and CO and their analysis is explained in sections a and b below. These sets of experiments led us to understand the interactions of pure components with different chain length n-alkanes and thus the behavioral changes.

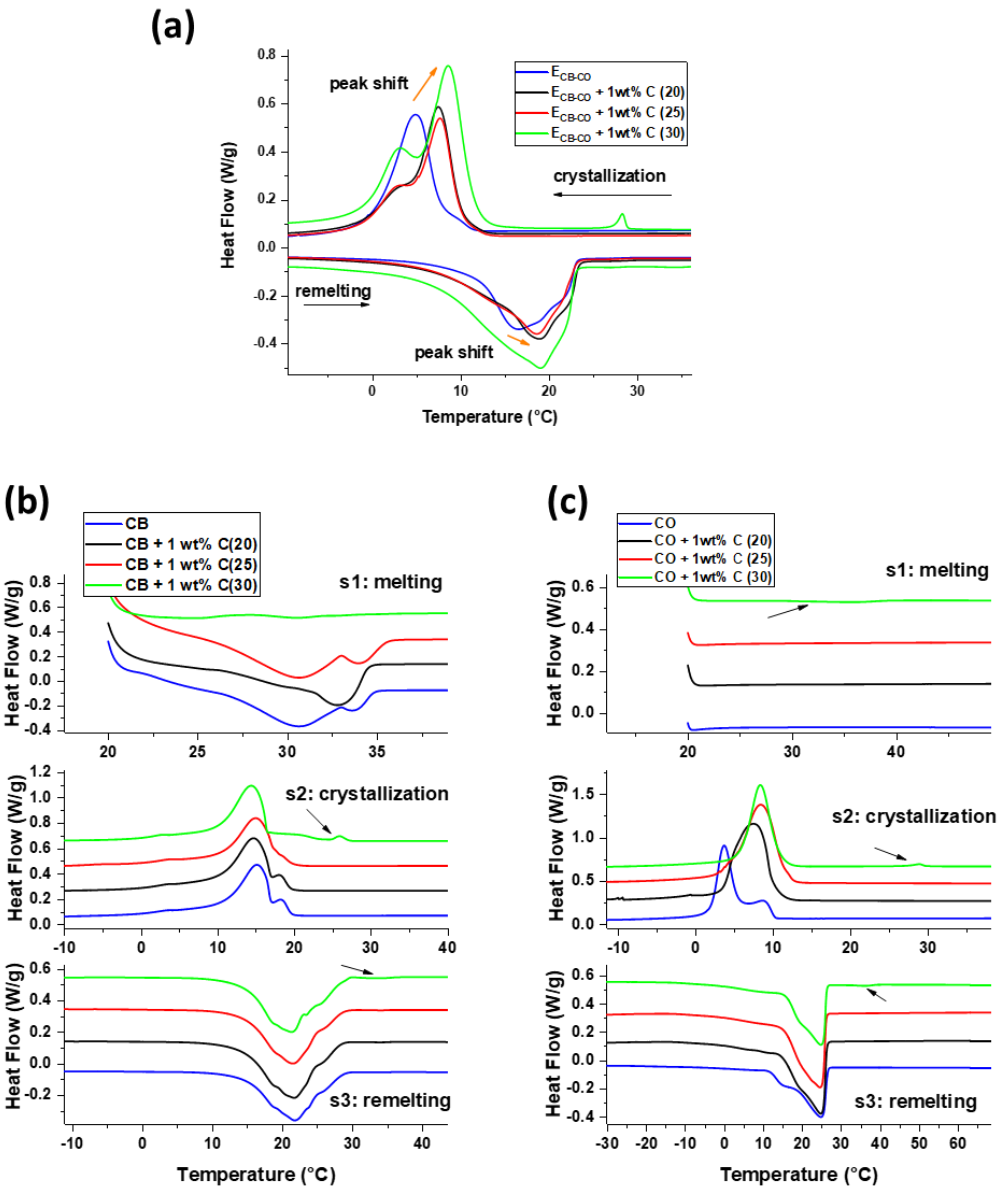

Figure 58: (a) DSC thermogram of the effect of n-alkanes on (a) crystallization and re-melting process of $E_{CB\text{-}CO}$ (b) melting, crystallization, and re-melting of CB and (c) CO. Their comparison with a thermal property of $E_{CB\text{-}CO}$, pure CB, and CO respectively. The orange arrow in (a) depicts the shift of exotherm and endotherm of $E_{CB\text{-}CO}$ after the addition of 1 wt% of n-alkanes to a higher temperature. In figure (b) and (c) the exotherm and endotherm peak of C (30) crystal is indicated by a black arrow.

b) Effect of n-alkanes on CB:

The thermal behavior of CB with three different segments is shown in Figure 58 (b). Each color represents a different set of blends with n-alkane (black, red and green) and their

comparison with pure CB (blue line). After 24 h at 22 °C, DSC was performed for each different additives and their melting segment was plotted as segment 1 (s1). In the case of pure CB, two endothermic peaks are detected during the melting process, which can be ascribed to the melting of two polymorphs, Form IV (30.85 °C) and Form V (33.6 °C) [35]. After the addition of 1 wt% of C (20), one sharp peak is obtained at ~ 33 °C (Form V), which suggests the formation of only one polymorph as compared to pure CB. However, samples of 1 wt% of C (25) do not show any significant difference in the melting pattern. While after the addition of 1 wt% C (30) a very small melting peak is detected.

The next segment (Figure 58 (b) s2) was designed to observe the effect of dynamic crystallization on the individual fat and their respective blends. A controlled cooling process was achieved in this segment that led to the formation of crystal forms that are different from those formed during the 24 h isothermal crystallization process. As explained in the current previous study [107], pure CB crystallized according to the composition of TAGs present in the CB. The co-crystallization of the HMF, a medium melting fraction (MMF), and a low melting fraction (LMF) took place. For the addition of 1wt% of C (20) and C (25), there is no specific change in peak temperature detected, whereas, for 1wt% of C (30), two exothermic peaks appeared, one at ~ 26 °C and another at ~ 14 °C. By comparing this exotherm with pure CB and thermogram of pure n-alkane (Appendix Figure 72), the peak at 26 °C represents the crystals of C (30), whereas the peak at 14 °C detected is for CB crystals. Another observation is that HMF peak at 1 wt% C (25) and C (30) is diminishing as compared to pure CB, which can suggest that the HMF of CB interacted with C (25) and C (30), however, a similar phenomenon is not observed for 1wt% C (20). After the crystallization process, the re-melting process is shown in Figure 58 (b) s3. Unfortunately, after the addition of n-alkanes to CB, it does not show any specific change in melting temperature with respect to chain length. Thus, this result highlights that there is an effective change in the crystallization of CB after the addition of 1 wt% of C (20) during isothermal crystallization (segment 1) as compared to dynamic crystallization (segment 3). Moreover, a phase separation at solid state in case of 1 wt% addition of C (30) emerged, similar to a eutectic mixture (Figure 58 (a)). On the other hand, no evidence of an increase in melting temperature with respect to the addition of n-alkanes is observed.

c) Effect of n-alkanes on CO:

In Figure 58 (c), three segments of melting, crystallization, and re-melting for 1 wt % of n-alkanes in CO with respect to pure CO are shown. Each different color represents 1 wt% of C

(20), C (25), and C (30) respectively. In case of CO, after 24 h, the crystals are formed however, due to the handling process it is already in molten form before the start of the measurement, hence no endothermic peak is detected except for 1 wt% C (30). The small endothermic peak is detected at ~ 36 °C. This peak represents the melting temperature of 1 wt% C (30). The next segment shows the crystallization of these blends with a rate of 2 K/min. For pure CO, two crystallization exotherms are detected, in which, one is a sharp peak at a lower temperature (~ 2.5 °C) and the second overlapping shoulder peak at a higher temperature (~ 7.4 °C). After the addition of 1 wt% of C (20), the peak temperature is shifted to ~ 8 °C. Similarly, after the addition of 1 wt% C (25), the peak shifted more to the higher temperature, which suggests that higher carbon chain length enhances the crystallization in pure CO. However, in the case of 1 wt% C (30), the peak temperature is not further shifted towards higher temperature, rather, another small exothermic peak is detected at ~ 28 °C. Altogether, this result proposes that the addition of long-chain hydrocarbon helped to increase in crystallization temperature of CO along with phase separation. A similar result is obtained during the crystallization process for $E_{CB\text{-}CO}$.

During the re-melting process, CO shows two peaks, one main peak at ~ 24 °C and another shoulder peak at ~ 14 °C, which reflects the melting of HMF and LMF respectively. After the addition of 1 wt% of C (20) (red curve), the peak temperature is not changed, however, the shoulder peak at 14°C disappeared. This endotherm is in accordance with the exotherm profile in Figure 58 (c) s2 of the same blend as it tends to crystallize as a single peak. This suggests that the addition of n-alkane helped to prevent the co-crystallization process in the case of CO by providing the necessary surface “seed” to crystallize as a one-crystal form. A similar effect of vanishing shoulder of melting peak is observed after addition of 1 wt% of C (25) and C (30). Likewise, it has been found in a study that after addition of 1 wt% of low HLB sucrose esters to coconut oil resulted in minor changes in melting temperature with no influence on polymorphic occurrence [108]. Thus, these results offer compelling evidence for the hypothesis that the interaction of CO with derivatives of n-alkanes is more pronounced and hence, the effect on the eutectic mixture is distinct.

The results of the DSC experiments indicate that the crystallization and melting temperature of the eutectic mixture increase after the addition of all the derivatives of n-alkanes. Further analysis confirms that the interaction of CO with n-alkanes induces such behavior due to the attractive interaction of CO with n-alkanes. Although the reason for fast crystallization has been discussed, the question remains, what interactions have occurred between CO and n-alkanes crystals for inducing the crystallization process. To put further steps

towards understanding the crystallization process, the following hypothesis is necessary to be considered: The crystal structure of n-alkanes and their compatibility with the crystal structure of CB and CO results in non-favorable and favorable interactions respectively. To explain in detail firstly the mechanism for the formation of eutectic mixture needs to be understood, which is also explained earlier in section 3.

The formation of a stable crystallization nucleus requires total overcome a certain (free) energy barrier determined by the balance of volume and surface energy. As can be seen from the preliminary experiments, the formation of nuclei and the crystallization of CO initiates from the edges of the vessels or microscope slides and progresses to the center.

A) Due to the structural differences between TAGs of CB (monounsaturated TAGs), the attachment of these TAGs to the short-chained saturated TAGs increases the total free energy. On the contrary, the detachment of CB crystal from CO crystals reduces the free energy to the states of higher preference.

B) Another aspect arises from the supercooling as the crystallization temperature is 22 °C (CT), which is close to the melting temperatures of CB and CO. The CB and CO crystals have an ample amount of time to arrange the best possible lamella having stable 3D nuclei with the least amount of free energy and surface energy. Therefore, the demixing of CB and CO could take place except for the crystals formed at eutectic mixture composition.

To further elaborate this hypothesis with respect to the addition of n-alkanes in $E_{CB\text{-}CO}$, the concept of a) epitaxial growth b) heterogeneous nucleation can be taken into account. Already formed crystals of n-alkanes act as a 'template' for the initiation of CO crystallization. The strong van der Waals attractive forces between template molecule and CO depends on the orientation and conformation of crystal nature. According to the previous studies, the crystal formation of n-alkanes differs with respect to the chain length and evenness (in the number of carbon atoms), pure n-alkanes crystallize in monoclinic (even carbon $n > 26$), triclinic (even carbon $n < 26$) or depending on temperature odd n-alkanes crystallize in an orthorhombic or pseudo-hexagonal structure [18]. Here, C (20) and C (25) derivatives are even and odd chain length having less carbon atom than 26 respectively hence, tend to crystallize in triclinic and in an orthorhombic or pseudo-hexagonal for C (25) respectively. Similarly, the polymorphic formation of CO and CB tends to form typically hexagonal, orthorhombic, and triclinic crystal structures depending on process conditions [15]. Hence, when the triclinic crystal structure of C (20) is mixed with $E_{CB\text{-}CO}$ and in CO individually, the crystallization temperature increases due to the epitaxial growth mechanism [109]. With the similarity in crystal orientation and

chain length of CO and C (20) and C (25), the lamellar distance and subcell packing become similar which ultimately tend to appear attractive forces. Due to similar subcell packing the interfacial energy becomes less and so the activation energy for nucleation of CO decreases. Whereas in the case of the addition of C (30), the monoclinic crystal structure tends to occur which exhibits dissimilar behavior with the crystal structure from TAGs of CO. Due to these differences in the crystal structure, the phase separation between CO and C (30) crystals occurs. Although there appears a phase separation in polymorphic form these crystals from C (30) act as nucleation sites (heterogeneous nucleation process) for rest of liquid fraction and hence an increase in crystallization temperature is observed. In contrast to the effect on CO crystallization, the effects on CB crystallization is hardly noticeable. The reason could be that even though the similarities in crystal structure from C (20) and C (25) to CB crystals, the lamellar spacings increased due to the presence of a double bond in the oleic acid. Due to this behavior, only HMF from CB (this fraction contains mainly saturated TAGs) show attractive forces with triclinic or orthorhombic crystal structure and hence the disappearance of shoulder peak from Figure 58 (b) (crystallization segment) is observed. Whereas, in case of C (30) addition again due to dissimilarities between crystal orientation (monoclinic of C (30) and CB crystals (Form I (hexagonal)) and lamella spacings (due to double bond), the phase separation occurs.

4.3 Ternary plot: Liquidus temperature projections

It is useful to construct a ternary diagram with liquidus melting temperature projections in order to understand the possible forecast of the melting temperature profile of the ternary system with respect to the chain length of n-alkanes. To elaborate this in more detail, the ternary temperature profile is plotted by considering the melting temperatures (s3: re-melting segment in Figure 58) of mixtures: one ternary mixture of CB, CO, and n-alkanes ($E_{CB\text{-}CO}$ + 1wt% n-alkanes), 2 binary mixtures of CB and CO with n-alkanes (CB and CO + 1wt% n-alkanes) and the melting temperatures of liquidus line of 12 binary mixtures of CB/CO blends from section 3 (shown the graph in Figure 59 (d)) and the melting temperature of individual components. Figure 59 (a), (b), and (c) represent the ternary temperature profile diagram with the specific indications of contours having least temperature (blue region) to highest possible temperature (red region) for further mixtures of ternary components of C (20), C (25) and C (30) addition

to CB and CO respectively. The three sides of triangles represent the weight fraction of the individual components, as indicated with the increasing concentration arrow. Different color profiles are separated by boundary lines displayed with dashed black lines. The respective temperature limits for each boundary line are shown on the vertical bar next to the ternary diagram. The filled gray circle on each boundary line belongs to the point with a specific concentration of ternary mixture and only the fractions of respective n-alkanes in the mixture are shown as black text. For instance, the ternary mixture for the 1st point in Figure 59 (a) indicates (weight fraction of C (20)) $X_{C(20)} = 0.01$, then the 2nd point indicates $X_{C(20)} = 0.15$, and so on. The data points from the current experiments are shown as yellow squares. Based on these data points the possible forecast of a ternary temperature state diagram for all concentrations is possible to make. In the case of the C (30) ternary diagram (Figure 58 (c)), the superimposition of the two plots is shown. As DSC profiles of C (30) addition to $E_{CB\text{-}CO}$, pure CB, and CO show two melting peaks, the solid line represents the possible forecast obtained by considering the melting temperature of C (30). In all three diagrams, dark blue indicates the least melting temperature for ternary blends of CB, CO, and n-alkanes. The ternary mixture of C (20) and CB-CO indicates the formation of a eutectic phase with a range from X_{CO} = ~0.37 to 0.70 with up to $X_{C(20)}$ = ~0.05. Moreover, the light blue contour in the case of C (20) addition also shows the eutectic phase with an increased concentration range of CO from ~0.22 to 0.75 with up to ~0.15 of C (20). For further concentrations of C (20), the green region estimates the elevation in melting temperature of the ternary mixture. Similarly for a higher concentration of CO and/or CB with less amount of C (20) will increase the melting temperature of the ternary mixture. As the concentration of C (20) further increases, the melting temperature will increase as expected. On the other hand, in the case of C (25), the ternary eutectic forms the range from ~0.37 to 0.75 of CO and up to ~0.08 of C (25). Although the prediction represents the eutectic mixture with such a high percentage of C (25), the predictions are in contradiction with the DSC and initial microscopy result as it tends to phase separate above 2wt% for C (25). For the further concentration of C (25), the melting temperature of the ternary phase is increasing with the effect of phase separation. In case of the ternary plot for C (30), the dashed line and solid line plot suggest that the ternary eutectic forms with the range from ~0.37 to 0.75 of CO and ~0.37 to 0.55 of CO up to the ~0.10 of C (30) respectively. For further concentrations, the dashed line plot represents the similar predictions as C (25) ternary plot, whereas, solid line estimates imply that in the range of ~0.55 to 0.75 of CO, the least melting temperature has predicted as compared to the other compositions on that boundary line.

From these ternary plots, a similar trend for C (25) and C (30) addition is predicted, due to higher chain length than CB and CO as well as a large difference in melting temperature of CB and CO, whereas, the eutectic with a higher concentration of C (20) is possible due to fewer differences in melting temperature and with chain length. Hence, irrespective of chain length with 1 wt% of n-alkanes addition to $E_{CB\text{-}CO}$ does not show any significant change in melting temperature but with higher percentage may increase the melting temperature up to ~22°C with a consequence of phase separation in case of C (25) and C (30).

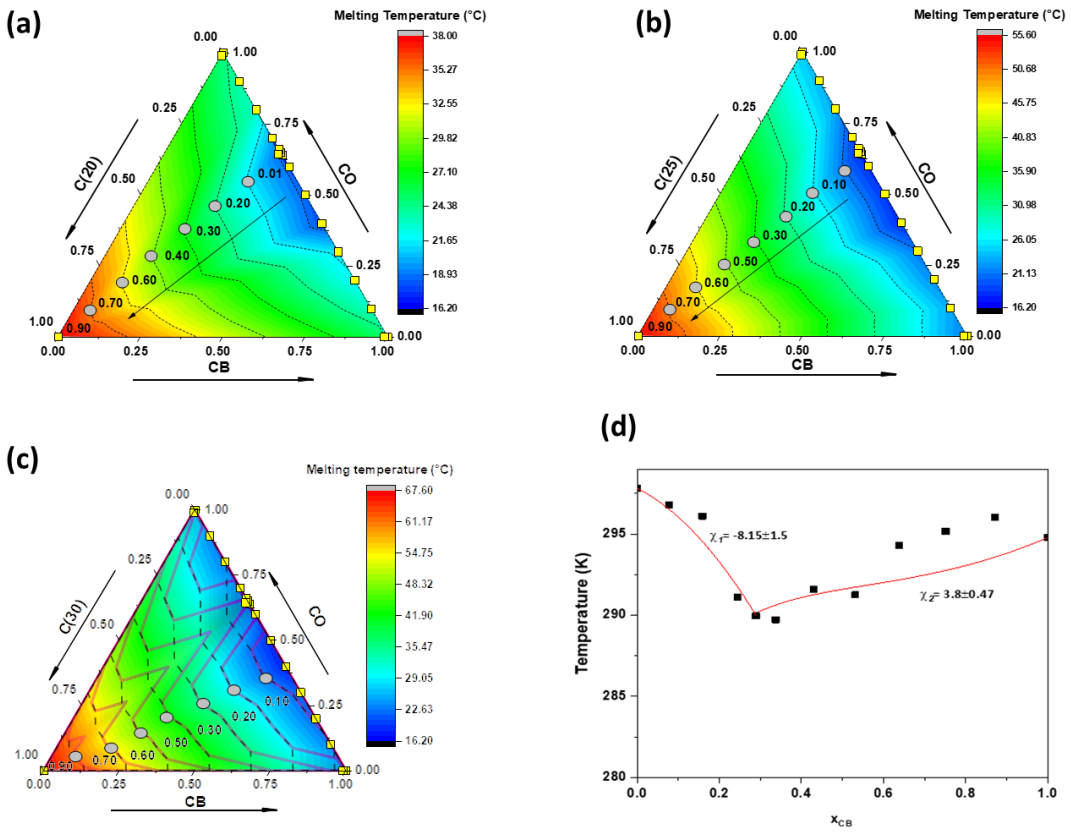

Figure 59: Ternary plot with melting temperature projections with respect to the concentrations (a) C (20)-CB-CO (b) C (25)-CB-CO (c) C (30)-CB-CO ternary plot. The sidebar represents the change in temperature with respect to the color. Yellow square symbols indicate measured data points and filled gray circles on boundary lines are representing the concentration of n-alkanes on that position to understand the effect of chain length concentration on the melting temperature of ternary mixtures. In the case of the C (30) ternary plot, the superimposition of predication n from two different melting points from DSC results is shown. Solid line predictions belong to C (30) melting points and a dashed line indicates the main peak temperature (CB, CO, and $E_{CB\text{-}CO}$). (d) The liquidus line for CB/CO blends is plotted based on DSC results from a previous study [107].

4.4 Crystal morphology

The crystal morphology of n-alkanes addition to E_{CB-CO} blends was captured by PLM. Figure 60 (a) shows the morphology of 1 wt% of C (20), C (25), and C (30) to E_{CB-CO} after 24 h at 22 °C and after heating this sample to 90 °C and cooled down to 10 °C with 2 K/minute rate. The pictures captured after 24 h at 22 °C, display the crystal formation after the isothermal crystallization process. Hence one can understand the morphology of crystals, which are melted during the DSC melting segment. Although the crystallinity of eutectic mixture and n-alkanes are visible in microscopy, the DSC could not measure endotherm for these small crystals hence, this result is not shown in Figure 55. According to images, after the addition of 1 wt% of C (20), C (25), and C (30), aggregation of small needle-like morphology is observed. Moreover, the crystallinity is increased as compared to E_{CB-CO}, which is studied in the previous work [107]. While in the case of dynamic crystallization, the granular structure is formed in all blends. Similar to DSC, a morphological study is also performed on CB and CO, to understand the effect of carbon chain length on morphology. In Figure 60 (b), the crystal morphology of 1 wt% of C (20), C (25), and C (30) to CB after 24 h at 22 °C and after heating this sample to 90 °C and cooled down to 10 °C with 2 K/min rate is shown respectively. These images after 24 h detected spherulitic morphology for 1 wt% of C (20), whereas, granulated structures are observed for 1 wt% of C (25). While in the case of 1 wt% of C (30), randomly shaped aggregates of small crystallites are formed. After heating at 90 °C and cooling down to 10 °C, the formation of crystal morphology shows the visualization of the crystallization process from DSC (Figure 58 (b) s2). At 10 °C, in all blends, small granulites are observed, which is similar to morphological behavior observed in pure CB [107].

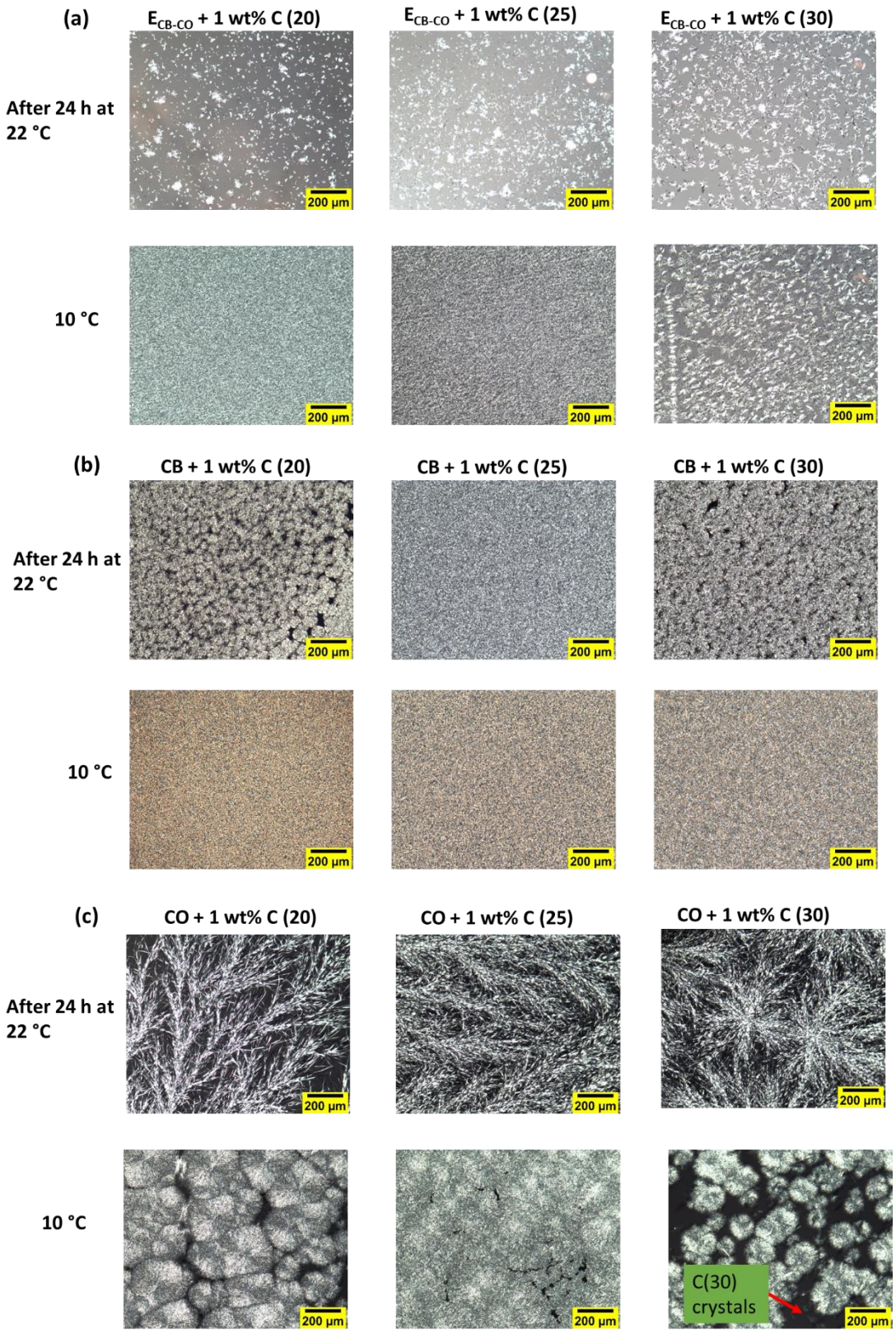

Figure 60: Microscopic representation of changes in morphology with respect to the addition of 1 wt% of C (20), C (25) and C (30) in (a) E_{CB-CO} (b) CB and (c) CO after 24 h at 22 °C (showing

results of isothermal crystallization) and at 10 °C after dynamic crystallization process. The scale bar represents 200 µm.

Similar experiments were performed on CO, Figure 60 (c) shows the images captured after 24 h at 22 °C and crystal morphology after dynamic crystallization at 10 °C. The needle-like morphology is observed after 24 h in all cases of the addition of n-alkanes, whereas, for 1 wt% of C (20) and C (25), small spherulites from an aggregation of needle-shaped crystals are formed and grew until their surface-merge. Similar phenomena occurred in the case of 1 wt% of C (30) for crystal growth however, there is a hint of another crystal form (rod-like) which is marked with a red arrow in the figure. According to crystal morphology from pure n-alkanes (Appendix Figure 73), this rod-like morphology represents the crystals of C (30). Therefore, these two different forms of crystal structure represent the phase separation, which is in good agreement with DSC results. Accordingly, the result demonstrates that, although the addition of 1 wt% of n-alkanes in $E_{CB\text{-}CO}$ does not influence the crystal morphology a lot, the increase in crystallites after 24 h leads to a hypothesis of increasing solid fat content. Similar results were observed in the case of 1 wt% of sucrose esters in CO showed no effect on polymorphism and morphology but crystallization kinetics [110]. Hence, to verify this theory, SFC was calculated based on ^{1}H solid-state NMR experiments.

4.5 Effect of n-alkanes on crystallization kinetics

To understand the effect of n-alkanes addition to $E_{CB\text{-}CO}$ and CB, CO on the solid fat content (SFC (%)), isothermal crystallization kinetics is studied. Figure 61 (a), (b), and (c) show the graph between the relation of SFC after addition of C (20), C (25), and C (30) on pure $E_{CB\text{-}CO}$ and CB, CO respectively. The blue graph represents the control samples for three different mixtures. The insets show the magnification at early times of the crystallization kinetics from the original graph. According to Figure 61 (a), after the addition of three different n-alkanes to $E_{CB\text{-}CO}$, the SFC value is increased to ~ 7 % from ~ 5 % (control sample). No significant influence of carbon chain length on final SFC is detected. Moreover, the magnifying view reveals that in the case of 1 wt% of C (20) and C (25) addition, the crystal growth occurs similar to $E_{CB\text{-}CO}$, while in the case of 1 wt% of C (30), the time required for crystal growth is faster than the other blends. To understand in detail the effect on $E_{CB\text{-}CO}$, similar experiments were carried out on CB and CO. According to Figure 61 (b), the SFC profile was is influenced with

respect to chain length as well as a pure CB profile. The SFC value after 24 h for all the blends also shows a similar value (~ 70 %). This result suggests that the SFC value of CB, is not affected by a small number of n-alkanes and therefore the thermal behavior is less likely affected. In contrast with the results for CB, the addition of n-alkanes to CO (Figure 61 (c)) shows a significant change in crystallization kinetics, however, the SFC value after 24 h hardly differs (~ 22%). As per the magnifying view, the crystal growth for 1 wt% of C (20) and C (25) is delayed as compared to pure CO, whereas, in the case of 1 wt% of C (30) the crystal growth is promoted. A similar conclusion is reached by studies of the addition of diacylglycerol as a minor component to anhydrous milk fat showing the delay in onset of crystallization at low degrees of supercooling [111]. The possible reason for the prohibition of nucleation with C (20) and C (25) is to promote dense crystal lamella which would lead to thermodynamically stable nuclei due to similarities in molecular structures of CO and C (20) and C (25). Therefore, in the case of DSC results the crystallization temperature increased. Altogether, the crystallization kinetics profile provides the reason for the change in thermal behavior after the addition of n-alkanes to pure CO.

Similar to DSC results, SFC profiles for all the samples depict that, in the case of a eutectic mixture, the effect is prominent after the addition of n-alkanes due to pronounce interaction between CO with n-alkanes as compared to CB. For more understanding of crystallization kinetics, all the profiles were fitted with the Avrami equation (Appendix Figure 74). After fitting this equation, *k* (Avrami constant) and *n* (exponent) were acquired (a fitting example is shown in the figure). In Figure 61 (d), the relation of *k* with respect to the chain length of n-alkanes is shown. Avrami constant (*k*) for 1 wt% of C (20) and C (25) obtained a similar value as $E_{CB\text{-}CO}$, which reflects that there is no specific variation in nucleation and crystal growth, however, the sharply increased value for 1 wt% of C (30) represents an increase in crystallization rate due to seed crystals of C (30). Similar behavior is obtained for 1 wt% of n-alkanes in CO. The phase separation due to the addition of C (30) is strongly detected by a sharp increase in *k* value. These results are in agreement with the study of the addition of different amounts of candelilla wax (CLW) and rice bran wax (RW) in palm kernel stearin (PKS-85), the SFC content at 20 °C and 4 °C after 24 h have not significantly changed, however, exhibited a higher value of *k* at 20 °C for the addition of CLW implying promoting crystallization of PKS-85 [48].

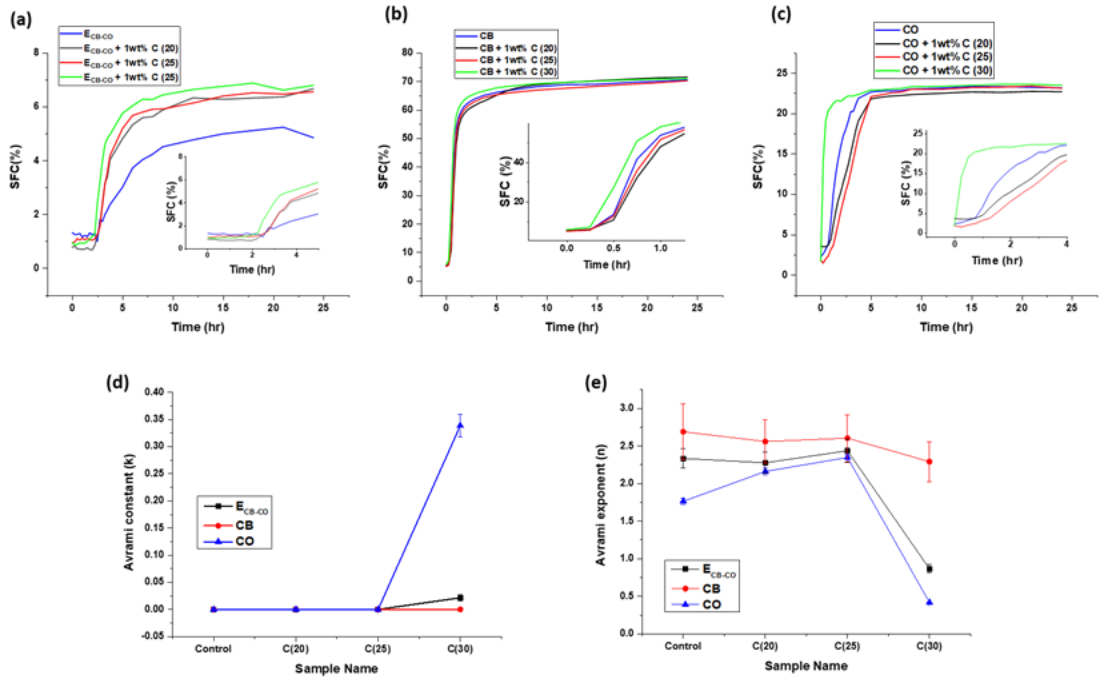

Figure 61: Effect on solid fat content (SFC) profile for the addition of 1 wt% of C (20), C (25), and C (30) in (a) $E_{CB\text{-}CO}$, (b) CB and (c) CO respectively. The insider graph represents the magnifying view of the start of the crystallization process. (d) And (e) denotes Avrami constant (k) and exponent (n) change after 1 wt% of n-alkanes. Control represents pure $E_{CB\text{-}CO}$, CB, and CO.

Further, In the case of CB blends, no specific effect on *k* value was observed after the addition of 1wt % of C (20) and C (25) as compared to pure CB, because of alike SFC profile as shown in Figure 61 (b)(magnified view). The reason for such behavior could be that a small number of n-alkanes (specifically C (20) and C (25)) acted as a part of the CB system and hence no specific change occurred. Whereas, after the addition of 1 wt% C (30) to CB, the crystallization process is promoted as per magnified view but the (*k*) value is hardly varied.

The Avrami exponent, *n*, originally meant to reflect the crystal growth geometry, provides kind of evidence about nucleation and growth mechanism [21], [23]. The phenomenological Avrami equation addresses the crystal growth as a combination of the function of the time dependence of nucleation and the number of dimensions in which growth takes place. Nucleation is either instantaneous, with all nuclei appearing at once, or sporadic, with the number of nuclei increasing linearly with time. Crystal growth could be either spherical, plate-like, or needle-like in three, two, or one dimension respectively. Ideally, the exponent value is an integer, however, in most experiments, fractional values are observed, due to the simultaneous

development of more than one type of crystal. In this study, fractional values are obtained after fitting the equation, which explains either the aforementioned reason or similar crystals from different types of nuclei [11]. In Figure 61 (e), the effect on exponent *n* with respect to chain length is shown for $E_{CB\text{-}CO}$, CB, and CO. For 1 wt% of C (20) and C (25) addition to $E_{CB\text{-}CO}$, represent a similar value as a control for Avrami exponent, while a decrease in ($n \sim 1$) for 1 wt% of C (30) is obtained. This result shows the formation of needlelike growth from sporadic nuclei in the case of pure $E_{CB\text{-}CO}$ and addition of C (20) and C (25) due to the low degrees of supercooling, resulting in higher free energy and a lower rate of nucleation and thus leading towards sporadic nucleus formation [11]. While in the case of 1 wt% of C (30) addition leads to a lower value, which can be due to the presence of rod-like structure of C (30) crystals. However, the formation of spherulitic structure can not be detected with this set of fittings. In the case of CB blends, the (*n*) value is in the range of ~ 2.7 to ~ 2.5 from pure CB to 1wt% of C (30) addition. This suggests the formation of spherulitic crystals from instantaneous nucleation due to high degrees of supercooling, resulting in lower free energy and a higher rate of nucleation, hence the formation of a large number of nuclei [11]. In contrast to CB blends, (*n*) value increase until C (25) and decrease for 1 wt% C (30) after addition to CO. These values indicate, rod/needle/fiberlike crystal growth from either instantaneous or sporadic nucleation [11]. According to the microscopy images (Figure 60(c) _after 24 h at 22 °C), all three blends represent the needle-like growth, however, the possibility of formation of sporadic nuclei after addition of 1wt% C (20) and C (25) results into an increase in exponent value and for 1wt% of C (30), the high degrees of supercooling between C (30) crystals and crystallization temperature results into instantaneous nucleation of rod-like structure from C (30) crystals.

Thus, according to the Avrami fitting results and microscopy images, the epitaxial growth mechanism in case of 1wt% addition of C (20) and C (25) may occur, whereas, heterogeneous nucleation is found in case of 1wt% C (30) addition. These results support the hypothesis predicted according to the DSC results in section 4.2. Similarly, a study on the difference between epitaxial and heterogeneous nucleation is carried out on crystallization of palm mid fraction on two template molecules: sorbitan tripalmitate and sorbitan tribehenate. Due to similar molecular structure, the chain length of sorbitan tripalmitate and palm mid fraction, epitaxial growth mechanism is responsible for crystal growth, whereas, in the case of sorbitan tribehenate, heterogeneous nucleation takes place due to the different chain length [109].

4.6 Effect of n-alkanes on mechanical properties

Rheological properties of pure fat and fat/oil blends are widely explored for understanding the fundamental relation between microscopic to macroscopic levels. In this study, the focus is on studying the effect of n-alkanes addition to $E_{CB\text{-}CO}$ in terms of rheological properties and its comparison with pure $E_{CB\text{-}CO}$. For understanding the variation in rheological properties of mixtures during temperature and time sweeps, only the storage modulus is considered for better visualization and interpretation. Figure 62 (a), (c), and (e) represents the crystallization kinetics under the rheometer in terms of temperature and time sweeps. The brown graph denotes the temperature change with respect to time. While, Figure 62 (b), (d), and (f) display the amplitude sweep profile after 2 h 30 min of the crystallization process. Each different color indicates a different set of the mixture. The result indicates that in the case of 1 wt% of n-alkanes addition to $E_{CB\text{-}CO}$, the storage modulus increases with respect to carbon chain length. Additionally, the storage modulus compared to the pure eutectic mixture is also increased. The crystallization temperature (CT) (step when storage modulus increases or leaps) is detected as 22 °C for pure eutectic as well as for mixture with 1 wt% of C (20). Whereas, CT increases to ~ 27 °C and ~ 30 °C for mixture with 1 wt% of C (25) and C (30) respectively. In the case of a mixture with 1 wt% of C (30), stepwise crystallization is observed due to phase separation between crystals of C (30) and the rest of the CB-CO mixture. This result is in line with the SFC profile from the NMR experiment in Figure 61 (a). Similar to previous experiments, rheological properties were also further studied for pure CB and CO. Figure 59 (d) shows that adding 1 wt% of C (20) and C (25) in CB does not change significantly CT. The mixtures show similar behavior of stepwise crystallization as pure CB except for C (30), which indicates a small step just before reaching the first plateau region. The small step represents the crystallization of C (30) crystals and another step suggests that either a polymorphic transition or co-crystallization of two polymorphs is occurring. Moreover, the addition of n-alkanes to CB leads to a decrease in storage modulus. Due to enhanced interactions of HMF from CB with n-alkanes, the rest of the mixture remains in the liquid state at this particular timeline and hence resulted in a higher fraction of the mobile phase entrapped in a crystal network. Therefore, the reduced storage modulus is observed as compared to pure CB. Altogether, the rheological profile for CB displays similar behavior as previous experiments from DSC and SFC profiles.

On contrary, to the effect on CB, the addition of n-alkanes displays differences in the rheological properties of CO. In the case of 1 wt% of C (20) and C (25) with CO, the storage

modulus value after 2 h 30 min is distinctly unchanged with respect to the pure eutectic mixture, whereas, for a mixture with 1 wt% of C (30), the storage modulus value increases greatly. Furthermore, the behavior is similar to a mixture of 1 wt% of C (30) with $E_{CB\text{-}CO}$: CT increases to ~ 35 °C along with stepwise crystallization, indicating phase separation. The correlation between crystallization kinetics under the quiescent condition and constant oscillation demonstrates similar findings due to the stronger interaction of CO, which is a mixture of short-chained saturated TAGs and n-alkanes.

Further, the experiments proceed with the amplitude sweep study to understand the viscoelastic and structural properties of crystal networks. The strain amplitude sweep was performed for the range of strain from 0.001 % to 100 %. Closed symbols represent storage modulus (*G′*) and open symbols as loss modulus (*G″*). These graphs are differentiated into linear and non-linear viscoelastic regimes represented as LVE and NLVE. According to Figure 61 (b), *G′* is higher than *G″* which points that sample behaves as 'elastic solid' for all the blends under small deformations. Moreover, the LVE range has decreased after the addition of 1 wt% of n-alkanes to $E_{CB\text{-}CO}$ due to an increase in modulus (solidity). Whereas, in the case of CB, the LVE range has increased after the addition of 1 wt% of n-alkanes as compared to pure CB. Correspondingly in the case of CO mixtures, 1 wt% of C (20) and C (25) display a similar LVE range as pure CO, while, decreased LVE range is observed after the addition of 1 wt% of C (30) due to higher modulus value.

As explained earlier in section 3, most of the previous work on fat crystals has been performed in the LVE range as it focused on interaction forces establishing the connectivity of the crystal network. In the LVE range, the interparticle network or in the present case the crystal aggregate network is held together by van der Waals's attractive and Born's repulsive forces [92]. These forces can also be denoted as the bonds between the particle-particle clusters. Therefore, with a small amplitude, the stretching of these bonds between particles is small enough to leave the bond intact. Hence, any specific changes during a small amplitude could not be observed.

The breaking of a crystal network depends strongly on the type of morphology formed during the crystallization as the inter-particle bond stretching differs according to the geometry of crystals [25]. Therefore, all these different blends show a unique breaking behavior of the crystal network as each blend has a variety of (mixtures of needles and spherulitic) morphology under crystallization. In this study, typically three types of breaking of a network were observed: 1. In $E_{CB\text{-}CO}$ blends with n-alkanes, only a small number of crystals are formed which

are not interconnected. Hence, the breaking in this blend is likely to refer to the dissolving of the small crystals back to a liquid and small fractures in individual crystals. 2. For CO and CB, the slippage at large deformations is observed, and hence clear NLVE region does not occur.

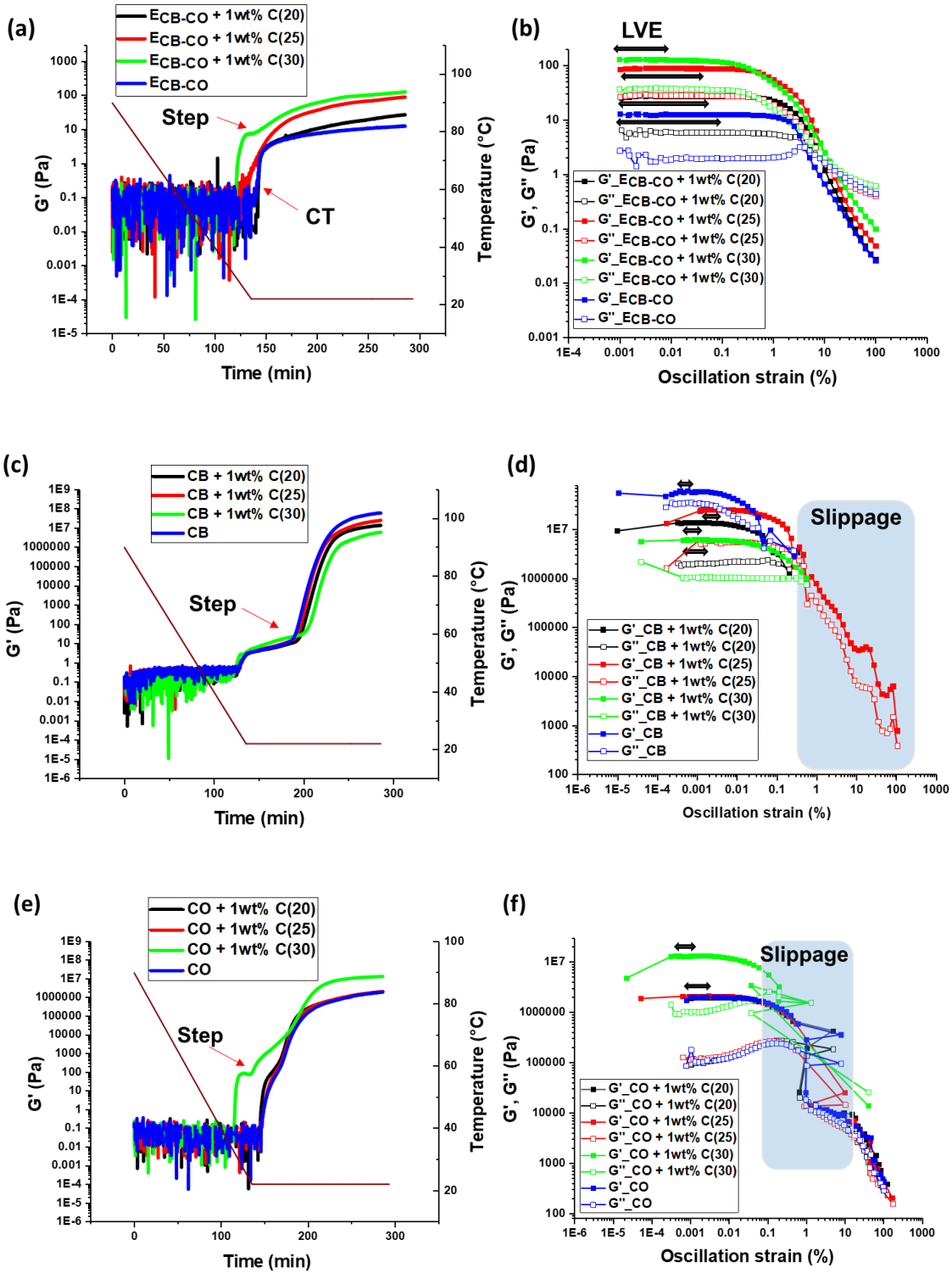

Figure 62: Effect on rheological properties after addition of n-alkanes to E_{CB-CO}. (a), (c) and (e) represent temperature and time sweep plotted against time in minutes and the brown graph profile is the temperature vs. time which provides precise temperature detection with respect to rheological properties for E_{CB-CO}, CB, and CO respectively. 'CT' represents the crystallization temperature position in each case where G' crosses over G''. (b), (d), and (f) represent the amplitude sweep profile for the same sequence. The slippage occurs in the case of CB and CO samples due to high rigidity to jamming of needlelike morphology at higher strain value respectively.

3. In the case of pure CO and blends with 1 wt% of n-alkanes, the slippage occurs from 1 to 10% of strain. To understand this in more depth, in situ rheo-microscopy was performed. This direct observation shows, as the amplitude increased, small branches of needles detach from the mother branch of the tree-like structures and these small needles further promote slippage. They are caged between the mother branches, hence at higher amplitude, proper values cannot be detected. However, after breaking off small needles the mobility of the upper geometry becomes smooth again and hence the measurement accurately took place.

In the case of CB and its blends with 1 wt% of n-alkanes the LVE range increases due to the highly mobile phase entrapped in the solid crystal network and is followed by artifacts occurring due to slippage (which is indicated as a blue surface). To understand profoundly the amplitude sweep profile, in situ microscopy with rheology was implemented. For the sake of understanding, only until 30 minutes, the crystallization was performed (as the increase in modulus (solidity) could destroy the glass plate geometry which was used instead of steel plate) for CB samples. The result for only a blend with 1 wt% of C (25) has been shown. The videos were captured from the upper plate towards the lower plate (Refer Appendix video V3). Hence, from in situ microscopy, the movement of the 3D fat crystal network flowing according to the defined oscillatory force from crystals that were attached to the upper geometry towards the lower glass plate is visible. These videos were taken at the edge of the geometry instead of the center as the amplitude is higher at the edge hence the movement was easy to capture. Images extracted from these videos are shown in Figure 63. At the beginning of each amplitude sweep, the crystals at the upper plate region (UPR) were captured. No specific crystal morphology is observed. As the deformation increase, the middle region (MR) of the 3D crystal network is visible, where a needle-like random aggregative structure is observed. Further increase of amplitude leads to a decrease in G', which is indicated by an image at the lower plate region (LPR). In this image, the orange circles indicate the connection between spherical crystals as a

result of an aggregation of needles. So it can be predicted that after a 10% increase in the amplitude, these spherical crystals leave their position from the networks and slide with each other. Thus, at the highest amplitude, the crystal network breaks down into individual crystals.

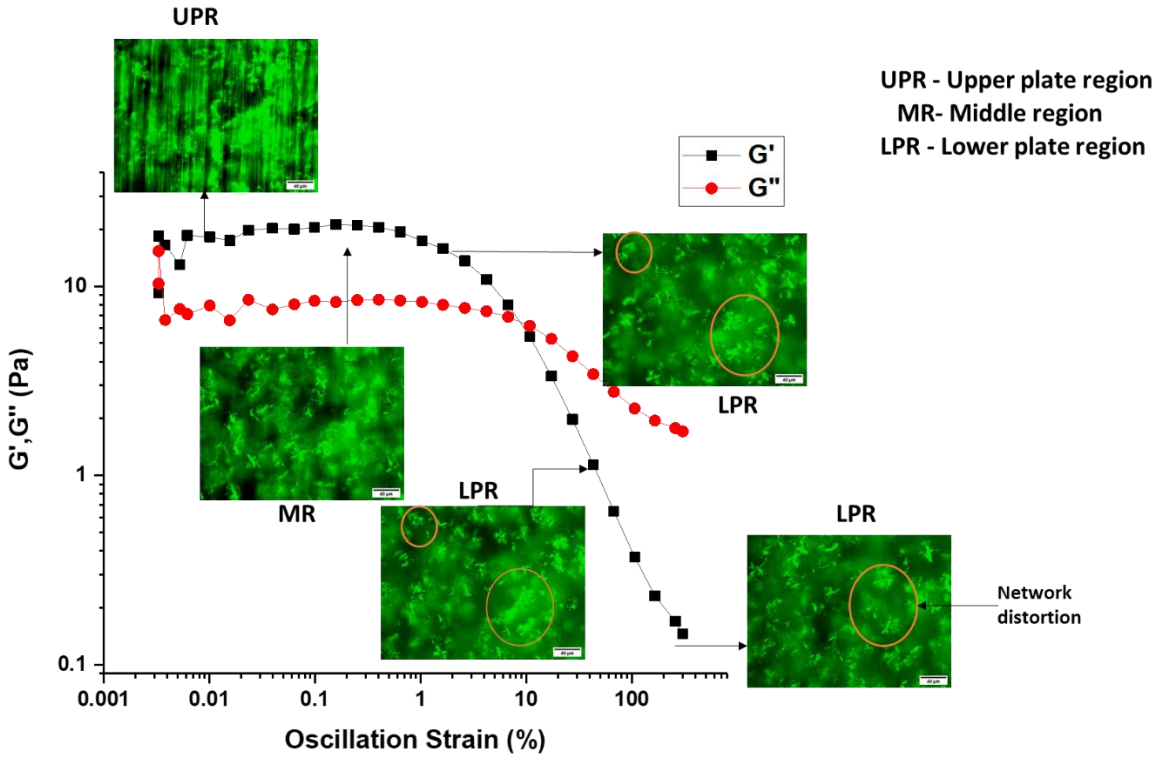

Figure 63: In situ microscopy to CB + 1 wt% C (25) sample representing the amplitude sweep after 30 minutes at 22 °C. The videos during amplitude sweep are taken from the upper plate towards the lower plate, hence individual images with a change in crystal network with respect to the amplitude are marked with an orange zone. The scale bar = 40µm.

4.7 Summary

The results in this study indicate that the crystallization and melting temperature of a eutectic mixture $E_{CB\text{-}CO}$ increase after the addition of n-alkanes. Together with thermal properties, the solid fat content (SFC) and storage modulus (*G'*) also increases as compared to $E_{CB\text{-}CO}$. The reason for this behavior is the strong van der Waal's attractive interaction of CO with n-alkanes, which leads to the promotion of the crystallization process in the blends. Based on the current results, the possible schematic for interaction between $E_{CB\text{-}CO}$ and n-alkanes is shown in Figure

64. Figure 64 (a) demonstrates the nomenclature of the structure of n-alkanes along with pure CO and CB at solid-state. As CO and CB are mixtures of a large number of TAGs, the structure in Figure 64 (a) displays the saturated (medium-chain (C (12:0)) and mono-unsaturated (C (18:1)) TAG which are the main constituents of CO and CB respectively. Figure 64 (b) shows the possible interactions occurring at the solid-state of ternary blends. According to present results, and previous studies on crystallization modifiers to lipid systems, the interaction of "seed" or "substrate" to the remaining part of lipid is strongly dependent on the chain length, molecular size, and saturation degree. Due to spatial arrangements of molecules, the ones having similar size and shape attract each other and try to form strong and dense crystal packing, hence leading to better physicochemical properties. At the same time, these modifiers at lower concentrations act as "templates" to induce crystallization without affecting crystal morphology. This speculation was indeed confirmed with DSC, NMR, and PLM measurements respectively. In this study, C (20), and C (25) acted as a "template" to induce epitaxial crystalline growth, whereas, C (30) induces heterogeneous nucleation in a eutectic mixture. CO tends to crystallize from borders to the center of the system, hence, the addition of such templates or seeds to a eutectic mixture undeniably helped to crystallize faster and constitutes surfaces for aggregation of other TAGs from CO and CB. However, as the length of C (30) is much higher than CO and also defects due to kink of CB, phase separation tends to occur.

In case of C (20) addition, the possible strong interaction occurs between the alkyl chain of saturated TAGs from CO to the n-alkane. This lateral interaction of the alkyl chain results in closely packed arrangements and hence the better physicochemical properties of eutectic mixture obtains. There is a possibility that one molecule of C (20) interacts with the two alkyl chains of TAGs from CO as shown in figure 8 (b). The bilayer or multilayer (represented as vertical stacking) arrangements of CO with C (20) occurs. Additionally, the TAGs from CB arrange themselves in a vertical arrangement along with the stacking of CO. However, the precise crystal domain arrangement is yet to be understood. Similar behavior with respect to the C (25) addition to the eutectic mixture is predicted according to the experimental results. Whereas, after the addition of C (30), the clear phase separation is shown with lateral prolongation of CB and CO crystals with respect to C (30). Thus, this schematic indicates that the addition of C (20) and C (25), stabilizes the fatty acids of the fat molecule, whereas, C (30) addition act as a nucleation site.

Furthermore, the results also determined that in the case of a eutectic mixture, n-alkanes acted as seed crystals with less concentration and provide a hint towards an organo-gelator role with

more concentration (e.g. at and above 3 wt%) for a higher number of carbon chain length (C (25) and C (30) with respect to models that are used). Further experiments with x-ray diffraction and rheology are of interest to understand in detail the interactions based on the unit cell of polymorphs, precise construction of ternary plot as well as to confirm the hypothesis of the formation of oleogel respectively. Thus, to conclude, that after studying such ternary phase behavior, a model system like CB and CO, provides deep insight into tailoring several products in confectionary application.

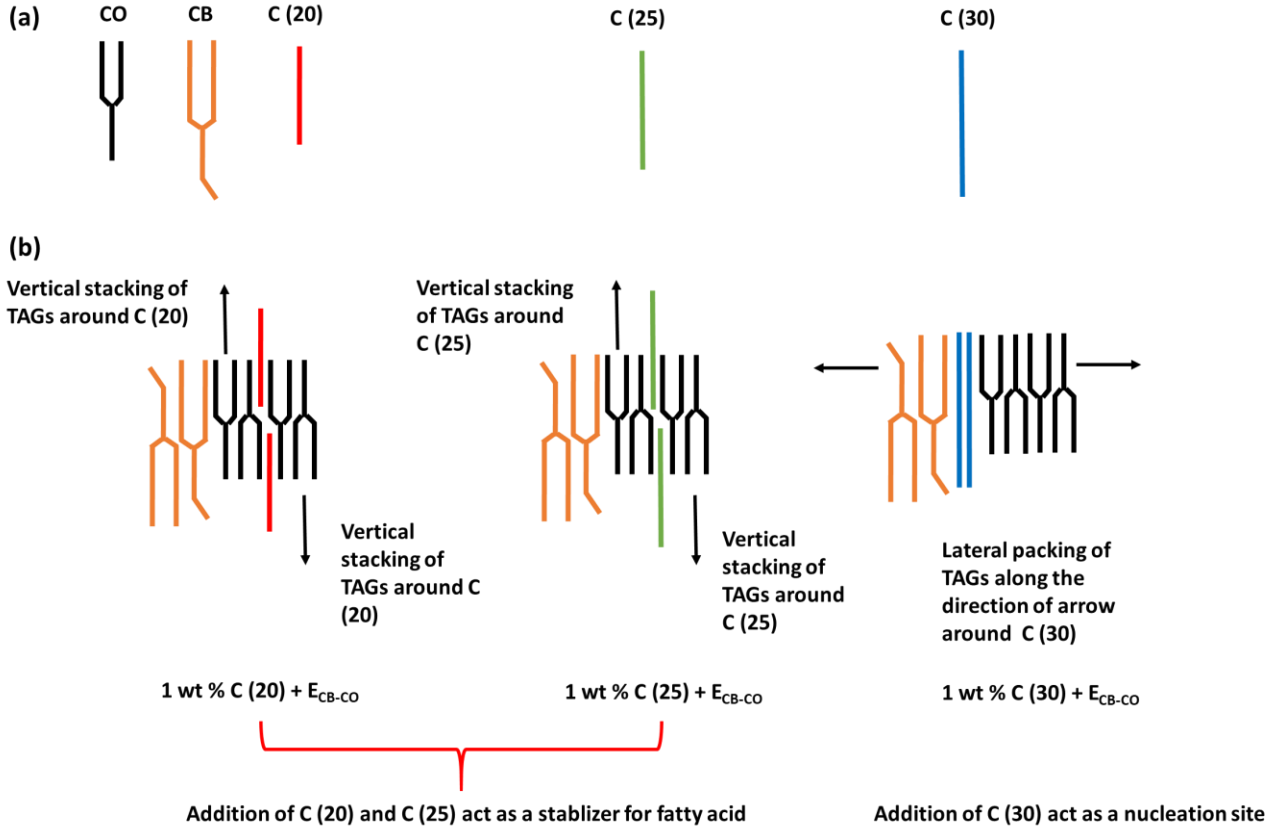

Figure 64: Schematic representing possible interactions of CO and CB in a eutectic mixture to C (20), C (25), and C (30).

Conclusion

Fundamental studies of thermal, physical, and mechanical properties of individual fats and oils and their respective blends ultimately help to optimize the process for manufacturing good quality food products. Therefore, it is necessary to investigate the changes that occur during mixing two fats or fat/oil on their physicochemical properties.

This work has been differentiated into four sections. Initially, the fatty acid and TAG analysis of bulk fat was carried out in order to understand the chemical composition. According to the results, CB contains monounsaturated TAGs as the main component, and oleic acid being the unsaturated part. Along with mono unsaturaterd fatty acid, the fatty acid having (C20:0), (C22:0), and (C24:0) chain length has also been identified. This explains why CB melts at higher temperatures although stated in various studies that the melting temperature is in the range of 17 to 36 °C. While the fatty acid analysis of CO reveals ~87 % of saturated fatty acid which is composed of mainly lauric acid (C12:0) and myristic acid (C14:0). Therefore, melts around room temperature.

The next three sections of this present work were focused on understanding the binary mixing behavior of Cocoa Butter/Tristearin (CB/TS), Cocoa Butter/Coconut Oil (CB/CO), and ternary mixing behavior of eutectic mixture ($E_{CB\text{-}CO}$) with three different derivatives of paraffin wax respectively.

In case of binary mixing behavior of CB/TS blends, the effect on thermal properties is studied initially, and based on the results of the thermogram the pseudo-binary phase diagram was created. According to the thermal properties, the melting and crystallization temperature of TS decreases whereas, there is no significant effect on CB in CB/TS blends. Moreover, solid-liquid-solid (S-L-S) transition in case of TS is observed during the melting process. This transition temperature of TS in the blend is also reduced as per the DSC thermograms. Next, the pseudo-binary phase diagram reveals that the CB/TS blends show monotectic mixing behavior. This includes solidus, liquidus, and S-L-S transition line in order to differentiate between the co-existence of solid, liquid, and solid of TS and liquid of TS respectively. The liquidus and solidus line further fitted with Bragg-Williams approximation in order to find out the interaction between CB-TS in liquid and solid region. According to the fitting result, the positive value of the non-ideality parameter indicates phase separation, whereas, a negative value indicates unlike molecules form the crystal structure. In case of CB/TS blends, after fitting the non-ideality parameter results as a positive value hence, phase separation of CB-TS.

Moreover, in order to understand the interaction between CB and TS, CARS analysis was performed. According to the microscopic and spectral analysis, the phase separation in CB and TS is further confirmed. Therefore, the results from DSC, thermodynamic analysis, and CARS are in accordance with each other. Although the phase separation is confirmed with DSC and thermodynamical analysis, the reason for the decrease in melting and crystallization temperature of TS after the addition of CB is depicted by XRD analysis. According to these results, CB provokes the S-L-S transition in TS, which results in defects in the crystal structure of TS and melts quickly as compared to the pure TS. Thus, altogether, the results reveal that the addition of CB, which contains defects due to unsaturated part act as an impurity in CB/TS blends and hence reduces the melting and crystallization temperature of the blend.

After studying the binary mixing behavior of CB and TS, which is a pure saturated fat, the next system to understand the effect on CB was the addition of CO, which is a bulk fat that mainly consists of small and medium-chain saturated TAGs. Similar to CB/TS, the thermal properties of this binary blend are also studied. According to the DSC analysis, the melting and crystallization temperature of the blend decreased to a certain mixture and increased back again. Furthermore, the pseudo phase diagram was plotted based on DSC re-melting segment, which reveals that CB/CO blend behaves as a eutectic mixture. This eutectic mixture is in between 60 to 70 wt% of CO. Further analysis indicates that 65 wt% of CO 35 wt% of CB recorded the lowest melting temperature (~16 °C), which is less than pure CB (~21 °C) and CO (~24 °C). Later, the fitting of Bragg-Williams approximation to the liquidus line of CB/CO phase diagram reveals positive value from pure CB to the eutectic mixture ($E_{CB\text{-}CO}$) and negative value from $E_{CB\text{-}CO}$ to CO. These two values of the non-ideality parameter indicates that this particular approximation has limitation for such bulk mixed blends and hence the precise fitting was not able to carry out. Next, the morphological studies show that CB crystallizes into a mixture of spherulitic and granulitic crystal structure and after the addition of CO, the morphology changes into a spherulitic structure composed of needles as CO crystallizes into a long needlelike structure. According to the morphological results, the least crystals were detected for $E_{CB\text{-}CO}$ after 24 h at 22 °C. Later to understand the thermal behavior crystallization kinetics was studied in terms of solid fat content after 24 h at 22 °C for each of CB/CO blends. This study indicates that the addition of CO inhibits the crystallization process of CB by either stopping the co-crystallization or polymorphic transition. Furthermore, the least value for SFC is detected for $E_{CB\text{-}CO}$. This reveals that at eutectic mixture fewer crystals are formed and hence melt quickly. Next, the crystallization kinetics under constant oscillation

strain was conducted, which shows a similar result as quiescent crystallization kinetics. The rheological properties reveal that, as the concentration of CO increases, the LVE range increases due to less connectivity between the crystal blobs. The breaking of the crystal network was further analyzed in terms of fractal dimension (d_f). As the connectivity between crystal blobs decreases the fractal dimension increases. Hence, for the mixture of 70 wt% to 30 wt% of CB, a higher value of fractal dimension was obtained, whereas, 2D fractal dimension in case of pure CO. This is in agreement with the Avrami exponent from the fitting of the Avrami equation to the SFC profile and morphological studies. Moreover, the relation between mesoscopic interactions with nanoscopic interaction reveals that, for $E_{CB\text{-}CO}$, a higher size of nanoplatelet is predicted than pure CB and CO hence, less stable crystal formation. Altogether, these mixing behavior helped to understand the CB and CO systems and if mixed what kind of interactions are happening which would be indeed useful in case of confectionary products with CB and CO in it as CO can be used as a CB substitute.

As explained earlier, the concept of fractal dimension in the fat crystal network reveals the mass as well as spatial arrangements of fat crystals, which ultimately will help to understand the mouthfeel of the products containing fat crystals. Therefore, a precise calculation is necessary to make. This current study shows that fractal dimension is dependent on time hence, at a particular timeline it is necessary to calculate. Therefore, in this study Kraus model was fitted to the amplitude sweep of the CB/CO blend. The fractal dimension calculation was only carried out for CB/CO blends as the precise amplitude sweep for CB/TS blends was not possible due to high solidity (slippage).

Eventually, the idea of the addition of paraffin wax derivatives in a eutectic mixture was applied as previous studies imply that paraffin wax is used for providing shine to the chocolate. Even though the commercial use is known the interaction of this wax molecule with CB was unknown hence, this study was focused on the addition of derivatives of paraffin wax to pure CB, CO, and $E_{CB\text{-}CO}$. Similar experiments were carried out as CB/CO in case of C (20), C (25), and C (30) in addition to the $E_{CB\text{-}CO}$, CB, and CO. The initial experiments reveal that a higher amount (above 3 wt%) of n-alkanes acts as an organogelator hence, oleogel like behavior is observed. As $E_{CB\text{-}CO}$ stays in liquid after 24 h at 22 °C, the clear oleogel like behavior is visible. However, in this study only 1 wt% of n-alkanes addition was analyzed further as a higher concentration of n-alkanes leads to the phase separation. Thus, the thermal and mechanical properties revealed that after the addition of 1 wt% of n-alkanes in $E_{CB\text{-}CO}$, the crystallization, melting temperature, and storage modulus increased. A similar result is obtained in case of

1wt% addition of n-alkanes to CO, whereas there is no significant effect on CB. Therefore, the effect on $E_{CB\text{-}CO}$ is dominated by the interaction of CO with n-alkanes rather than CB. Thus, the whole research section concludes that C (20) and C (25) act as “template” or “seed” for CO crystallization by having strong lateral interaction between the alkyl chain of TAG from CO and n-alkane, whereas, heterogeneous nucleation occurs with the addition of C (30).

Thus, altogether, this complete set of research studies is divided into a fundamental understanding of the mixing behavior of fat-fat, fat-oil, and fat-oil-wax systems. Along with a fundamental understanding of mixing behavior of different blends of CB and CO and paraffin wax addition to CB, CO and $E_{CB\text{-}CO}$, this particular study also be useful in the practical applications of different blends. Eventually, a study on variety of different ratios will help the industrial personnel to design the unique product with precise characteristics.

Outlook

In the future, the focus will be on understanding the organogel behavior of $E_{CB\text{-}CO}$ and derivatives of waxes. The mechanical properties of organogel will help understand the stability and storage life in terms of practical applications. Furthermore, the nanoscale arrangements of wax derivatives with fat and oil are yet to be determined hence, this would also be a question to answer in the future. Furthermore, the tribology of organogels will also help to understand the swallowing behavior of the products containing gels. Furthermore, the relation of fractal dimension with mouthfeel will also be crucial to understand.

References

[1] K. Sato, “Polymorphism of Lipid Crystals,” *Crystallization of Lipids*. pp. 17–60, 14-Feb-2018.

[2] S. M. Abdulkarim, M. W. Myat, H. M. Ghazali, K. Roselina, and K. A. Abbas, “Sensory and physicochemical qualities of palm olein and sesame seed oil blends during frying of banana chips,” *J. Agric. Sci.*, vol. 2, no. 4, p. 18, 2010.

[3] S. Tenjarla, “Microemulsions: an overview and pharmaceutical applications,” *Crit. Rev. Ther. Drug Carr. Syst.*, vol. 16, no. 5, 1999.

[4] M. Berdick, *The role of fats and oils in cosmetics*, vol. 49. 1972.

[5] P. Lonchampt and R. W. Hartel, *Fat bloom in chocolate and compound coatings*, vol. 106. 2004.

[6] C. LOISEL, G. LECQ, G. KELLER, and M. OLLIVON, “Dynamic Crystallization of Dark Chocolate as Affected by Temperature and Lipid Additives,” *J. Food Sci.*, vol. 63, no. 1, pp. 73–79, 2006.

[7] R. D. O’brien, *Fats and oils: formulating and processing for applications*. CRC press, 2008.

[8] T. A. Vilgis, “Soft matter food physics - The physics of food and cooking,” *Reports Prog. Phys.*, vol. 78, no. 12, p. 124602, 2015.

[9] A. P. B. Ribeiro *et al.*, “Crystallization modifiers in lipid systems,” *J. Food Sci. Technol.*, vol. 52, no. 7, pp. 3925–3946, 2015.

[10] Walter Borchrad Ott, *Crystallography*. Springer-Verlag Berlin Heidelberg, 1993.

[11] A. G. Marangoni and L. H. Wesdorp, *Structure and properties of fat crystal networks*. CRC Press, 2012.

[12] N. Garti and K. Sato, *Crystallization and polymorphism of fats and fatty acids*. M. Dekker, 1988.

[13] I. Pascher, M. Lundmark, P.-G. Nyholm, and S. Sundell, “Crystal structures of membrane lipids,” *Biochim. Biophys. Acta (BBA)-Reviews Biomembr.*, vol. 1113, no. 3–4, pp. 339–373, 1992.

[14] D. L. Dorset, *Crystallography of the polymethylene chain: an inquiry into the structure of waxes*, vol. 17. Oxford University Press on Demand, 2005.

[15] K. Sato, *Crystallization of Lipids*. 2018.

[16] N. C. Acevedo and A. G. Marangoni, “Nanostructured fat crystal systems,” *Annu. Rev. Food Sci. Technol.*, vol. 6, pp. 71–96, 2015.

[17] C. Himawan, V. M. Starov, and A. G. F. Stapley, “Thermodynamic and kinetic aspects of fat crystallization,” *Adv. Colloid Interface Sci.*, vol. 122, no. 1–3, pp. 3–33, 2006.

[18] K. Sangwal, *Additives and crystallization processes: from fundamentals to applications*. John Wiley & Sons, 2007.

[19] D. Turnbull, “Phase changes,” in *Solid state physics*, vol. 3, Elsevier, 1956, pp. 225–306.

[20] 20,” *J. Chem. Phys.*, vol. 76, no. 10, pp. 5098–5102, 1982.

[21] M. Avrami, “Kinetics of phase change. I General theory,” *J. Chem. Phys.*, vol. 7, no. 12, pp. 1103–1112, 1939.

[22] M. Avrami, “Kinetics of phase change. II transformation-time relations for random distribution of nuclei,” *J. Chem. Phys.*, vol. 8, no. 2, pp. 212–224, 1940.

[23] M. Avrami, “Granulation, phase change, and microstructure kinetics of phase change. III,” *J. Chem. Phys.*, vol. 9, no. 2, pp. 177–184, 1941.

[24] A. Bunde and S. Havlin, “Fractals and disordered systems. 1991.” Berlin, Springer.

[25] B. Joshi, S. Beccard, and T. A. Vilgis, “Fractals in crystallizing food systems,” *Curr. Opin. Food Sci.*, vol. 21, pp. 39–45, 2018.

[26] L. G. B. Bremer, T. van Vliet, and P. Walstra, “Theoretical and experimental study of the fractal nature of the structure of casein gels,” *J. Chem. Soc. Faraday Trans. 1 Phys. Chem. Condens. Phases*, vol. 85, no. 10, pp. 3359–3372, 1989.

[27] D. Pérez-Martínez, C. Alvarez-Salas, J. A. Morales-Rueda, J. F. Toro-Vazquez, M. Charó-Alonso, and E. Dibildox-Alvarado, “The effect of supercooling on crystallization of cocoa butter-vegetable oil blends,” *J. Am. Oil Chem.*

Soc., vol. 82, no. 7, pp. 471–479, 2005.

[28] S. S. Narine and A. G. Marangoni, "Fractal nature of fat crystal networks," *Phys. Rev. E*, vol. 59, no. 2, p. 1908, 1999.

[29] G. Huber and T. A. Vilgis, "Universal properties of filled rubbers: Mechanisms for reinforcement on different length scales," *Kautschuk und Gummi, Kunststoffe*, vol. 52, no. 2, pp. 102–107, 1999.

[30] G. Huber, T. A. Vilgis, and G. Heinrich, "Universal properties in the dynamical deformation of filled rubbers," *J. Phys. Condens. Matter*, vol. 8, no. 29, p. L409, 1996.

[31] T. A. Vilgis, G. Heinrich, and M. Klüppel, *Reinforcement of polymer nano-composites: theory, experiments and applications*. Cambridge University Press, 2009.

[32] R. E. Timms, "Phase behaviour of fats and their mixtures," *Prog. Lipid Res.*, vol. 23, no. 1, pp. 1–38, 1984.

[33] S. T. Beckett, *Industrial ChocolateManufacture and Use*. Blackwell, Oxford, 1999.

[34] C. Loisel, G. Keller, G. Lecq, C. Bourgaux, and M. Ollivon, "Phase transitions and polymorphism of cocoa butter," *J. Am. Oil Chem. Soc.*, vol. 75, no. 4, pp. 425–439, 1998.

[35] R. L. Wille and E. S. Lutton, "Polymorphism of cocoa butter," *J. Am. Oil Chem. Soc.*, vol. 43, no. 8, pp. 491–496, 1966.

[36] M. Windbergs, C. J. Strachan, and P. Kleinebudde, "Investigating the Principles of Recrystallization from Glyceride Melts," *AAPS PharmSciTech*, vol. 10, no. 4, pp. 1224–1233, 2009.

[37] R. Campos, M. Ollivon, and A. G. Marangoni, "Molecular composition dynamics and structure of cocoa butter," *Cryst. Growth Des.*, vol. 10, no. 1, pp. 205–217, 2010.

[38] I. Rothkopf and W. Danzl, "Changes in chocolate crystallization are influenced by type and amount of introduced filling lipids," *Eur. J. lipid Sci. Technol.*, vol. 117, no. 11, pp. 1714–1721, 2015.

[39] M. H. A. Jahurul *et al.*, "Characterization of crystallization and melting profiles of blends of mango seed fat and palm oil mid-fraction as cocoa butter replacers using differential scanning calorimetry and pulse nuclear magnetic resonance," *Food Res. Int.*, vol. 55, pp. 103–109, 2014.

[40] M. Lipp and E. Anklam, "Review of cocoa butter and alternative fats for use in chocolate—Part B. Analytical approaches for identification and determination," *Food Chem.*, vol. 62, no. 1, pp. 99–108, 1998.

[41] e M. Lipp and E. Anklam, "Review of cocoa butter and alternative fats for use in chocolate—part A. Compositional data," *Food Chem.*, vol. 62, no. 1, pp. 73–97, 1998.

[42] M. Geary and R. Hartel, "Crystallization Behavior and Kinetics of Chocolate-Lauric Fat Blends and Model Systems," *JAOCS, J. Am. Oil Chem. Soc.*, vol. 94, no. 5, pp. 683–692, 2017.

[43] S. D. Williams, K. L. Ransom-Painter, and R. W. Hartel, "Mixtures of palm kernel oil with cocoa butter and milk fat in compound coatings," *J. Am. Oil Chem. Soc.*, vol. 74, no. 4, pp. 357–366, 1997.

[44] L. B. Quast, V. Luccas, A. P. B. Ribeiro, L. P. Cardoso, and T. G. Kieckbusch, "Physical properties of tempered mixtures of cocoa butter, CBR and CBS fats," *Int. J. Food Sci. Technol.*, vol. 48, no. 8, pp. 1579–1588, 2013.

[45] A. R. M. Ali and P. S. Dimick, "Melting and solidification characteristics of confectionery fats: anhydrous milk fat, cocoa butter and palm kernel stearin blends," *J. Am. Oil Chem. Soc.*, vol. 71, no. 8, pp. 803–806, 1994.

[46] M. S. Miskandar, Y. B. C. Man, R. A. Rahman, I. N. Aini, and M. S. A. Yusoff, "Effects of emulsifiers on crystal behavior of palm oil blends on slow crystallization," *J. Food Lipids*, vol. 14, no. 1, pp. 1–18, 2007.

[47] T. Tran, N. L. Green, and D. Rousseau, "Spheroidal fat crystals: Structure modification via use of emulsifiers," *Cryst. Growth Des.*, vol. 15, no. 11, pp. 5406–5415, 2015.

[48] C. Liu, Z. Zheng, F. Zaaboul, C. Cao, X. Huang, and Y. Liu, "Effects of wax concentration and carbon chain length on the structural modification of fat crystals," *Food Funct.*, vol. 10, no. 9, pp. 5413–5425, 2019.

[49] A. I. Blake, E. D. Co, and A. G. Marangoni, "Structure and physical properties of plant wax crystal networks and their relationship to oil binding capacity," *J. Am. Oil Chem. Soc.*, vol. 91, no. 6, pp. 885–903, 2014.

[50] G. Höhne, W. F. Hemminger, and H.-J. Flammersheim, *Differential scanning calorimetry*. Springer Science &

Business Media, 2013.

[51] R. Haynes, *Optical microscopy of materials*. Springer Science & Business Media, 2013.

[52] R. Oldenbourg, “Polarized light microscopy: principles and practice,” *Cold Spring Harb. Protoc.*, vol. 2013, no. 11, p. pdb-top078600, 2013.

[53] S. Bresson, D. Rousseau, S. Ghosh, M. El Marssi, and V. Faivre, “Raman spectroscopy of the polymorphic forms and liquid state of cocoa butter,” *Eur. J. lipid Sci. Technol.*, vol. 113, no. 8, pp. 992–1004, 2011.

[54] S. Sunder, R. Mendelsohn, and H. J. Bernstein, “Raman studies of the CH and CD stretching regions in stearic acid and some specifically deuterated derivatives,” *Chem. Phys. Lipids*, vol. 17, no. 4, pp. 456–465, 1976.

[55] P. Rostron, S. Gaber, and D. Gaber, “Raman Spectroscopy , Review,” no. September, 2016.

[56] N. Billecke *et al.*, “Perilipin 5 mediated lipid droplet remodelling revealed by coherent Raman imaging,” *Integr. Biol.*, vol. 7, no. 4, pp. 467–476, 2015.

[57] W. H. De Jeu, *Basic X-ray scattering for soft matter*. Oxford University Press, 2016.

[58] Lon J. Mathias, *Solid State NMR of Polymers*. New York: Springer Science+Business Media, LLC, 1991.

[59] T. Mezger, *The rheology handbook: for users of rotational and oscillatory rheometers*. European Coatings, 2020.

[60] T. Inoue, Y. Hisatsugu, R. Yamamoto, and M. Suzuki, “Solid–liquid phase behavior of binary fatty acid mixtures: 1. Oleic acid/stearic acid and oleic acid/behenic acid mixtures,” *Chem. Phys. Lipids*, vol. 127, no. 2, pp. 143–152, 2004.

[61] M. Abes, L. Bouzidi, and S. S. Narine, “Crystallization and phase behavior of 1, 3-propanediol esters: II. 1, 3-Propanediol distearate/1, 3-propanediol dipalmitate (SS/PP) and 1, 3-propanediol distearate/1, 3-propanediol dimyristate (SS/MM) binary systems,” *Chem. Phys. Lipids*, vol. 150, no. 1, pp. 89–108, 2007.

[62] E. E. Brumbaugh, M. L. Johnson, and C. Huang, “Non-linear least squares analysis of phase diagrams for non-ideal binary mixtures of phospholipids,” *Chem. Phys. Lipids*, vol. 52, no. 2, pp. 69–78, 1990.

[63] A. G. Lee, “Lipid phase transitions and phase diagrams II. Mixtures involving lipids,” *BBA - Rev. Biomembr.*, vol. 472, no. 3–4, pp. 285–344, 1977.

[64] B. G. Tenchov, “Nonuniform lipid distribution in membranes,” *Prog. Surf. Sci.*, vol. 20, no. 4, pp. 273–340, 1985.

[65] J. Reyes-Hernández, E. Dibildox-Alvarado, M. A. Charó-Alonso, and J. F. Toro-Vazquez, “Physicochemical and rheological properties of crystallized blends containing trans-free and partially hydrogenated soybean oil,” *JAOCS, J. Am. Oil Chem. Soc.*, vol. 84, no. 12, pp. 1081–1093, 2007.

[66] Anoop, “Finding the Fractal Dimension using Box Counting method.,” *MATLAB Central File Exchange.* .

[67] N. Billecke *et al.*, “Chemical imaging of lipid droplets in muscle tissues using hyperspectral coherent Raman microscopy,” *Histochem. Cell Biol.*, vol. 141, no. 3, pp. 263–273, 2014.

[68] F. Fleissner, M. Bonn, and S. H. Parekh, “Microscale spatial heterogeneity of protein structural transitions in fibrin matrices,” *Sci. Adv.*, vol. 2, no. 7, p. e1501778, 2016.

[69] Y. Liu, Y. J. Lee, and M. T. Cicerone, “Broadband CARS spectral phase retrieval using a time-domain Kramers–Kronig transform,” *Opt. Lett.*, vol. 34, no. 9, pp. 1363–1365, 2009.

[70] A. G. Marangoni, *Structure-function analysis of edible fats*. Elsevier, 2018.

[71] N. Brunello, S. E. McGauley, and A. Marangoni, “Mechanical properties of cocoa butter in relation to its crystallization behavior and microstructure,” *LWT-Food Sci. Technol.*, vol. 36, no. 5, pp. 525–532, 2003.

[72] F. H. Mattson and A. VOLPENHEIN, “The specific distribution of fatty acids in the glycerides of vegetable fats,” *Order*, vol. 1, p. 2, 1961.

[73] L. America and U. S. Congress, “C o c o a h t,” no. 7, pp. 1–2.

[74] S. Marty and A. G. Marangoni, “Effects of cocoa butter origin, tempering procedure, and structure on oil migration kinetics,” *Cryst. Growth Des.*, vol. 9, no. 10, pp. 4415–4423, 2009.

[75] J. F. Toro-Vazquez, D. Pérez-Martínez, E. Dibildox-Alvarado, M. Charó-Alonso, and J. Reyes-Hernández, “Rheometry and Polymorphism of Cocoa Butter During Crystallization Under Static and Stirring Conditions,”

JAOCS, J. Am. Oil Chem. Soc., vol. 81, no. 2, pp. 195–202, 2004.

[76] M. H. A. Jahurul *et al.*, "Hard cocoa butter replacers from mango seed fat and palm stearin," *Food Chem.*, vol. 154, pp. 323–329, 2014.

[77] N. Biswas, Y. L. Cheow, C. P. Tan, S. Kanagaratnam, and L. F. Siow, "Cocoa butter substitute (CBS) produced from palm mid-fraction/palm kernel oil/palm stearin for confectionery fillings," *J. Am. Oil Chem. Soc.*, vol. 94, no. 2, pp. 235–245, 2017.

[78] F. Lavigne, C. Bourgaux, and M. Ollivon, "Phase transitions of saturated triglycerides," *J. Phys. JP. IV, Colloq.*, vol. 3, pp. 137–140, 1993.

[79] D. M. Small, "The physical chemistry of lipids from alkanes to phospholipids," *Handb. Lipid Res.*, vol. 4, pp. 1–672, 1986.

[80] S. Bruin, "Phase equilibria for food product and process design1," *Fluid Phase Equilib.*, vol. 158, pp. 657–671, 1999.

[81] C. Krafft, L. Neudert, T. Simat, and R. Salzer, "Near infrared Raman spectra of human brain lipids," *Spectrochim. Acta Part A Mol. Biomol. Spectrosc.*, vol. 61, no. 7, pp. 1529–1535, 2005.

[82] R. G. Snyder, "The structure of chain molecules in the liquid state: Low-frequency Raman spectra of n-alkanes and perfluoro-n-alkanes," *J. Chem. Phys.*, vol. 76, no. 8, pp. 3921–3927, 1982.

[83] R. A. MacPhail, H. L. Strauss, R. G. Snyder, and C. A. Elliger, "Carbon-hydrogen stretching modes and the structure of n-alkyl chains. 2. Long, all-trans chains," *J. Phys. Chem.*, vol. 88, no. 3, pp. 334–341, 1984.

[84] C. Takechi and F. Kaneko, "X-ray diffraction and vibrational spectroscopic study of the influence of cis- and trans-unsaturation on the α-phase of triacylglycerols," *J. Phys. Chem. B*, vol. 117, no. 29, pp. 8896–8905, 2013.

[85] E. Da Silva, S. Bresson, and D. Rousseau, "Characterization of the three major polymorphic forms and liquid state of tristearin by Raman spectroscopy," *Chem. Phys. Lipids*, vol. 157, no. 2, pp. 113–119, 2009.

[86] M. Motoyama, "Structure and Phase Characterization of Triacylglycerols by Raman Spectroscopy," *Bull NARO Inst Livest Grassl Sci*, vol. 12. pp. 19–68, 2012.

[87] B. L. Joshi, "Rheology and Thermodynamics of Fat/Oil Blends," Hochschule Offenburg, 2017.

[88] A. Minato *et al.*, "Synchrotron radiation X-ray diffraction study on phase behavior of PPP-POP binary mixtures," *J. Am. Oil Chem. Soc.*, vol. 73, no. 11, pp. 1567–1572, 1996.

[89] C. P. Tan and Y. B. C. Man, "Differential scanning calorimetric analysis of palm oil, palm oil based products and coconut oil: effects of scanning rate variation," *Food Chem.*, vol. 76, no. 1, pp. 89–102, 2002.

[90] M. Geary and R. Hartel, "Crystallization Behavior and Kinetics of Chocolate-Lauric Fat Blends and Model Systems," *J. Am. Oil Chem. Soc.*, vol. 94, no. 5, pp. 683–692, 2017.

[91] S. Padar, S. A. K. Jeelani, and E. J. Windhab, "Crystallization kinetics of cocoa fat systems: experiments and modeling," *J. Am. Oil Chem. Soc.*, vol. 85, no. 12, pp. 1115–1126, 2008.

[92] H. Kamphuis and R. J. J. Jongschaap, "The rheological behaviour of suspensions of fat particles in oil interpreted in terms of a transient-network model," *Colloid Polym. Sci.*, vol. 263, no. 12, pp. 1008–1024, 1985.

[93] R. Vreeker, L. L. Hoekstra, D. C. Den Boer, and W. G. M. Agterof, "The fractal nature of fat crystal networks," *Colloids and surfaces*, vol. 65, no. 2–3, pp. 185–189, 1992.

[94] J. M. Deman and A. M. Beers, "Fat crystal networks: structure and rheological properties," *J. Texture Stud.*, vol. 18, no. 4, pp. 303–318, 1987.

[95] N. C. Acevedo, F. Peyronel, and A. G. Marangoni, "Nanoscale structure intercrystalline interactions in fat crystal networks," *Curr. Opin. Colloid Interface Sci.*, vol. 16, no. 5, pp. 374–383, 2011.

[96] S. S. Narine and A. G. Marangoni, "Microscopic and rheological studies of fat crystal networks," *J. Cryst. Growth*, vol. 198, pp. 1315–1319, 1999.

[97] T. S. Awad, M. A. Rogers, and A. G. Marangoni, "Scaling behavior of the elastic modulus in colloidal networks of fat crystals," *J. Phys. Chem. B*, vol. 108, no. 1, pp. 171–179, 2004.

[98] D. Tang and A. G. Marangoni, “Fractal dimensions of simulated and real fat crystal networks in 3D space,” *J. Am. Oil Chem. Soc.*, vol. 85, no. 6, pp. 495–499, 2008.

[99] D. Tang and A. G. Marangoni, “Modified fractal model and rheological properties of colloidal networks,” *J. Colloid Interface Sci.*, vol. 318, no. 2, pp. 202–209, 2008.

[100] A. G. Marangoni and D. Rousseau, “Is plastic fat rheology governed by the fractal nature of the fat crystal network?,” *J. Am. Oil Chem. Soc.*, vol. 73, no. 8, pp. 991–994, 1996.

[101] B. Mahisanunt, H. Hondoh, and S. Ueno, “Effects of Tripalmitin and Tristearin on Crystallization and Melting Behavior of Coconut Oil,” *J. Am. Oil Chem. Soc.*, vol. 96, no. 4, pp. 391–404, 2019.

[102] A. G. Marangoni and M. A. Rogers, “Structural basis for the yield stress in plastic disperse systems,” *Appl. Phys. Lett.*, vol. 82, no. 19, pp. 3239–3241, 2003.

[103] A. G. Marangoni, “Elasticity of high-volume-fraction fractal aggregate networks: A thermodynamic approach,” *Phys. Rev. B*, vol. 62, no. 21, p. 13951, 2000.

[104] L. Ahmadi, A. J. Wright, and A. G. Marangoni, “Structural and mechanical behavior of tristearin/triolein-rich mixtures and the modification achieved by interesterification,” *Food Biophys.*, vol. 4, no. 2, pp. 64–76, 2009.

[105] T. A. Stortz, A. K. Zetzl, S. Barbut, A. Cattaruzza, and A. G. Marangoni, “Edible oleogels in food products to help maximize health benefits and improve nutritional profiles,” *Lipid Technol.*, vol. 24, no. 7, pp. 151–154, 2012.

[106] D. J. Abdallah and R. G. Weiss, “n-Alkanes gel n-alkanes (and many other organic liquids),” *Langmuir*, vol. 16, no. 2, pp. 352–355, 2000.

[107] B. L. Joshi, B. I. Zielbauer, and T. A. Vilgis, “Comparative Study on Mixing Behavior of Binary Mixtures of Cocoa Butter/Tristearin (CB/TS) and Cocoa Butter/Coconut Oil (CB/CO),” *Foods*, vol. 9, no. 3, p. 327, 2020.

[108] K. Chaleepa, A. Szepes, and J. Ulrich, “Effect of additives on isothermal crystallization kinetics and physical characteristics of coconut oil,” *Chem. Phys. Lipids*, vol. 163, no. 4–5, pp. 390–396, 2010.

[109] C. Ishibashi, H. Hondoh, and S. Ueno, “Epitaxial growth of fat crystals on emulsifier crystals with different fatty acid moieties,” *Cryst. Growth Des.*, vol. 17, no. 12, pp. 6363–6371, 2017.

[110] K. Chaleepa, A. Szepes, and J. Ulrich, “Effect of additives on isothermal crystallization kinetics and physical characteristics of coconut oil,” *Chem. Phys. Lipids*, vol. 163, no. 4–5, pp. 390–396, 2010.

[111] A. J. Wright, R. W. Hartel, S. S. Narine, and A. G. Marangoni, “The effect of minor components on milk fat crystallization,” *J. Am. Oil Chem. Soc.*, vol. 77, no. 5, pp. 463–475, 2000.

Statutory declaration

I declare that I have developed and written the enclosed Ph.D. thesis completely by myself, and have not used sources or means without declaration in the text. Any thoughts from others or literal quotations are clearly marked. The Ph.D. thesis was not used in the same or in a similar version to achieve an academic grading or is being published elsewhere.

Mainz, 09.03.2021

Bhagyashri Laxmikant Joshi

Matlab and Python program code for data analysis

1) 'Xipk' automated program for data extraction
Author- <u>Dr. Robert Graf</u>

```
 (#include <stdio.h>
#include <string.h>
#include <inc/exptUtil>
#include<math.h>


int td;
int ne;
int si;
int exp1;
int proc2;
int proc;
int lf, rf, lp, rp;
int status;
float       offset_f2, sr_f2, sr_f1, dw_f2, dw_f1, scaling;
double   sw_f2, sw_f1, o1;
char nm1[20],dsk[20], nm2[20], serfile[200],command[400];
char *ptr;

GETCURDATA



//*************************************************************************************************
*****
//*        Read some variables from Bruker NMR dataset                                  *
//*************************************************************************************************
*****

si = 8192;
FETCHPAR1S("TD",&td);
FETCHPAR1S( "IN_F", &dw_f1 );
FETCHPARS( "SW", &sw_f2 );
FETCHPARS( "OFFSET", &offset_f2 );
STOREPAR( "SI", si );
STOREPAR( "ABSG", 2);
STOREPAR( "ABSF1", 250.0 );
STOREPAR( "ABSF2", -250.0);
STOREPAR( "F1P", 200.0 );
STOREPAR( "F2P", -200.0);
STOREPAR1( "F1P", 0.0 );
STOREPAR1( "F2P", td*dw_f1/2000000);
STOREPAR1( "WDW", 0);
STOREPAR1( "PH_mod", 0);
XCMD("xtrf xdim");
i2 = td;
proc=procno+1;
WRP(proc)
```

```
RPROCNO(proc)

//*************************************************************************************************
*****
//*       Do automated phase correction and baseline corrections for idividual slices       *
//*************************************************************************************************
*****

for(ne=0; ne<i2; ne++){
                        RSR(ne+1,9999)
                        RPROCNO(9999)
                        APKS
                        ABSF
                        WSR(ne+1, proc, expno, name, user, disk)
                        RPROCNO(proc)
                        }
DELETEPROCNO(name, expno, 9999, disk, user)
DATASET(name, expno, proc, disk, user)
VIEWDATA_SAMEWIN
proc=proc+1;
WRP(proc)
RPROCNO(proc)
STOREPAR( "ABSG", 5);
STOREPAR( "ABSF1", 20.0 );
STOREPAR( "ABSF2", -15.0);
STOREPAR( "F1P", 20.0 );
STOREPAR( "F2P", -15.0);
ABS2

//*************************************************************************************************
*****
//*       Do do some computations for integration ranges                                  *
//*************************************************************************************************
*****

lf = si*((offset_f2 - 200)/sw_f2);
rf = si*((offset_f2 + 200)/sw_f2);
lp = si*((offset_f2 - 10.0)/sw_f2);
rp = si*((offset_f2 + 5.0)/sw_f2);

//(void) sprintf(text,"offset:  %f --- sw: %f.",(-200.0-offset_f2)/sw_f2), sw_f2);
(void) sprintf(text,"2D phase correction finished !! \n (full proc 2: %i - %i, peaks proc 3: %i - %i) .",lf,rf,lp,rp);
QUITMSG(text);
```

2) 'Readreal' automated program for data extraction
Author- <u>Dr. Robert Graf</u>

```
%#########################################################################
%#
%#                       function READREAL
%#
%#     reads in data as max. 4D real arrays from typical BRUKER process files.
%#     If dimensions (n1...n4) are specified, the routine generates according dimensions.
%#     If the product of dimensions is smaller than the data length, the routine tries to
%#     estimate/generate the next higher dimension. Hence, if nothing but the filename
```

```
%#      is specified the data are read in as 1D.
%#
%#      usage: data=readreal(filename,n1,n2,...);
%#
%#           n1...n4 = optional dimensions (estimated from data length if not present)
%#      (c) P. Bl?mler 2/03
%#########################################################################
%-------------------------------------------------------------------------
%  version 1.0 PB 3/2/03    (please change this when code is altered)
%             RG 5/18/18   adopted to the new TopSpin version 3.5pl7
%-------------------------------------------------------------------------


function data=readreal(infile,n1,n2,n3)

fid=fopen(infile,'r','l');
if fid==-1
   disp('ERROR: file not found');
   data=[];
   return
end
data=fread(fid,'int32');
fclose(fid);
[fsize,c]=size(data);
if exist('n1')==0
   n1=fsize;
end
if exist('n2')==0
   n2=round(fsize/n1);
end
if exist('n3')==0
   n3=round(fsize/n1/n2);
end
n4=round(fsize/n1/n2/n3);
if n1*n2*n3*n4 ~= fsize
   disp('RESET to 1D: something wrong with dimensions!');
   n1=fsize; n2=1; n3=1; n4=1;
end
if n4 ~= 1
   disp(['Reading data as 4D real: Size ',num2str(n1),' x ',num2str(n2),' x ',num2str(n3),' x ',num2str(n4),'
points']);
elseif n3 ~= 1
   disp(['Reading data as 3D real: Size ',num2str(n1),' x ',num2str(n2),' x ',num2str(n3),' points']);
elseif n2 ~= 1
   disp(['Reading data as 2D real: Size ',num2str(n1),' x ',num2str(n2),' points']);
elseif n1 == fsize
   disp(['Reading data as 1D real: Size ',num2str(n1),' points']);
end
data=reshape(data,n1,n2,n3,n4);
data=squeeze(data);

)
```

3) SFC determination after area integration-MATLab R2017a
Author- <u>Dr. Robert Graf</u>

(>> fw=readreal('CB10-CO90_180511_2.dat',8192,256);

```
Reading data as 2D real: Size 8192 x 256 points
>> fw=fw(987:7544,1:193);
>> pa=readreal('CB10-CO90_180511_3.dat',8192,256);
Reading data as 2D real: Size 8192 x 256 points
>> pa=pa(4102:4347,1:193);
>> Ipa=sum(pa,1);
>> Ifw=sum(fw,1);
>> plot(Ifw)
>> plot(Ipa)
>> plot(Ipa./Ifw)
>> Integral_of_peaks=Ipa./Ifw;
)
```

4) Fractal dimension from multiple PLM images

Author: Anoop (Mathworks) and modified for multiple images by Bhagyashri Joshi

```
(%Assume jpg images are in the same directory as the m file.
   indir = cd; %Modify the indir to location of the jpg files.
   outdir = 'Gray'; %Name or output directory.
     directory = dir([indir, '\', '*.jpg']);

   if ((~exist(outdir, 'dir') && length(directory) > 0))
      %Create new directory named outdir if directory not exist.
      mkdir(outdir);
   end

fid = fopen('sf and blackpicese.txt','w');
fileID = fopen('FD.txt', 'w');
   for i = 1 : length(directory)
      filename = directory(i).name;
      rgb_img = imread([indir, '\', filename]);
      if (ndims(rgb_img) == 3) %Make sure img is RGB (not gray).
         I2=imresize(rgb_img,[2048 2048]); %to resize the image
         img = rgb2gray(I2); % Convert rgb to grayscale
         I3 = im2double(img);
         lev = thresh_tool(I3);
         %level = graythresh(img);
         BW = imbinarize(I3,lev);
         WB=logical(1-BW);
         %img=img <= 127;      % convert grascale to black and white
         %Save gray image to outdir (keep original name).
         %imshowpair(image,BW,'montage')
         imwrite(WB, [outdir, '\', filename]);
      end
% initialises the varaibles for plotting the graph. scale is used to store
% the scaling factors and the count is used to store the number of boxes
% which contains parts of the image. For a given scale(1,i) value, the number
% of boxes occupied by the image will be available at count(1,i)
scale=zeros(1,11);
count=zeros(1,11);

[width,height,cols]=size(WB);
% since the program is for a 512x512 image, the limit is set
% to 11 since 2^11=2048

for j=1:11
  % scaling factors are taken as 2,4,8,16... 512.
```

```
  % For each scaling factor, the total number of pieces are to be calculated,
  % and the number of pieces which contain the black dots (pixels) among them are to
  % be counted.

  % For eg, when the scaling factor is 2, it means the image is divided in to
  % half, hence we will get 4 pieces. And have to see how many of pieces
  % have the black dots.
  sf=2^j;
  pieces=sf^2;
  pieceWidth=width/sf;
  pieceHeight=height/sf;

  %initially we assume, we have 0 black pieces
  blackPieces=0;

  % Now we have to iterate through each pieces to see how many pieces have the
  % black dots (pixel) in it. We will consider the collection of pieces as
  % a matrix. We are counting from 0 for the ease of calculations.
  for pieceIndex=0:pieces-1

     % row and column indices of each pieces are calculated to estimate the
     % xy cordinates of the starting and ending of each piece.
     pieceRow=idivide(int32(pieceIndex), int32(sf));
     pieceCol=rem(pieceIndex,sf);
     xmin=(pieceCol*pieceWidth)+1;
     xmax=(xmin+pieceWidth)-1;
     ymin=(pieceRow*pieceHeight)+1;
     ymax=(ymin+pieceHeight)-1;

     % each piece is extracted and stored in another array for
     % convenience.
     eachPiece=WB(ymin:ymax,xmin:xmax);

     %each piece obtained is plotted on a plot for getting a view
     %of the splitting of the whole image.
     %subplot(sf,sf,pieceIndex+1), imshow(eachPiece);

     % now, we will check whether the piece has some black dots in it.
     % then the count of the black pieces will be incremented.
     if (min(min(eachPiece))== 0)
        blackPieces=blackPieces+1;
     end
  end

  % the count of pieces which contains the black dots for a given scaling value
  % will be obtained here and will be stored in the respective variables.
  %fprintf('%d\t->\t%d\n', sf, blackPieces);
  fprintf(fid,'%d\t->\t%d\n', sf, blackPieces);
  scale(1,j)=sf;
  count(1,j)=blackPieces;
end

% Now the process is over, the graph is plotted and the fractal dimension
% is calculated using the 'ployfit' function.

f = figure('visible','off');
   hold on;
```

```
p = polyfit(log(scale),log(count),1);
c = polyval(p,log(scale));
fprintf(fileID, '%d\t->\t%d\n', p(1), p(2));
%a = p(1);
%b = p(2);
plot(log(scale),log(count),'o',log(scale),c, '-' );
xlabel('log (scale)');
ylabel('log (count)');
legend('data','linear fit');
saveas(f,sprintf('FIG%d.png',i)); % will create FIG1, FIG2,...
end
fclose(fileID);
fclose(fid);
```

5) NMR-Avrami model fitting-Python
Author-Bhagyashri Joshi

```
get_ipython().run_line_magic('matplotlib', 'inline')
import pandas as pd
import matplotlib.pyplot as plt
df=pd.read_excel(r'C:/Users/joshi/Desktop/NMR/CBNMR.xlsx',sheet_name='CB90')
x = df['time'].values
y = df['SFC'].values
z = df['SFC_SD'].values
y1=y[0:12]
x1=x[0:12]
yerr=z[0:12]
#plt.errorbar(x,y,z,fmt='bo')
#plt.scatter(x1,y1)
plt.errorbar(x1,y1,yerr,fmt='bo')
plt.show()  # or plt.savefig("name.png")#defining the function
import numpy as np
S0=df.at[0,'SFC']
S1=df.at[12,'SFC']
#t0=15
def SFC(x1,a0,a1):
    return S0+((S1-S0)*(1-np.exp(-a0*(x1)**a1)))
import scipy.optimize as optimize
from scipy.optimize import curve_fit
popt, pcov = optimize.curve_fit(SFC, x1, y1,sigma=None)
print(popt)
yEXP = SFC(x1, *popt)
#plt.errorbar(x1, y1,yerr,fmt='b.', x1, yEXP,'k--')
fig = plt.figure()
ax1 = plt.axes()
ax1.errorbar(x1, y1,yerr=yerr)
ax1.plot(x1,SFC(x1,*popt),'--k')
#r^2value determination
import sklearn
from sklearn.metrics import r2_score
print ('R^2:', r2_score (yEXP,y1))
```

6) XRD-data analysis –Python
Author-Bhagyashri Joshi

```
import pandas as pd
import matplotlib.pyplot as plt
import numpy as np
import peakutils
from peakutils.plot import plot as pplot
from matplotlib import pyplot
get_ipython().run_line_magic('matplotlib', 'inline')
import scipy
from scipy.optimize import least_squares
from scipy import optimize
from scipy.optimize import curve_fit
import math

df=pd.read_excel(r'C:/Users/joshi/Desktop/Results section/python/XRD/XRD.xlsx', sheet_name='070')
x = df['q'].values
y = df['I'].values
plt.plot(x,y)
plt.show()
y2 = y + np.polyval([-1.05,1.5], x)
base = peakutils.baseline(y2, 1)
def _1gaussian(x, amp,cen,sigma):
   return amp*(1/(sigma*(np.sqrt(2*np.pi))))*(np.exp((-1.0/2.0)*(((x-cen)/sigma)**2)))
def _2gaussian(x, amp1,cen1,sigma1, amp2,cen2,sigma2):
    return amp1*(1/(sigma1*(np.sqrt(2*np.pi))))*(np.exp((-1.0/2.0)*(((x-cen1)/sigma1)**2))) + \
        amp2*(1/(sigma2*(np.sqrt(2*np.pi))))*(np.exp((-1.0/2.0)*(((x-cen2)/sigma2)**2)))
popt_2gauss, pcov_2gauss = scipy.optimize.curve_fit(_2gaussian, x, y2-base, p0=[0.8,1.28,0.1,11,1.42, 0.08])
perr_2gauss = np.sqrt(np.diag(pcov_2gauss))
pars_1 = popt_2gauss[0:3]
pars_2 = popt_2gauss[3:6]
gauss_peak_1 = _1gaussian(x, *pars_1)
gauss_peak_2 = _1gaussian(x, *pars_2)
F1=2.3548*popt_2gauss[2]
F2=2.3548*popt_2gauss[5]
FWHM1=(math.asin((F1*0.154)/(4*math.pi)))  #radian
thetha1=(math.asin((popt_2gauss[1]*0.154)/(4*math.pi))) #radian
D1=(0.9*1.54)/(FWHM1*np.cos((thetha1))) #angstrom
LS1=10*(2*np.pi)/popt_2gauss[1] #angstrom
FWHM2=(math.asin((F2*0.154)/(4*math.pi)))  #radian
thetha2=(math.asin((popt_2gauss[4]*0.154)/(4*math.pi))) #radian
D2=(0.9*1.54)/(FWHM2*np.cos((thetha2))) #angstrom
LS2=10*(2*np.pi)/popt_2gauss[4] #angstrom
#areas = [np.trapz(y, x) for xs,ys in zip(xsplit, ysplit)
#print(pars_1, pars_2)
#print(popt_2gauss,perr_2gauss,)
fig = plt.figure()
pyplot.figure(figsize=(10,6))
ax1 = plt.axes()
ax1.plot(x, y2-base,'y-',x,_2gaussian(x,*popt_2gauss),'--k')
ax1.plot(x, gauss_peak_1, "g")
#ax1.fill_between(x, gauss_peak_1.min(), gauss_peak_1, facecolor="green", alpha=0.5)
ax1.plot(x, gauss_peak_2, "y")
#ax1.fill_between(x, gauss_peak_2.min(), gauss_peak_2, facecolor="yellow", alpha=0.5)
ax1.figure.savefig('C:/Users/joshi/Desktop/Results section/python/XRD/070.png')
```

```
import xlsxwriter
workbook = xlsxwriter.Workbook('result070.xlsx')
worksheet1 = workbook.add_worksheet('070')
#worksheet2 = workbook.add_worksheet('070')
#worksheet3 = workbook.add_worksheet('080')
#worksheet4 = workbook.add_worksheet('085')
#worksheet5 = workbook.add_worksheet('115')
header = (['amp1', popt_2gauss[0]],
['cen1',popt_2gauss[1]],
['sigma1',  popt_2gauss[2]],
['amp2', popt_2gauss[3]],
['cen2',popt_2gauss[4]],
['sigma2',  popt_2gauss[5]],
['FWHM1',  FWHM1],
['D1', D1],
['LS1', LS1],
['FWHM2',  FWHM2],
['D2', D2],
['LS2', LS2])
row = 0
col = 0
for parameters, value in (header):
    worksheet1.write(row, col,     parameters)
    worksheet1.write(row, col + 1, value)
    row += 1
workbook.close()
```

Appendix

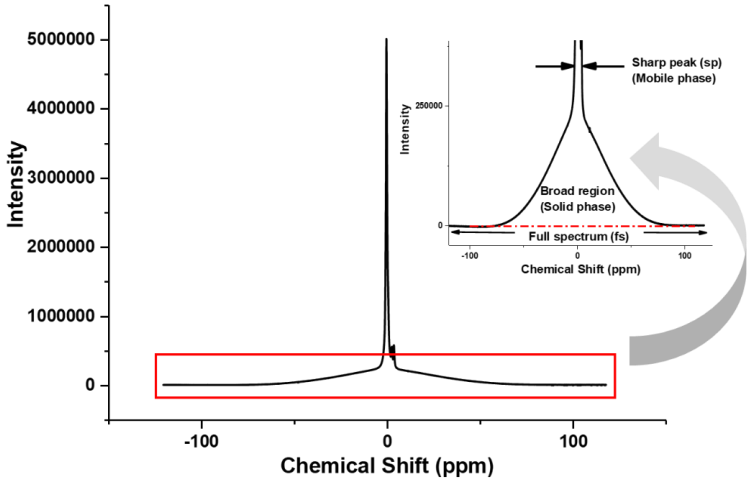

Figure 65: Spectrum detected from ^{1}H ssNMR for a sample and inset graph is the zoom view of a red rectangle region, where, the three regions are indicated.

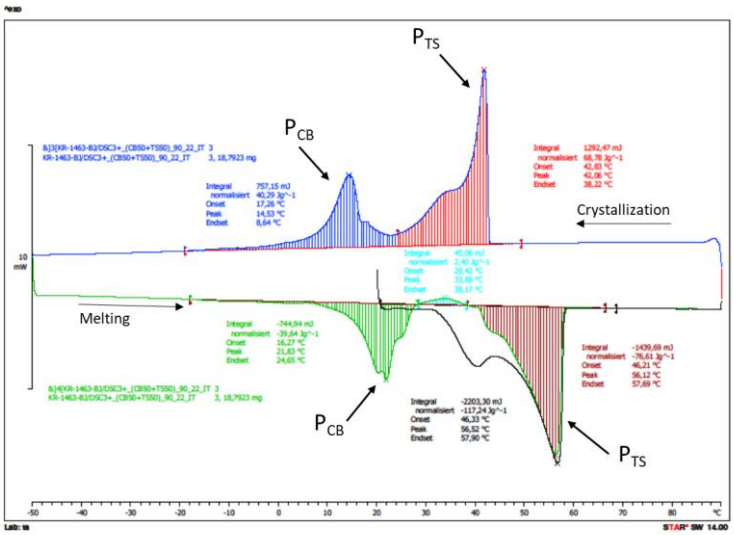

Figure 66: Area under the peaks for CB (50%)+TS (50%) is shown

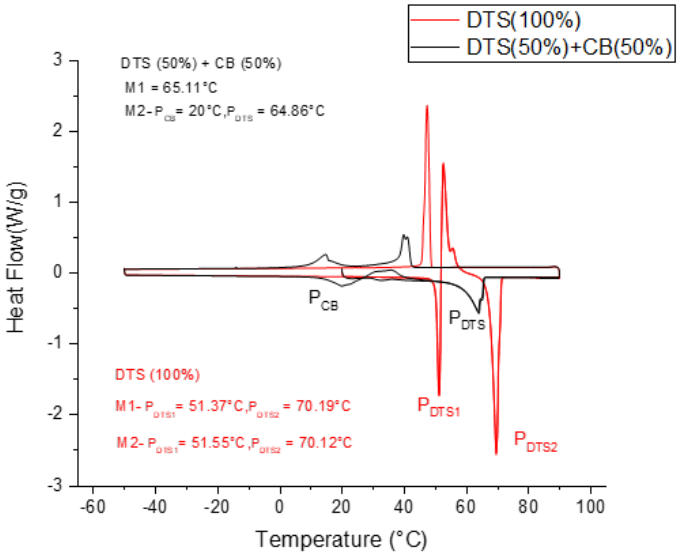

Figure 67: DSC thermal profile of deuterated TS (dTS or DTS) and 50/50 wt% of CB and DTS

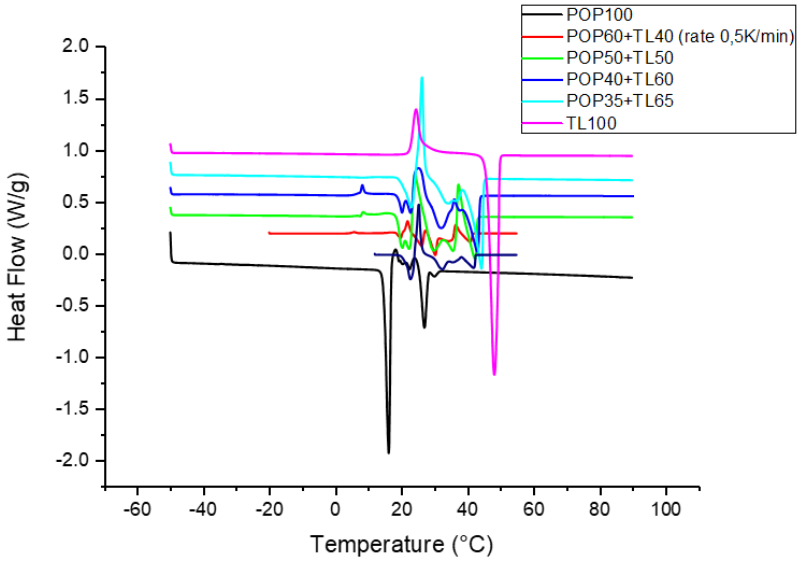

Figure 68: The DSC thermogram for pure components of CB (POP) and CO (Trilaurin) showed no eutectic behavior.

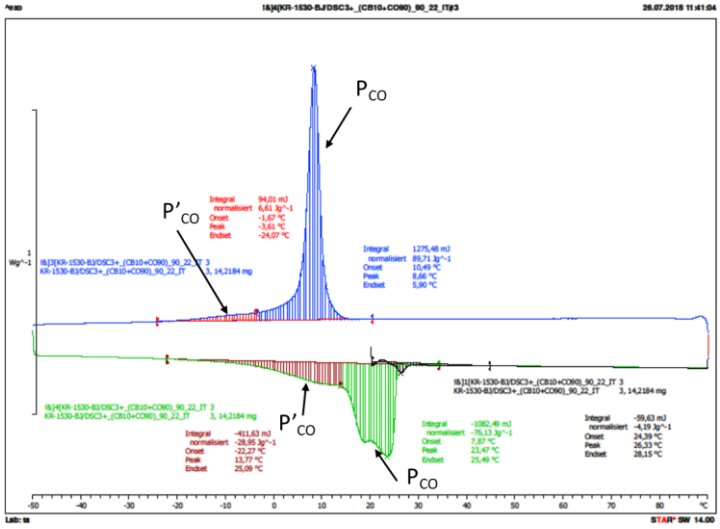

Figure 69: Area under the curves for P_{CO}, and P'_{CO} for CB (10%)+CO (90%).

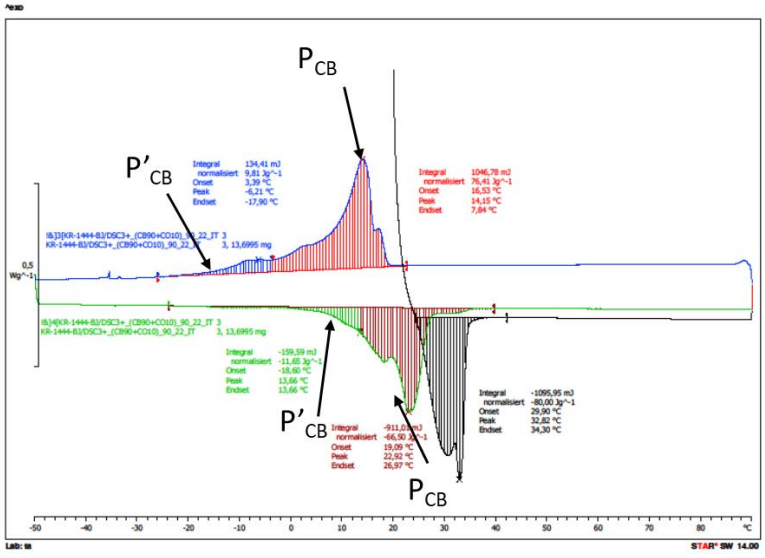

Figure 70: Area under the curves for P_{CB}, and P'_{CB} for CB (90%) + CO (10%).

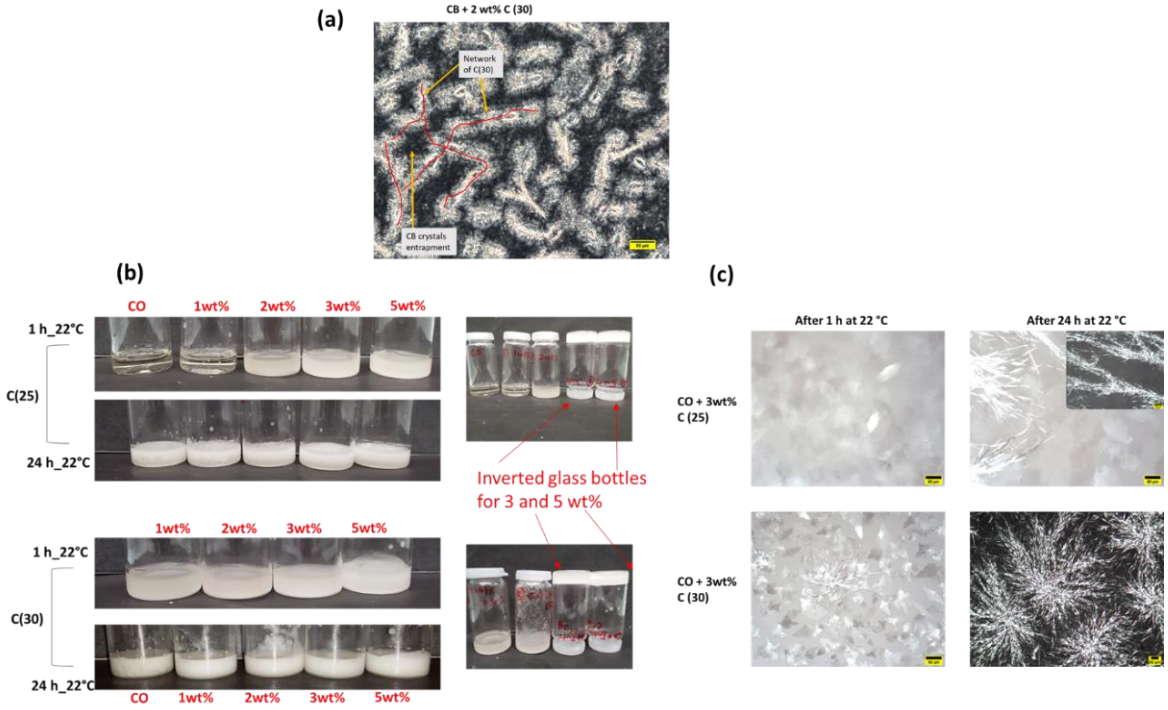

Figure 71: (a) 'oleogel like' crystal behavior for CB + 2wt% C (30); (b) represents the images of glass bottles containing CO mixtures with 1,2, 3, and 5 wt% of C (25) and C (30) after 1 h and 24 h at 22 °C. (c) Simultaneously, the microscopy images are shown for 3 wt% of C (25) and C (30) addition. The scale bar = 50 µm.

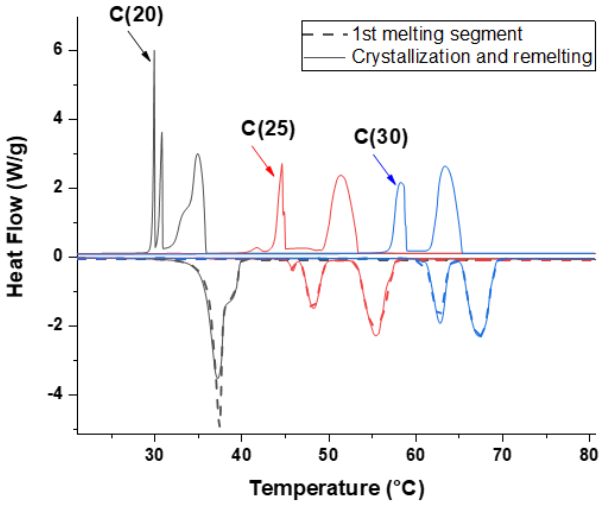

Figure 72: Thermal behavior of pure n-alkanes.

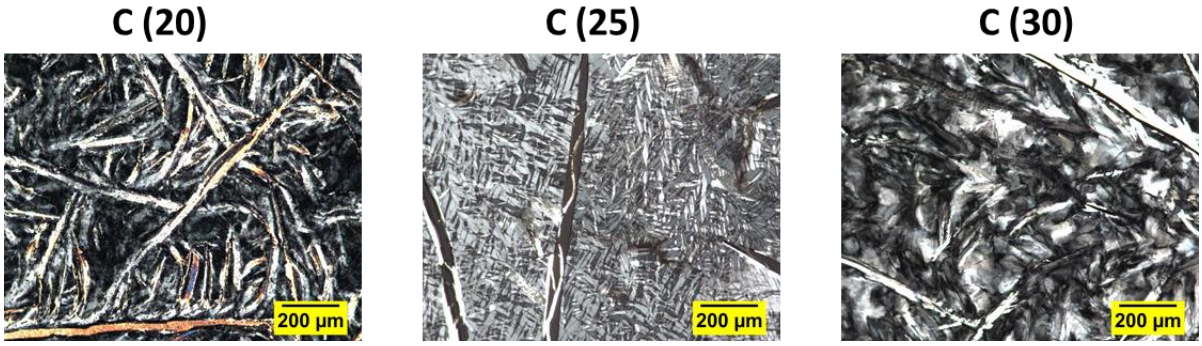

Figure 73: Crystal morphology of n-alkanes after 24 h at 22 °C. The scale bar = 200 µm.

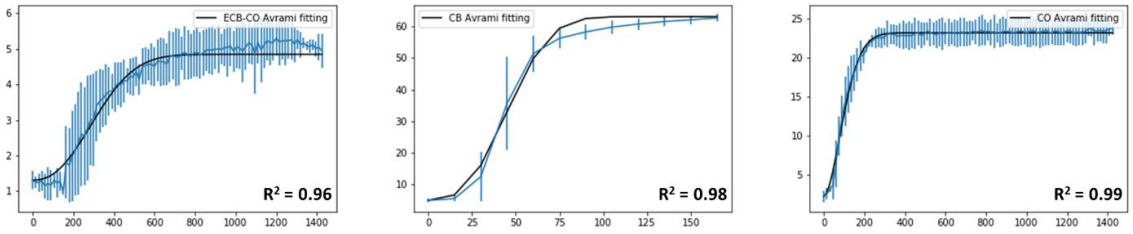

Figure 74: Avrami fitting to SFC profiles of E_{CB-CO}, CB, and CO.